UNIVERSITÀ DEGLI STUDI DI PADOVA

Dipartimento di Ingegneria dell'Informazione
Scuola di Dottorato di Ricerca in Ingegneria dell'Informazione - Indirizzo Scienza e Tecnologia dell'Informazione

Ph.D. Thesis

Reliability and failure analysis of RF-MEMS switches for space applications

Author: Enrico Autizi
Coordinator: Prof. Matteo Bertocco
Advisor: Prof. Gaudenzio Meneghesso

Academic Year 2010/2011

Padova, January 25th, 2011

Contents

Abstract

Wireless communication systems for space applications requires electronic components with an high level of reliability, a low power consumption and they should be as small as possible in order to be better integrated in satellites. Radio Frequency Micro Electro Mechanical (RF-MEMS) components can be considered one of the best candidates to comply with previous requirements and, under certain conditions, they can completely replace an entire solid state circuit [1]. RF-MEM devices in general are characterized by a good miniaturization, an easily integration in a standard solid state circuit, an almost zero power consumption, a good RF linearity and an high quality factor Q [2].

Concerning RF-MEMS switches RF performances, they exhibit a very low insertion loss, lower than 0.1dBm up to 100GHz and, at the same time, a good isolation, more than 20dBm. From an electrical and mechanical point of view the power consumption of these switches is close to zero because of an “on-state” current around pA and they are almost unaffected by high level of acceleration or deceleration because of their mass that is extremely small. The possibility to integrate the production of these devices in the standard foundry silicon processes and their integration with mature semiconductor technology are a great advantage for their spread making possible to produce them in an easy and cheap way.

Over the last 10 years important developments on MEMS switches have been done all over the world. As a matter of fact, these switches are quite attractive since they combine the excellent RF performances and low power consumption of mechanical switches with the small size and low weight of semiconductor devices. However, the appearance of MEMS switches on the market has been hindered by the need for specific packaging [3] [4] [5] as well as by reliability issues [6]. Reliability is a major issue for any satellite since it is almost impossible to envisage any repair work once the spacecraft has been launched. Hence, reliability is a key driver when designing any RF equipment. If we consider a RF-MEMS switch, we have to guarantee that his electro-mechanical performances will be the same after an intensive usage in harsh environment, for instance after millions or billions of cycles and after the exposure to different kind of radiations. In case of their application in a redundancy scheme they have to be completely operative even after a long period of activity or inactivity.

The aim of this thesis is to perform an electrical characterization and several reliability tests on different kind of RF-MEMS switches in order to analyze which are the weaknesses and the strengths of this new technology. Electrical characterizations have been done using two different measurement systems. The first, based on a vector network analyzer and a power supply, has been used to test the RF performances of the devices and to extract the best actuation and deactuation voltages. The second set up, based on the internal RF signal generator of the VNA, and an 8-GHz digital signal oscilloscope, has been used to characterize the electrical performances like actuation time, release delay. Cycling stress, one of the most common test used to understand the robustness of this kind of devices, has been performed on different topologies of switch in order to better understand how some parameters, such as the shape of the beams or the actuation voltage, impact on the reliability of the device.

Furthermore, the influence of continuous actuation stress on the reliability of dielectric-less switches has been investigated, comparing different designs and studying the variation of the main electrical parameters induced by the stress and the successive recovery phase.

Other two critical issues investigated in this thesis are the sensitivity to EOS/ESD events of RF-MEMS switches under actuated and not-actuated conditions and their sensitivity to different kind of radiation, protons and X-rays.

The sensitivity to EOS/ESD has been studied between RF-OUT and ground with no bias voltage applied (up-state membrane), and between RF-OUT and GND at different voltages (fully actuated / partially bended membrane). Moreover, the same devices have been characterized under HBM regime in order to study if any correlation between TLP tests and the Human Body Model exists for these devices.

Concerning the radiation effects, the impact of 2MeV protons and 10keV x-rays radiation stresses has been analyzed at increasing radiation dose and during subsequent annealing at room temperature.

Sommario

I sistemi wireless di comunicazione per applicazioni spaziali richiedono componenti con un elevato grado di affidabilità, un basso consumo di potenza e ridotte dimensioni al fine di agevolare la loro integrazione all'interno di satelliti. I componenti Micro Elettro Meccanici per Radio Frequenza (RF-MEMS) sono tra i migliori candidati per la realizzazione di dispositivi in grado di sostituire i normali circuiti a stato solido. I vantaggi di tale tecnologia sono: elevata miniaturizzazione, facilità di integrazione in un circuito allo stato solido, potenza consumata prossima allo zero, ottime performance RF ed un elevato fattore di merito Q.
Per quanto rigurada le performance RF degli RF-MEMS switches, questi sono caratterizzati da una insertion loss bassa, minore di 0.1dBm fino a 100GHz, ed allo stesso tempo da un buon isolamento, maggiore di 20dBm. Da un punto di vista elettrico e meccanico la potenza consumata è estremamente bassa in quanto la corrente assorbita durante il loro funzionamento è di qualche decina di pA ed inoltre reagiscono molto bene ad accelerazioni o decelerazioni elevate grazie alla massa ridotta. La possibilità di integrare la loro produzione all'interno del classico processo utilizzato per i dispositivi in silicio rappresenta un notevole vantaggio a favore della loro diffusione ed integrazione.
Negli ultimi 10 anni sono stati fatti enormi passi avanti in questo settore. Essi infatti mettono insieme le eccellenti performance RF ed i bassi consumi degli switch meccanici con le dimensioni estremamente ridotte dei dispositivi a semiconduttore. Tuttavia la necessità di specifici packages e la presenza di diversi problemi affidabilistici hanno rallentato la loro diffusione. In ambito spaziale l'afidabilità è estremamente importante in quanto un qualsiasi intervento tecnico una volta lanciato il satellite è impossibile da effettuarsi. Nel caso di un RF-MEMS switch le performance devono essere garantite

dopo un utilizzo intensivo, come ad esempio dopo miliardi di cicli di funzionamento, in un ambiente ostile e soggetto a radiazioni. In applicazioni ridondanti bisogna inoltre garantire la piena operatività dopo numerosi anni di funzionamento o di inattività.

Lo scopo di questa tesi è caratterizzare da un punto di vista elettrico ed affidabilistico diversi tipi di RF-MEMS switches al fine di analizzare punti di forza e debolezze di questa nuova tecnologia. Le caratterizzazioni elettriche sono state effettuate utilizzando due differenti set-up di misura. Il primo, composto da un network analyzer e da un generatore di tensione, è stato utilizzato per valutare le performance RF dei dispositivi ed estrarre le migliori tensioni di attuazione e disattuazione. Il secondo, basato sul generatore interno di segnale del network analyzer e da un oscilloscopio digitale è stato utilizzato per misurare i tempi di attuazione e disattuazione. Il cycling stress, uno dei metodi più comunemente utilizzati per valutare l'affidabilità di tali siwtch, è stato effettuato su diverse tipologie di dispositivi al fine di valutare quale fosse l'impatto di parametri come la forma delle struttura sospesa o la tensione di attuazione sull'affidabilità.

Si è inoltre studiato l'effetto di un'attuazione continua su dispositivi privi di dielettrico, paragonando quattro diversi tipi di layout e studiando il cambiamento dei principali parametri elettrici durante lo stress e durante la fase di recupero.

Altri 2 problemi critici che si sono affrontati in questa tesi sono la sensibilità ad eventi EOS/ESD di switch RF-MEMS sia attuati che disattuati e gli effetti di irragiamenti con protoni o raggi X.

Test EOS/ESD sono stati condotti tra i pad RF-OUT e GND senza una tensione applicata (quindi con la membrana sospesa sollevata), e tra RF-OUT e GND a differenti tensioni (membrana a contatto e parzialmente piegata). Gli stessi dispositivi sono stati inoltre in regime HBM per vedere se esiste una correlazione tra i test condotti con TLP e lo Human Body Model.

Per quanto riguarda gli irragiamenti, si è studiato l'effetto di protoni con energia pari a 2MeV e raggi X a 10KeV durante lo stress incrementando la dose e durante la fase di annealing a temperatura ambiente.

Capitolo 1

Devices description

The devices used in this thesis have been developed during two different projects, the first one is an Italian research project called *Modelling, design and characterisation of MEMS devices for reconfigurable radio-frequency transceiver architectures* that belongs to the Projects of Relevant National Interest (PRIN). The second one is a European project called *High reliability MEMS redundancy switch* sponsored by the European Space Agency (ESA) whose purpose is to develop a reliable redundancy switch for space applications. In both projects, the devices, ohmic switches with shunt or series topology and different anchorages, have been manufactured by Bruno Kesler Foundation (FBK) of Trento (Italy).

1.1 Introduction to anchored beams and cantilever structures

The structures of the RF-MEMS switches developed in these projects can be divided into two main groups, depending by the suspended membrane anchorage type: double anchored beams and cantilever beam. In both cases they are electrostatically actuated using an external DC bias.

Their basic working principle it's quite easy [33]. The transmission line is interrupted and, on the top of the interruption, there is a suspended membrane that can be anchored using the two different topologies previously described. The actuation structure, a pull-down electrode, is located under the suspended membrane and in the middle of the line interruption. Biasing the actuation structure, through an external pad, we are able to create a potential difference with the bridge, to bend it thanks to the electrostatic force and, finally, to close the switch.

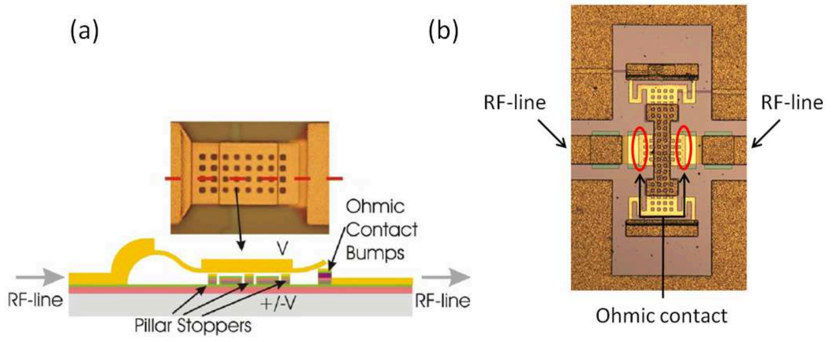

Figure 1.1: Schemes of a cantilever device (a) and picture of a BAT device (b)

Different solutions can be implemented in order to avoid a short circuit between the suspended membrane and the pull-down electrode, these solutions consist in coating the pull-down electrode with Silicon Dioxide or using particular structures, like stopping pillars, as described later.

1.1.1 Basic principles of electrostatic actuation

As mentioned before, all the devices used in these thesis are electrostatically actuated so it's important to clarify which are the basic principles of electrostatic actuation. When we apply a voltage between the pull-down electrode and the suspended membrane, an electrostatic force is induced between these two points. This is almost the same phenomenon that happens between the plates of a capacitor applying a voltage.

In order to make the explanation easier, we can consider the suspended membrane and the pull-down electrode as the two faces of a parallel-plane capacitor, ignoring the fringing fields, and consider the structures shown in Figure 1.2.

According to this hypothesis the parallel plate capacitance is

$$C = \frac{\varepsilon_0 A}{g} = \frac{\varepsilon_0 W w}{g} \tag{1.1}$$

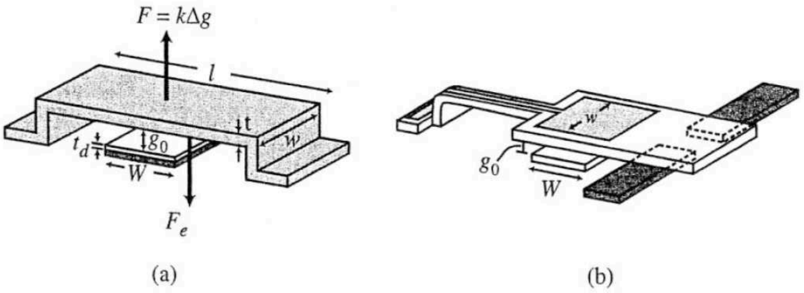

(a) (b)

Figure 1.2: Schemes of a double anchored (a) and cantilever (b) MEMS structure with the pull down electrode

Where w is the width of the beam, W is the width of the pull-down electrode, A it's the area given by Ww and g is the distance between the suspended membrane and the electrode. Considering the power delivered to the capacitor, the fact that the capacitance is time-dependent and assuming that no oxide exists between the electrode plate and the suspended membrane, we can calculate the applied electrostatic force using the following equation:

$$F_e = \frac{1}{2}V^2\frac{dC(g)}{dg} = -\frac{1}{2}\frac{\varepsilon_0 WwV^2}{g^2} \tag{1.2}$$

where V is the voltage applied at the device. Looking at the previous equation it's possible to notice that the force is independent of the voltage polarity, this is the reason why, as we will see later, the DC characteristic of a good device should be perfectly symmetric.

Introducing the Hooke's law of elasticity, $F = Kx$, where F can be considered the mechanical restoring force due to the stiffness of the suspended membrane for a given x displacement, and K the spring constant, we obtain

$$\frac{1}{2}\frac{\varepsilon_0 WwV^2}{g^2} = K(g_0 - g) \tag{1.3}$$

where g_0 is the distance between the bridge and the pull-down electrode with no bias applied. Solving the (1.3) for the voltage we obtain

$$V = \sqrt{\frac{2k}{\varepsilon_0 Ww}g^2(g_0 - g)} \tag{1.4}$$

The plot of the suspended membrane distance (g) versus the applied voltage is shown in Figure 1.3.
It is easy to see from the graph that there are two possible positions for every applied voltage. However, the dashed line represents the unstable portion of the height because the position of the suspended membrane becomes unstable at $(2/3)g_0$ making it to collapse on the pull-down electrode. This instability is caused by the positive feedback in the electrostatic actuation. Let's consider the electric field applied to the bridge, we can write the following equation for the electrostatic force

$$F_e = \frac{QE}{2} \tag{1.5}$$

where Q is the charge on the suspended membrane and $E = V/g$ is the electric field generated by the bias voltage. Increasing the voltage we make the charge to increase, causing an increase in the electrostatic force too. At the same time the force decrease the bridge height which increase the capacitance and thus the charge and the electric field.

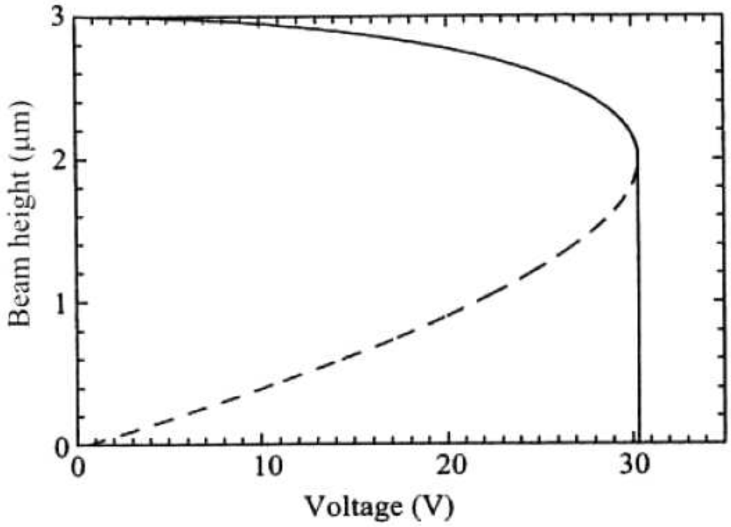

Figure 1.3: Suspended membrane height versus applied voltage. The dashed line represents the unstable portion of the height. (W=100μm, w=100μm, g_0=3μm, K=10N/m)

At a certain point, corresponding to an height of $(2/3)g_0$, the electrostatic force is greater than the restoring force and the suspended membrane col-

lapses to the pull-down electrode.
The same result can be analytically predicted considering the equation (1.4), deriving it with respect to g and setting that to zero. Doing this we can obtain that the instability point is exactly $(2/3)g_0$. At this point, substituting this value to the equation (1.4) we obtain the pull-down voltage that is

$$V_p = V(\frac{2}{3}g_0) = \sqrt{\frac{8k}{27\varepsilon_0 W w}g_0^3} \tag{1.6}$$

Looking at the equation (1.6), although it seems that there is a relation between V_p and w, V_p does not depend on the bridge width because the spring constant k varies linearly with w.

1.1.2 The spring constant

In the previous section we have demonstrated that the actuation voltage depends on the spring constant K. This is a really important parameter for the analysis of the RF-MEMS switches because, knowing its value or, at least, if it's high or low, it let us to predict some interesting behaviors of the device such as inclination towards stiction after long actuation period or susceptibility to cycling.

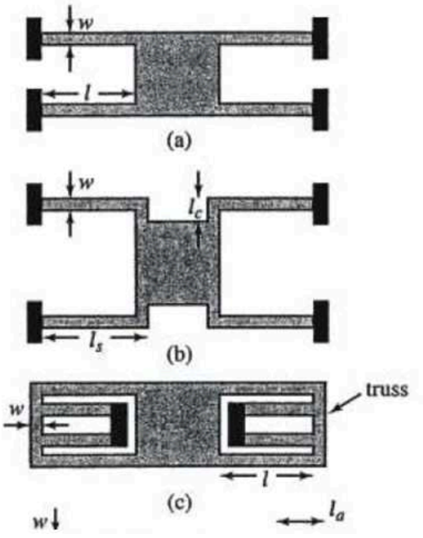

Figure 1.4: Possible solution for changing the spring constant

There are several ways, changing the layout and the suspended membrane beams shape, for increasing or reducing the spring constant. Some of the possible solutions are presented in Figure 1.4. This four configurations differ for the spring constant, from the highest (a) to the lowest (d). Something similar has been used for the devices measured in this thesis. Two different topologies of devices designed by University of Bologna for the PRIN project are shown in Figure 1.5

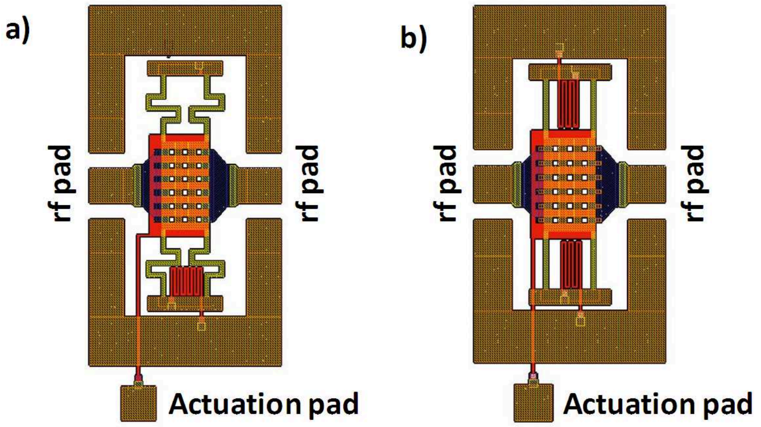

Figure 1.5: Two different structures designed by the University of Bologna. Meander beams (a) and straight beams (b)

As it is possible to see from the previous figure, the suspended membrane structure of device (a) and (b) it's perfectly the same, the only difference in the devices is the beams' shape, meander beams for (a) and straight beams for (b). This difference causes a significant change in the actuation voltage and in the reliability and it will be analyzed deeper in the following chapters.

1.1.3 Effect of holes in the suspended membrane

In almost all MEMS switches, small diameter holes are defined in the suspended membrane in order to improve the switching speed and the hole area can be up to 60% of the total surface.

Holes are useful to reduce the residual stress and the Young's Modulus of the structure. Moreover, the presence of holes cause a reduction in the mass which yields a higher mechanical resonant frequency.

The effects of holes on the up-state capacitance are negligible if their diameter is less than 3-4 times the height of the bridge because of fringing effects. Considering this small rule, the electrostatic force is not affected by the hole density or placement.

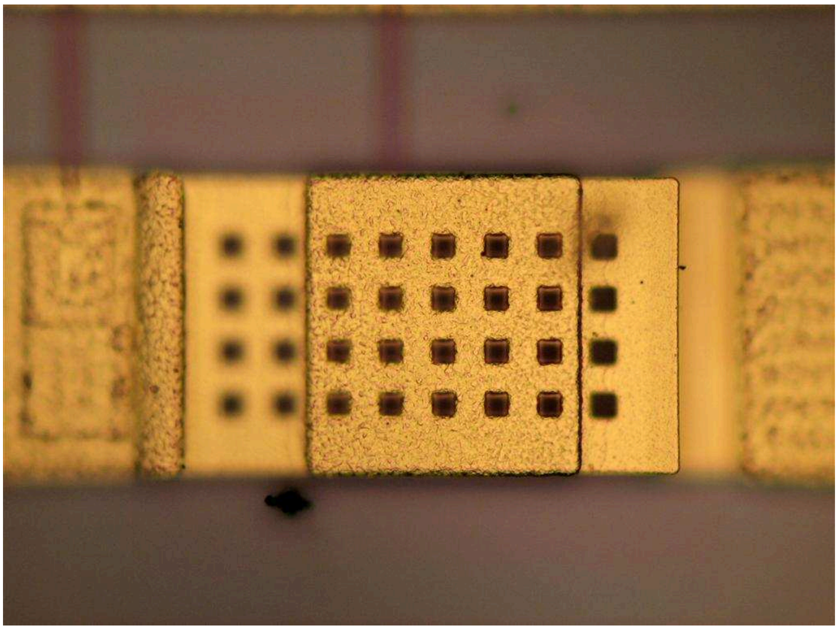

Figure 1.6: Detail of a cantilever structure. Holes on the suspended membrane are clearly visible

In Figure 1.6 it's possible to see the holes on the suspended membrane of a cantilever switch designed by the University of Perugia. In this case we have several squared holes of 10x10μ with a gap of 10μm.

1.2 Overview on Fondazione Bruno Kessler (FBK) fabrication process

The FBK process for MEMS structures is based on surface micromachining techniques and standard CMOS type processing sequences on a high resistivity silicon substrate. This is an eight masks process that has been developed in the last four years in order to obtain a reliable technology platform.
The whole process consists in about 200 single processing steps.
A scheme of the base line fabrication process is presented in Figure 1.7, here it's possible to see how all the main structures are realized, starting from the

easier resistors and capacitors up to the more difficult suspended membrane. A complete description of the different steps is presented hereunder:

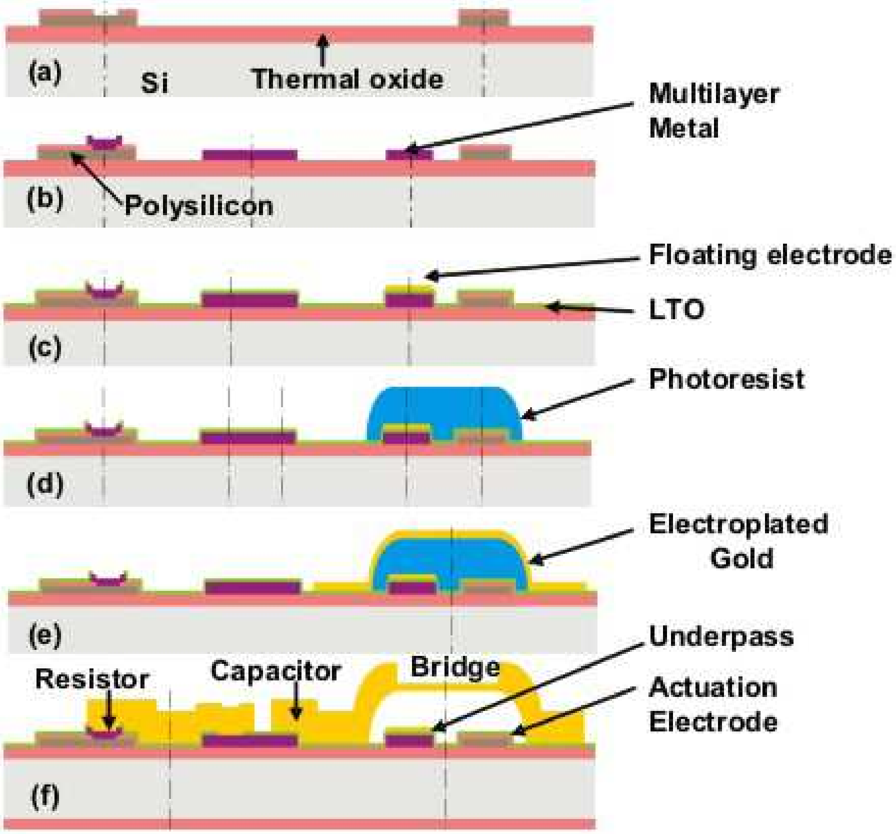

Figure 1.7: Schematic description of the different steps used by FBK form MEMS devices fabrication

(a) A 1000nm thick thermal oxide is grown as an isolation layer and then it is annealed in nitrogen in order to reduce the fixed charge. On the top of it, 630nm of polysilicon are deposited and then doped with Boron. A step at 925°C is necessary in order to diffuse the Boron. The final step consists in depositing 300nm of TEOS and opening the contacts through a plasma process.

(b) The multilayer underpass metal is deposited in this second phase. The different steps are: 30nm of Ti and 50nm of TiN deposited at 400°C, 410nm of Al1%Si and 60nm of Ti deposited at room temperature and finally an 80nm capping layer of TiN deposited at 300°C. This metallization scheme provides together a high conductive metal layer and a diffusion barrier for gold. The multilayer metal is then defined and etched.

(c) The multilayer created in the previous step is then covered with 100nm of low temperature oxide (LTO). The LTO and the last two layers deposited (Ti/TiN) are etched where the contact will be created. In these regions a 5nm thick Chromium adhesion layer followed by a 150nm Gold layer are deposited by PVD. The main purpose of this layer is to cover with a noble metal the exposed electrical contacts of the series ohmic switches in order to provide low resistive electrical contacts.

(d) A sacrificial layer of 3μm is deposited in order to realize the air gap under the suspended membrane and, on the top, a 2.5/25nm thick Cr/Au layer is deposited by PVD as a seedlayer for electrochemical Au deposition.

(e) The movable air bridges are defined using a 5μm thick positive resist. After an exposure to oxygen plasma at 80°C a 1.8μm thick gold layer is selectively grown.

(f) In this final step the CPW lines and anchor posts for the movable air bridges are defined with 5μm thick positive resist. Again the wafers are exposed to oxygen plasma and then a 3.8μm thick gold layer is selectively grown. Later a sintering in nitrogen at 190°C for 30 minutes is performed in order to provide the gold layers with the appropriate tensile stress. Finally the air bridges are released with a modified plasma etching process in order to avoid sticking problems.

The base line process described above can be adapted to special needs by introducing process variants or specific design options. Normally the process variants regard parameters or materials of a single layer.

In the last years different variations of single process parameters of the base line technology have been experimentally tested and the variations on single process parameters potentially relevant for reliability are: the resistivity of the poly-silicon, the thickness of the polysilicon layer, thickness of the bridge/CPW layer and air gap height.

1.3 University of Bologna designs

The different switches realized in the PRIN project have been designed by the University of Bologna and manufactured by the FBK. These devices can be divided in four different groups depending by the beams shape and the type of connections as shown in Figure 1.8. Defining V_{ACT} as the voltage that makes the suspended membrane collapse down and the "off state" and the "on state" positions as the states in which $V_{BIAS} < V_{ACT}$ and $V_{BIAS} \geq V_{ACT}$, the four different topologies are described below:

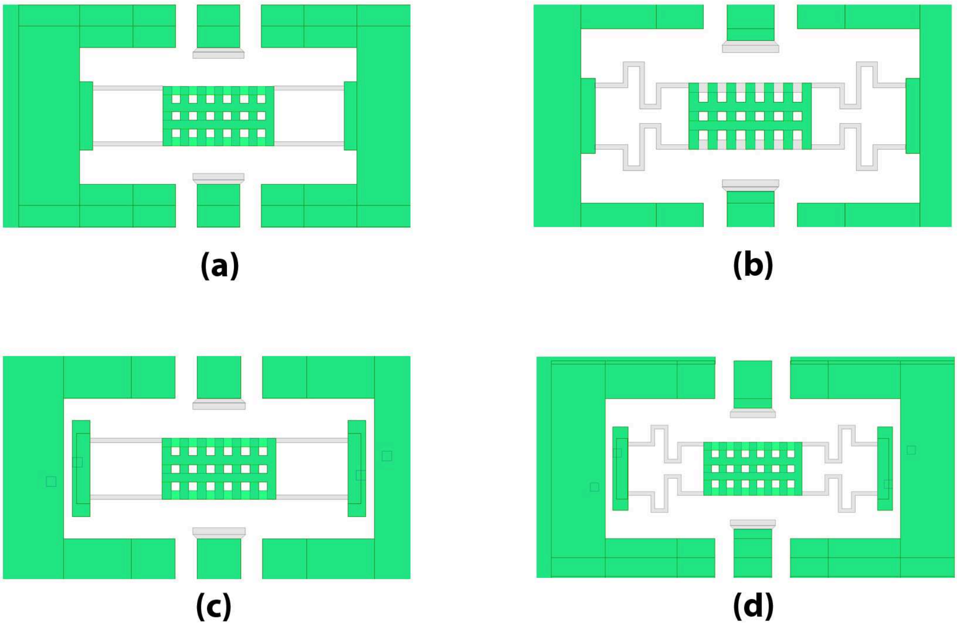

Figure 1.8: Simplify structures of University of Bologna switches

(a) Ohmic shunt straight beams based switch

In the off state position this device can be considered a transmission line while it becomes a short to ground in the on state position. Because of the straight beams, the spring constant is higher than in the meander beams devices and this implies a higher restoring force that cause a higher actuation voltage. V_{ACT} is around 40-60V.

(b) Ohmic shunt meander beams based switch

In the off state position this device can be considered a transmission line while it becomes a short to ground in the on state position. Because of the meander beams, the spring constant is lower than in the straight beams devices and this implies a lower restoring force that cause a lower actuation voltage. V_{ACT} is around 10-20V.

(c) **Ohmic series straight beams based switch**
In the off state position this device can be considered an open circuit while it becomes a transmission line in the on state position. Because of the straight beams, the spring constant is higher than in the meander beams devices and this implies a higher restoring force that cause a higher actuation voltage. V_{ACT} is around 40-60V.

(d) **Ohmic series meander beams based switch**
In the off state position this device can be considered an open circuit while it becomes a transmission line in the on state position. Because of the meander beams, the spring constant is lower than in the straight beams devices and this implies a lower restoring force that cause a lower actuation voltage. V_{ACT} is around 10-20V.

An interdigitated topology has been adopted for signal underpass and actuation electrodes in order to reduce the oxide charging phenomena as explain [14]. To avoid the contact between the suspended membrane and the actuation pad, poly dummy rectangular bricks are used and the contact is allowed only between the bridge and the signal electrodes. In certain devices, characterized by a thick bridge, a $5\mu m$ thick gold layer is used for the suspended membrane to improve its rigidity while the four suspending beam springs are made of a thinner $1.5\mu m$ gold membrane.

Because of the advantages presented in the previous section, these devices have a perforated suspended membrane with squared holes of $20x20\mu m$ with $20\mu m$ separation.

An external actuation pad is used to apply the voltage at the actuation electrode.

Typically this devices are realized with flat metal-to-metal contacts between the transmission line and the suspended membrane. These wide contacts guarantee a low series resistance and excellent RF performances even though, because of nano-irregularities on the gold surface and to hardening or pitting of the contact during multiple actuations, it can happen that only a small part of this area gets in contact leading to a sensible increase of the series

resistance and a degradation of the RF performances.
To avoid this kind of problems, a dimple can be used instead of the flat metal-to-metal contact. The advantage of the cone structure is the bigger pressure on the contact because of the smaller surface. Increasing the pressure makes the series resistance lower and more repeatable improving the RF performances.

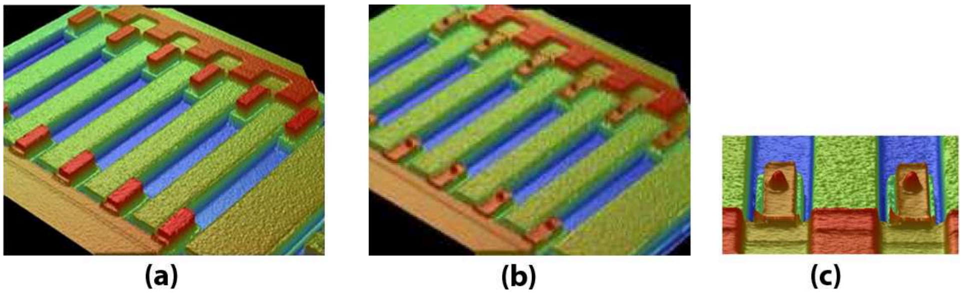

Figure 1.9: (a) in red flat metal-to-metal contact (b) in red dimples (c) close view of dimples, the cone shape is clearly visible

In Figure 1.9 the two different topologies of contact are presented. In (a) the small red "bricks" represent the flat metal-to-metal contact, the contact surface is big but unfortunately it tends to become irregular using the device. In (b) the structure with the dimples (red) is presented, the cones are quite small but they guarantee better long term performances. In (c) there is a close view of dimples, the cone shape is clearly visible.

1.4 University of Perugia designs

The devices presented in this thesis and designed by the University of Perugia have been manufactured by FBK in the contest of the ESA project. These devices here presented are not the final ones but just prototypes because the ESA project is not yet finished. Nevertheless, some of them are really promising structures from a reliability point of view.
The devices can be divided in four different topologies presented hereunder:

- **Series ohmic winged switch with stopping pillars (PSX)**
  This device consists of a metallic bridge, isolated from the ground planes of the co-planar waveguide, suspended above an interrupted

signal line. In Figure 1.10 the structure of the device and the performances are shown. The external actuation and ground pads are omitted.

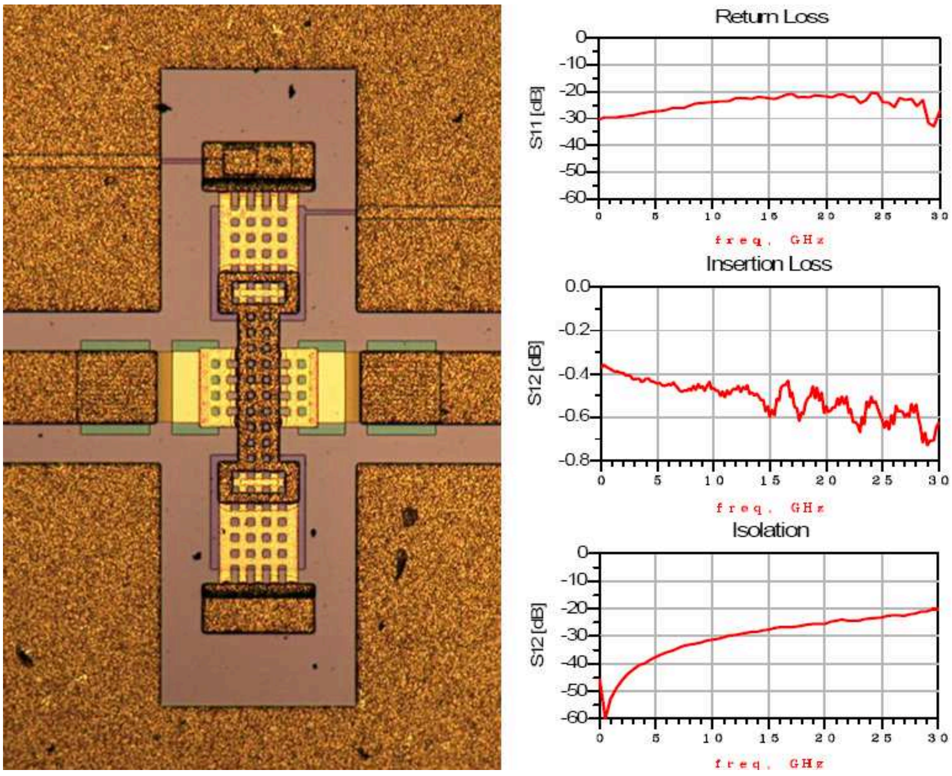

Figure 1.10: Picture and performances of a PSX switch

In the up state the bridge is suspended above the interrupted signal line providing very high and wideband isolation better than 20dB from DC up to 30GHz. On the contrary, in the down state the bridge is lowered by the electrostatic force applied through the actuation pad in order to contact the two ends of the transmission line.
The device exhibits very good RF performances as shown in Figure 1.10. The measured pull-in voltage is about 50V.

- **Boosted ohmic shunt switch (BO)**
  This device has been designed to have a very high capacitance ratio, defined as the ratio between the capacitance in the unactuated state and the capacitance of the actuated state. In this case the values are: $C_{up} = 21fF$, $C_{down} = 4.55pF$, $C_{down}/C_{up} > 200$.

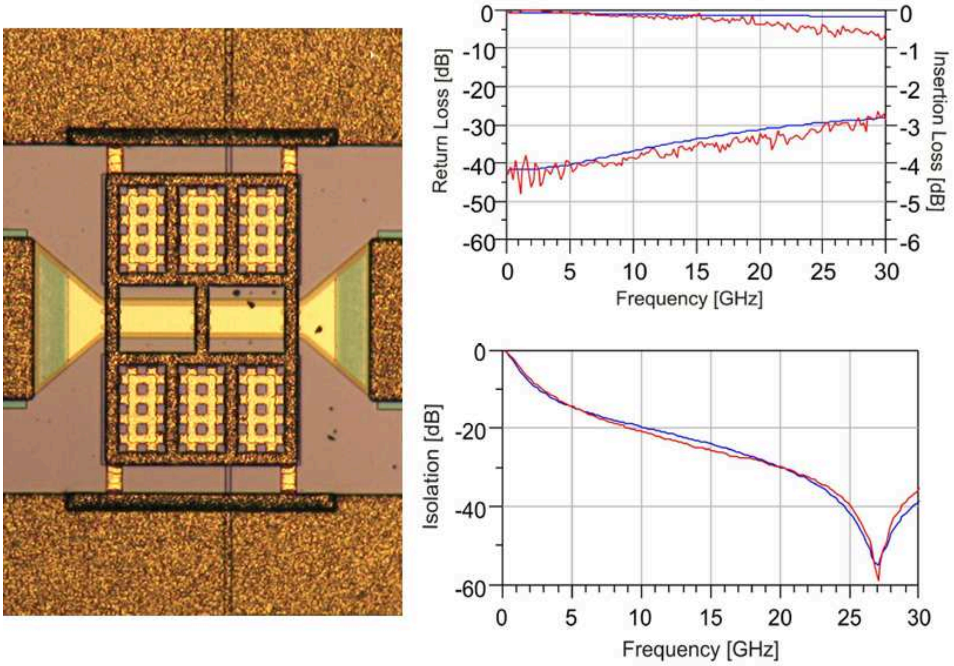

Figure 1.11: Picture and performances of a BO switch. Blue lines and red lines represent the simulated and measured performances.

In Figure 1.11 the structure of the suspended membrane and the performances, both simulated (blue lines) and measured (red lines), are shown. As it is possible to see from Figure 1.11, there is an excellent correlation between the simulation performances the measured ones. Typically actuation voltage is about 30V.

- **Spring anchor ohmic switch (BAT)**
  It has been designed with the aim to obtain a winged stopping pillars switch (like PSX) but with a lower actuation voltage. From Figure 1.12 it is easy to see that the suspended membrane structure it is almost the same of the PSX switch, the only difference is in the way the bridge is connected at the substrate. Here we have a sort of meander beams, similar to the one already seen in the PRIN devices, while in the PSX we have straight beams. Because of the lower spring constant, lower actuation voltages have been measured, between 15V and 30V. From an RF point of view, the spring anchor ohmic switch has shown a very good behavior as it is possible to see from Figure 1.12.

Moreover, also in this case, there is a good correlation between the simulation performances the measured ones. There is just a problem at low frequencies where the probable presence of parasitic oxide on the via contact tends to block the RF signal inverting the RF device expected behavior.

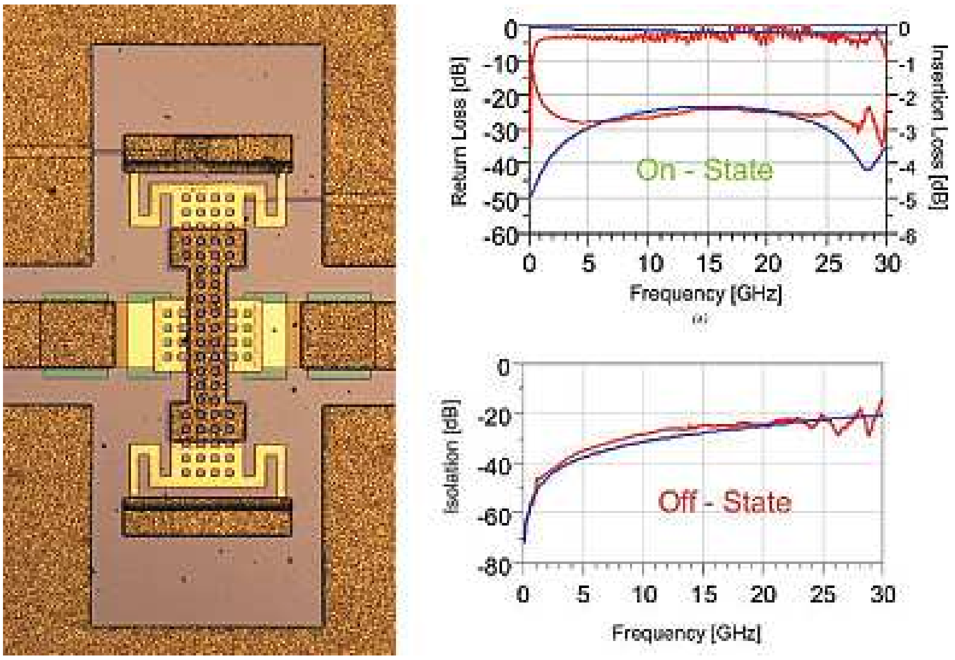

Figure 1.12: Picture and performances of a BAT switch. Blue lines and red lines represent the simulated and measured performances.

- **Cantilever switch (CA)**

  It consists of a gold cantilever beam suspended above an interrupted coplanar signal line and anchored at one end. The working principle is the same as for PSX and similar performances are obtain with the exception of smaller loss. The measured actuation voltage is about 50V and the de-actuation voltage is about 40V.

  In Figure 1.13 the structure of the suspended membrane and the performances are shown. The external actuation and ground pads are omitted. In order to guarantee a repeatable and low contact resistance dimples have been placed in the contact area and the beam central part has been reinforced with thicker gold [10] [11]. The can-

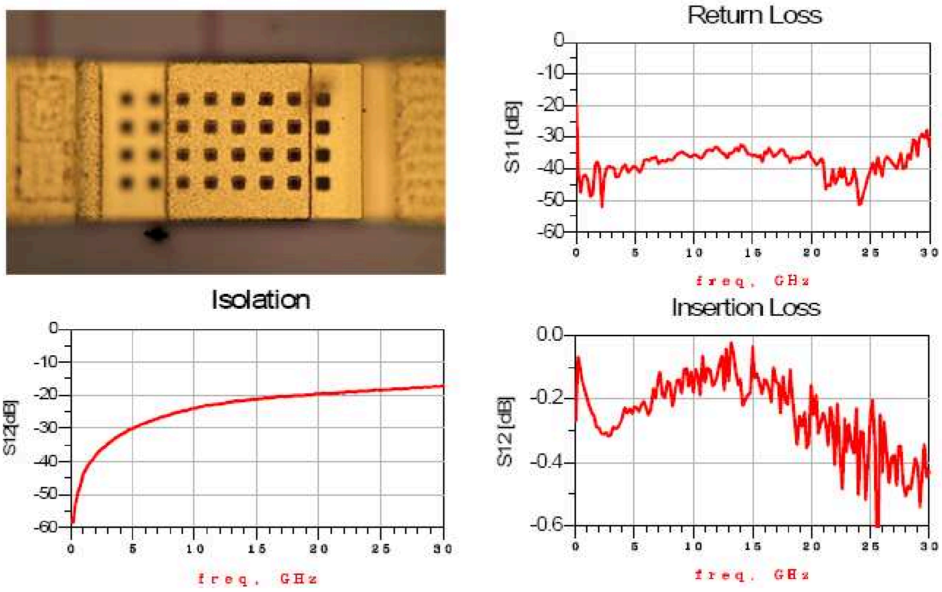

Figure 1.13: Picture and performances of a CA switch.

tilever switch has been manufactured without dielectric in order to limit charge trapping problems.

Also in these devices several holes have been realized on the suspended membrane for the reasons already explained in section 1.1.3. In this case the holes are $10\mu m$ x $10\mu m$ with $10\mu m$ separation.

1.4.1 Stopping Pillars

As it will be presented in the next chapter, the main failure mechanisms of MEMS switches have been found to be dielectric charging and microwelding of the ohmic contacts [7]. To overcome these problems different solutions can be implemented but the most efficient is to realize dielectric-free actuation pads avoiding the contact between the bridge and the pad [8] [9] realizing stopping pillars on the activation pad. This solution has been adopted since it does not require any changes in the FBK MEMS process.
Since the actuation structure is not covered with any dielectrics, it is extremely important to design a reliable structure to avoid the contact between the actuation structure and the suspended membrane.
Assuming the bridge to be like an infinite plate of thickness t supported by

dotlike pillars positioned in the vertexes of squares, the bridge displacement above the stoppers can be estimated using the following equation:

$$f = 0.063 \left(\frac{p}{E}\right)\left(\frac{a^4}{t^3}\right) \tag{1.7}$$

where E is the Young Modulus, t is the plate thickness, a is the length of the square sides, and p is the applied load which, in the case of electrostatic actuation, is equal to:

$$p = \frac{F_e}{a^2} = \frac{1}{2} \cdot \frac{\varepsilon_0 A_{pad}}{V^2 a^2} \tag{1.8}$$

where F_e is the electrostatic force, ε_0 is the vacuum permittivity, V is the voltage applied on the area A_{pad}. The equation 1.8 is an overestimation of the real bridge deformation because it does not consider the bridge tensile stress and the spring constant. In Figure 1.14 the bridge deformation as a function of the pillars height with respect to the activation pad is shown. In (a) the bridge deformation when a is set to $40\mu m$ and V is varied from 20V to 60V with a step of 10V is presented while in (b) the variation of f as a function of the spacing a for a fixed applied voltage V of 50V is shown. According to the data presented in 1.14 (b), a $0.55\mu m$ thick, $40/50\mu m$ spaced pillars should ensure the bridge isolation from the activation pad.

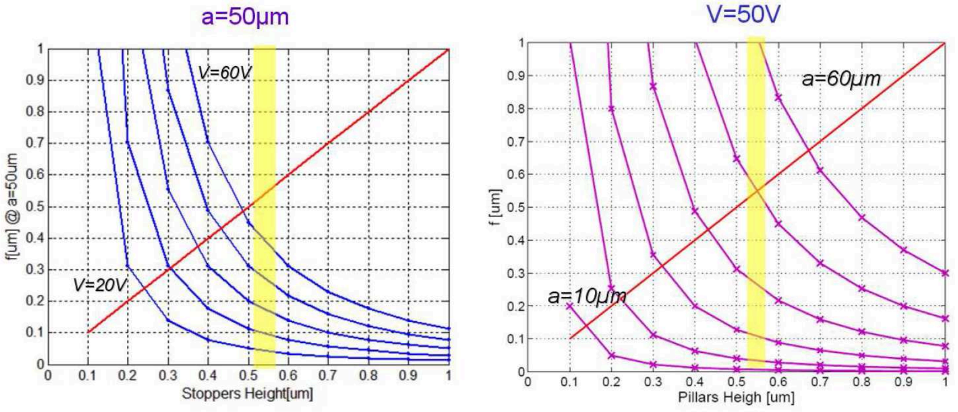

(a)

(b)

Figure 1.14: Bridge deformation f as a function of the pillars height. (a) Fixed spacing a = $50\mu m$ and increased voltage V (from 10 V to 60 V, 10 V step). (b) Fixed voltage V = 50V and increased spacing a (from $10\mu m$ to $60\mu m$, $10\mu m$ step)

As well as reducing the dielectric charging phenomena, the stopping pillars lead to an increased pull-out voltage V_{po} which is in general a desirable effect since it indicates an increase of the beam restoring force. The ratio V_{po}/V_{pi} is given by the following expression which has been derived by the formula for the standard dielectric-covered pads.

$$V_{po}/V_{pi} = \sqrt{\frac{27}{4}\frac{(d_0 - d_a)\left(d_a + \frac{d_e}{\varepsilon_r}\right)^2}{\left(d_0 + \frac{d_e}{\varepsilon_r}\right)}} \tag{1.9}$$

Where d_0 is the total air gap above the pad, d_a is the pillars height with respect to the actuation pad, d_e is the thickness of the dielectric covering the pad and ε_r is the dielectric constant. From Figure 1.15 it is possible to see that for a $0.55\mu m$ stopper the pull-out Vpo/Vpi ratio is close to 0.5. It is important to consider that in standard dielectric switches the pull-out voltages values are not easily predictable due to the unknown in the adhesion forces between the dielectric covering the pad and the metal bridge. This problem can be overcome in the case of stopping pillars because such

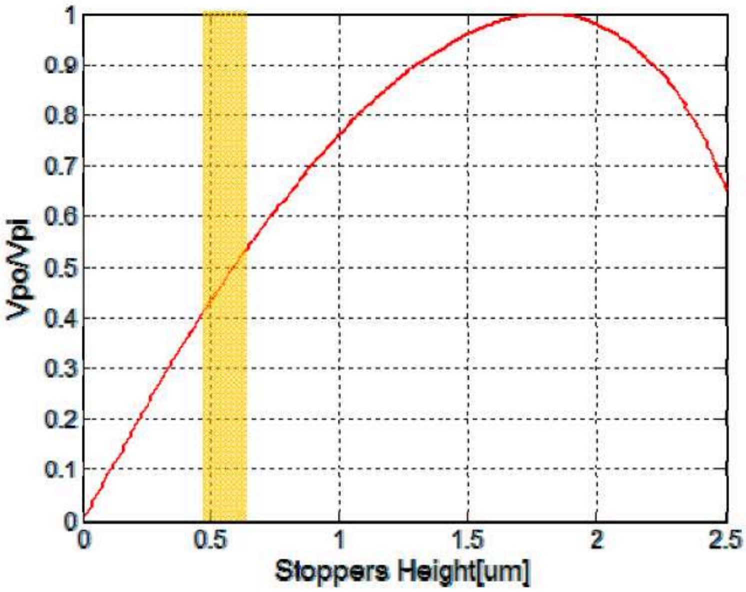

Figure 1.15: V_{PO}/V_{PI} ratio as a function of the pillars height for the case of dielectric-free electrode. The yellow line represent the working points for $0.55\mu m$ stopping pillars.

forces are not present and, for this reason, a better agreement between the theoretical and the actual value is expected.
New stopping pillars have been designed to be 4μm x 4μm large, 1.18μm thick bumps deposited on the substrate. The pad thickness is 0.63μm resulting in a stopper elevation of 0.55μm with respect to the electrode. The thickness of the contact bumps in ohmic switches is 0.63μm bigger than the stoppers height in order to guarantee low contact resistances. The pillar spacing is about 40-50μm. Figure 1.16 shows the layers that will be patterned for the realization of the contact bumps, the stoppers and the electrodes.

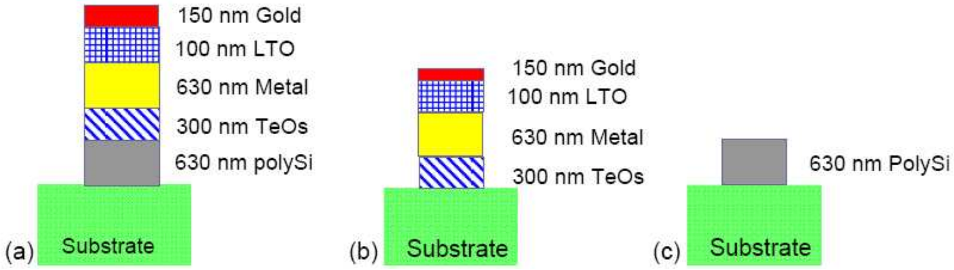

Figure 1.16: Layers constituting the contact bumps (a), the stoppers (b) and the electrodes (c).

Capitolo 2

Reliability analysis of RF-MEMS switches

Considering autonomous wireless communication systems for space applications, reliability and very low power consumption are two of the most important requirements and MEMS technology is extremely promising to meet this demand. In particular RF MEMS switches can be designed to operate in a wide range of frequencies from 0.1 to 100GHz with low power consumption.

RF switches designed with this technology have been demonstrated with low loss, low power consumption, low distortion, and higher off-state isolation as compared to p-i-n diodes or field effect transistors. However, before such switches can be used in commercial or spatial applications, they must demonstrate the ability to switch reliably over billions of cycles [12] [13], or, as in the case of a redundancy switch, to maintain their electrical, mechanical and RF performances for very long time. Unfortunately, long-term reliability of these devices is still an open question, since stable performances under a range of operational and environmental stresses has not been demonstrated yet. The coexistence of mechanical and electrical phenomena is the reason why the reliability of these devices is still an open question.

Furthermore, considering space applications, several issues concerning the radiation tolerance with respect to both total ionizing dose (TID) and single event effects (SEE) must be assessed before they may be successfully employed in radiation harsh environment.

Typical failure mechanisms of MEMS devices can be divided in three classes regarding the nature or the cause of the problem. Because of the electrical and mechanical nature of this kind of devices, some phenomena are also correlated. In the following sections, a description of the main reliability issues is reported, dividing the nature of the problem in electrical, environmental, and mechanical causes.

2.1 Electrical phenomena

2.1.1 Dielectric charging

Dielectric charging is probably the most common reliability issue impairing MEMS functionality and it consists in an accumulation of charge trapped in an insulator [15] [16] [17]. The charge trapped can be both positive or negative and it can be mainly created by two different mechanisms. The first one and the most common, is the presence of an high electric field across the insulator. This electric field can cause the injection of charge in oxide traps or interface states throw Poole Frenkel or Fowler-Nordheim tunneling. Another cause of charge trapping is the exposure to radiation that can induce electron-hole pairs in an insulator. If an electric field is present, these carriers can become trapped before they recombine.

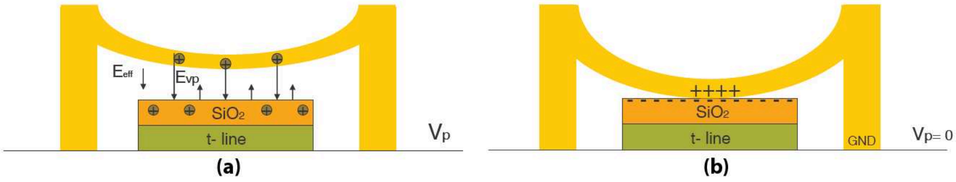

Figure 2.1: Schematic of charge trapped effects: screening (a) and stiction (b)

Dielectric charging can impact on the MEMS performances in the following ways:

- **Screening**
  The charge entrapped in the SiO_2 layer produces parasitic electric fields that can screen the effect of the applied voltage [18] [19] as represented in Figure 2.1 (a). This phenomenon typically leads to a variation of the actuation voltage because the voltage “felt” by the

suspended membrane can be higher or lower depending by the type of charge trapped (positive or negative). In the case of a bipolar actuation, charge trapping leads to a not symmetric actuation characteristic.

- **Stiction**
  The charge entrapped in the SiO_2 layer produces an electric field high enough to generate a strong force able to hold the bridge in the down-state position even when the external actuation voltage is set to 0V, see Figure 2.1 (b) [20]

2.1.2 Dielectric breakdown

A too high electric field across the insulator can cause a breakdown. We can distinguish two different types of oxide breakdown: the soft breakdown and the hard breakdown. The soft breakdown does not necessary compromise the functionality of the device and it can be seen as a sort of conduction path throw the oxide. The conduction path can be caused by traps distributed in the insulator and generated by the electric field or they can be already present because of imperfections during the deposition process. A soft breakdown usually implies an increasing of the leakage current. On the contrary, the hard breakdown completely destroy the device and it usually occurs to coincidence with an electrostatic discharge.

2.1.3 Power handling

Considering a RF signal with a V_0 amplitude, the DC component can be calculated using the following equation:

$$V_{DC} = \frac{V_0}{\sqrt{2}} \tag{2.1}$$

and the power at the input will be

$$P_{RF} = \frac{V_0^2}{2Z_0} \tag{2.2}$$

Logical or physical reliability issues can happen if the RF signal power flowing through the switch (with a micrometric dimension of the structure) is too high.

A logical issue can be defined as a particular issue related to some malfunction of the device that can be auto-actuated even with no external voltage applied. Two different kind of logical issues can be distinguished:

- **Self-actuation**
  It happens when a strong RF signal has an high enough DC component that is able to accidentally actuate the device.
- **Latching**
  It happens when a strong RF signal has a DC component equal to the hold-down voltage. It is quite similar to the previous case but, in this one, the bridge will be no more released [21].

Physical issues are typically related to electromigration phenomena [22] caused by high current propagation within the transmission lines and within the upper membrane. The electromigration degrades the conductivity of the metallization causing an increase of the power dissipated through Joule's laws and a consequent increase of the local temperature.
Applying a RF signal the electromigration impact is different from the one in DC regime. Due to the skin effect, increasing the operating frequency leads to an higher concentration of the current lines.

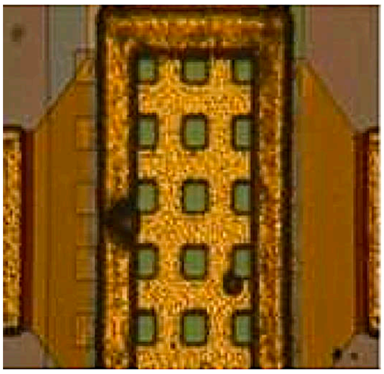

Figure 2.2: Suspended membrane of a RF-MEMS switch. Bubbles due to membrane fusion are clearly visible.

This concentration can easily cause line melting due to the material removal and the subsequent high temperature that it can reach. In Figure 2.2 it is possible to see an example of bubbles on the suspended membrane of a RF-MEMS switch caused by an high current flowing.

2.1.4 Contact resistance variation

This particular reliability issue typically affects resistive switches because of the presence of the ohmic contact. Its degradation bring to an increase of the contact resistance that lead to an increase of the temperature [35] at the contact point and finally to the failure of the switch. Furthermore, the increased resistance in the closed state can become comparable to the resistance exhibited in the open state, compromising the functionality of the switch because to distinguish between the open and the close state is impossible. The reduced size of the contact point increases the series resistance of the device degrading its electrical performances [23] [24].

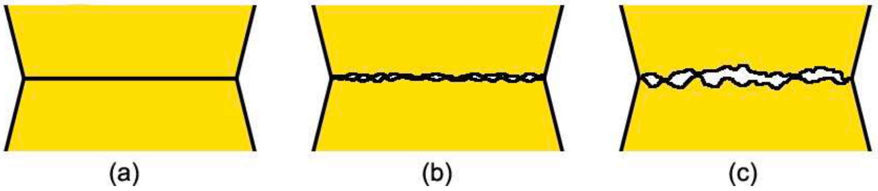

Figure 2.3: Simplify schemes of the contact possible configurations: theoretic (a), real contact of a new device (contact is not perfect because of roughness of the surfaces)(b), and finally the contact of a stressed devices (c)

In Figure 2.3 three different schemes of possible contact are reported. (a) can be considered as the theoretic contact between two surfaces completely flat. Unfortunately, because of the natural roughness of the material, the surfaces are never completely flat so the real contact of a new device can be described as in (b) where almost all the surfaces are in contact. The use of the device leads to a degradation of the contact as presented in (c). In this last case the real contact is extremely small causing an increase in the resistance.

2.1.5 Microwelding

The microwelding, or metal-to-metal welding, in RF-MEMS switches consists in the welding of the suspended membrane with the bottom part of the ohmic contact structure. This phenomenon can happen in all metals but it is easier in the soft ones, like gold, because of the lower melting point. The reduction of the contact point, combined with high forces and with the increase of the local temperature caused by the current flowing, can cause the welding of the two surfaces. We can distinguished two different types of microweldings like in the case of the oxide breakdown: a destructive welding and a non-destructive welding. The first case it is quite easy, the welding of the two surfaces is irreversible and they remain stuck. On the contrary, in the second case, there is just a small and partial welding of extremely small points on the surfaces but a transfer of material can happen lowering the quality of the contact and degrading the performances.

2.2 Mechanical phenomena

2.2.1 Fracture

Mechanical fracture is defined as the breaking of a uniform material into two separate sections. In MEMS it will usually leads to the catastrophic failure of a device, although there are some structures that will have more moderate performance degradation [25]. It is possible to define three different types of fracture:

Ductile It occurs in the ductile material and it is characterized by almost uninterrupted plastic deformation of the material.

Brittle It occurs along crystal planes and develops rapidly with little deformation.

Inter-crystalline It is similar to brittle fracture but it occurs along grain boundaries in polycrystalline materials, often beginning at a point where impurities accumulate.

Considering MEMS devices, brittle and inter-crystalline fractures are more common.

2.2.2 Fatigue

Fatigue is a failure mechanism caused by the cyclic loading of a structure below the yield or fracture stress of a material. This loading leads to the formation of surface micro-cracks that cause the slow weakening of the material over time and create localized plastic deformations.
Fatigue also causes a gradual change in the properties of a material. After repeated cycling, which is often on the order of billions of cycles, Young Modulus will gradually shift [25].

2.2.3 Stiction

This phenomenon occurs when two polished surfaces come into contact and they tend to adhere to one another because of metal-to-metal molecular forces preventing the suspended membrane from returning in the up-state position. While this fact is often unimportant in macroscopic devices, it becomes important in micrometer devices [25]. In the case of MEMS switches, this problem can be partially overcome trying to reduce the contact area and increasing the spring constant taking into account that increasing the spring constant the actuation voltage increases.

2.2.4 Wear

Wear is an event caused by the motion of one surface over another. It is defined as the removal of material from a solid surface as the result of mechanical action. While there are some mechanical operations, such as polishing and sharpening, that utilize wear in a constructive manner, wear is generally considered an undesirable effect in MEMS. Causes of wear are: adhesion, abrasion, corrosion, and surface fatigue [25].

2.2.5 Delamination

Delamination is a condition that occurs when a materials interface loses its adhesive bond. It can be induced by a number of means, from mask misalignments to particulates on the wafer during processing. It can also arise as the result of fatigue [25].

2.2.6 Stray stresses

These are failure mechanisms that are endemic to thin film structures. Stray stresses are defined as stresses in films that are present in the absence of external forces. In MEMS small stresses will cause noise in sensor outputs and large stresses will lead to a mechanical deformation. Thermal and residual stresses are the two sources of stray stress in MEMS [25].

2.3 Environmental phenomena

2.3.1 Humidity effects

Humidity can be considered a serious issue for MEMS structure. Surface micromachined devices are extremely hydrophilic for reasons related to processing and, for this reason, the surfaces in a humidity atmosphere will experience both condensation, which will create bending moment in structures, and capillarity forces, which will create stronger adhesive bonds than Van der Waals forces alone [25].

2.3.2 Temperature changes

Internal stresses in devices are extremely temperature dependent and for this reason temperature changes are a serious concern for MEMS. The temperature range in which a device will operate within acceptable parameters is determined by the coefficient of linear expansion. In devices where the coefficients are poorly matched, there will be a low tolerance for thermal variations [25]. The small number of data that have been published on this topic demonstrates actuation voltage variations in the range of $0.3-0.5V/^{\circ}C$ [26] [27]. Over a broad temperature range, this can lead to excessively large supply voltage variations.

In Figure 2.4 the variation of the gap capacitance and the variation of the actuation voltage as a function of the temperature for RF-MEMS switches is reported. The device has been fabricated on Pyrex glass substrates (Corning 7740) with copper posts, gold electrodes, and aluminum alloy membranes.

Additionally, operation at high voltages (necessary for low temperatures) can also adversely impact device reliability [28] . On the contrary, low temperatures can increase dielectric charging effects.

Beyond these issues, there are other difficulties caused by temperature fluc-

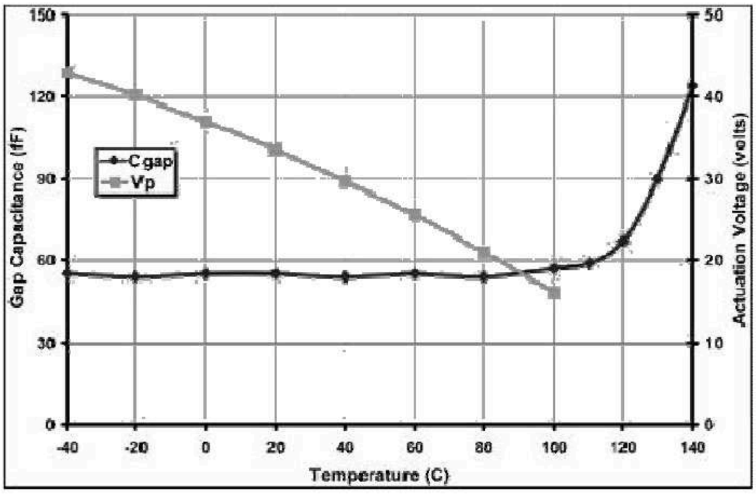

Figure 2.4: Measurement of gap capacitance (black) and actuation voltage as a function of temperature (grey)

tuations. Thermal effects cause problems in metal packaging, as the thermal coefficient of expansion of metals can be greater than ten times that of silicon. For these packages, special isolation techniques have to be developed to prevent the package expansion from fracturing the substrate of the device [25].

2.3.3 Radiation

It has long been known that electrical systems are susceptible to radiation and recent research has raised the possibility that mechanical devices may also be prone to radiation-induced damage. In particular the most sensitive devices are those where a mechanical motion governed by electric fields across insulators is present, such as electrostatically actuated cantilever bemas so RF-MEMS switches. Since insulators dielectric rupture, there is a distinct possibility that these devices will have decreased performance in the space environment. A further complication is the fact that radiation can cause bulk lattice damage and make materials more susceptible to fracture [25]. Recent work indicates that dielectric layers will trap charged particles, creating a permanent electric field that could interfere with the nominal behavior of the switch. Furthermore, some radiations can have an impact on the Young Modulus, changing the actuation voltage and the spring constant.

Region	Single event effects			Total dose		Charging		Plasma effects			
	Galactic cosmic rays	Trapped heavy ions	Solar energetic particles	Trapped radiation	Solar energetic particles	Surface charging	Internal charging	Ion sputtering	Scintillation	Plasma wave refraction	Surface erosion from O^+
Ionosphere	1	0	0	0	0	0	0	1	2	2	2
South Atlantic Anomaly	1	2	0	2	0	0	0	1	0	0	0
Inner radiation belt	1	2	0	2	0	0	0	0	0	0	0
Auroral zone	2	0	2	0	2	1	0	1	0	0	0
Polar cap	2	0	2	0	2	0	0	1	0	0	0
Plasmasphere	2	0	0	0	2	0	0	1	0	1	0
Plasma sheet	2	0	0	0	2	2	0	1	0	0	0
Outer radiation belt	2	1	2	2	2	2	2	1	0	0	0
Outer magnetosphere	2	0	2	0	2	1	2	1	0	0	0
Geomagnetic tail	2	0	2	0	2	0	0	1	0	0	0
Solar wind	2	0	2	0	2	0	0	1	0	0	0

Figure 2.5: Space environmental hazards in different regions of space (0: unimportant 1: relevant 2:important)

In Figure 2.5 a table presenting a list of space environmental hazards in different regions of space is reported.
Considering RF-MEMS switches, the most important events are presented in the first two columns: Single Event Effects and Total Dose. In the vertical axis there are different regions of the space starting from the nearest to the Earth (Ionosphere) up to the farest (solar wind or interplanetary space). In the horizontal axis different events are list, ordered roughly by the energy of the particles responsible for the hazards, decreasing in energy from left to right.
The color-coding and numbering represent approximate measurements of the importance of a particular phenomenon in a specific region. Note that this table does not consider the hazards of satellite drag, impacts from meteoroids or space debris, or satellite collisions. The drag is most important in low Earth orbit, while meteoroid impacts and satellite collisions can happen anywhere [31]. Figure 2.6 shows the distribution of the 299 anomaly records versus the anomaly type. The “other” category includes plasma, micro-meteoroid impacts, and uncategorized solar energetic particle effects. Effects from electrostatic discharge had the largest number of records, while single event effects and radiation damage together account for $\sim 33\%$ of the cases [30].

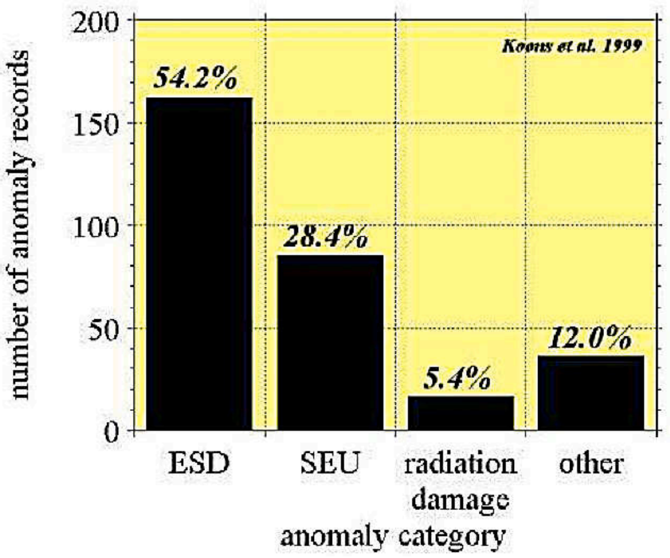

Figure 2.6: Breakdown of Single Event Up-set (SEU) and radiation damage anomaly records (data from Koons-99)

Figure 2.7 shows the different categories of Single Event Up-set (SEU) and radiation damage. The largest subcategory is the uncategorized SEU: their origin may have been galactic cosmic rays or solar energetic particle events for which there was no detailed correlation done with the environment. Radiation damage anomalies are infrequent compared to the other effects. Within the radiation damage category, there are only three records ($\sim 1\%$) corresponding to total radiation dose. Such a low frequency might therefore reflect conservative limits in radiation modeling and conservative shielding. The anomaly records did not quantify effects such as cost or delays in launches of similar, follow-on spacecraft. The most visible effect is mission loss or termination, and Koons et al. listed 11 such cases [32].
For reference, three of these losses were diagnosed as SEU effects, one as total radiation dose. The only other effect that can be easily quantified in the Koons et al. survey is the time it took the spacecraft operators to recover from the anomaly. It appears clearly that focusing on the impacts of single event effects and radiation damage (roughly one third of the anomaly cases) is extremely important. In the case of SEU events, automatic recovery using on-board correction algorithms can be probably considered for the events of minimal duration [30].

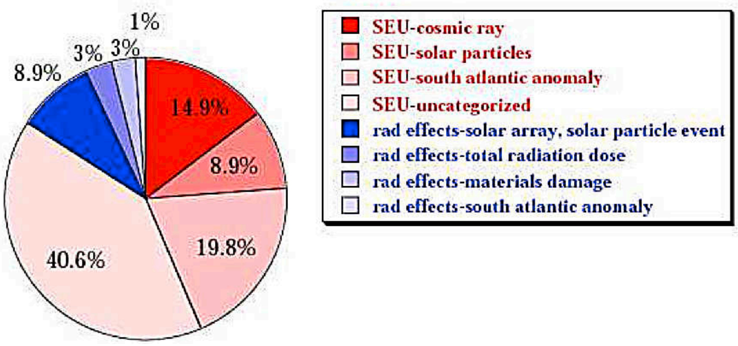

Figure 2.7: Breakdown of Single Event Up-set (SEU) and radiation damage anomaly records (data from Koons-99)

2.3.4 Vibrations and shocks

Vibration is a large reliability concern in MEMS. Due to the sensitivity and fragile nature of many MEMS, external vibrations can have disastrous implications. Either through inducing surface adhesion or through fracturing device support structures, external vibration can cause failure. Long-term vibration will also contribute to fatigue. For space applications, vibration considerations are important, because devices are subjected to large vibrations in the launch process [25].

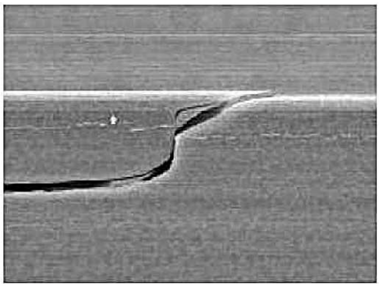

Figure 2.8: Crack in single crystal silicon support beams caused by vibrations from a launch test

In Figure 2.8 it is possible to see an example of crack in single crystal silicon support beams caused by vibrations from a launch test. A shock differs from a vibration because it is a single mechanical impact instead of a rhythmic event and it creates a direct transfer of mechanical energy across the device.

It can lead to both adhesion and fracture. Shock can also cause wire bond shearing, a failure mode common to all semiconductor devices [25].

2.3.5 Particulates

Particulates are fine particles, that are prevalent in the atmosphere. These particles have been known to electrically short out MEMS and can also induce stiction. While these particles are normally filtered out of the clean room environment, many MEMS are designed to operate outside the confines of the clean room and without the safety of a hermetically sealed package. As a result, devices must be analyzed to ensure that they are particle-tolerant before they can be used as high-reliable devices in environments with high particulate densities.
Another area in which contaminants cause problems is in adhesion. Proper device processing requires most materials interfaces to be clean in order to have good adhesion. If dust particles are present, then the two materials will be weakly bonded and are more likely to have delamination problems.

2.3.6 Electrical Over-Stress (EOS)/Electrostatic discharge (ESD)

EOS refers to a particular working situation in which voltage or current overcome the nominal values of the device, on the other side, ESD typically occurs when a device is improperly handled. These effects are known to be catastrophic in traditional solid state circuits and also in MEMS.

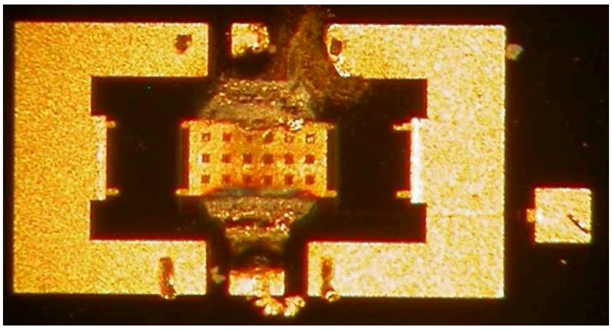

Figure 2.9: Example of ESD event in a RF-MEMS switch.

Figure 2.9 shows an example of ESD event in a RF-MEMS switch. It appears obvious that this kind of event is completely irreversible and it compromises the functionality of the device.

Despite for traditional solid state circuits a lot of in-circuit protection structures have been presented, MEMS technology does not typically exhibit the ability to implement similar protection schemes. For this reason, the reliability to ESD of such devices must be thought starting from the design phase.

Capitolo 3

Switches characterization and cycling stress

In electronic, a switch is a particular device that can be normally open or closed controlling the flowing of a signal. A RF-MEMS switch behaves in the same way, it can let the RF signal pass from one port to the other or deviates it toward ground. Depending on the configuration, two topologies can be distinguished: series or shunt switches.

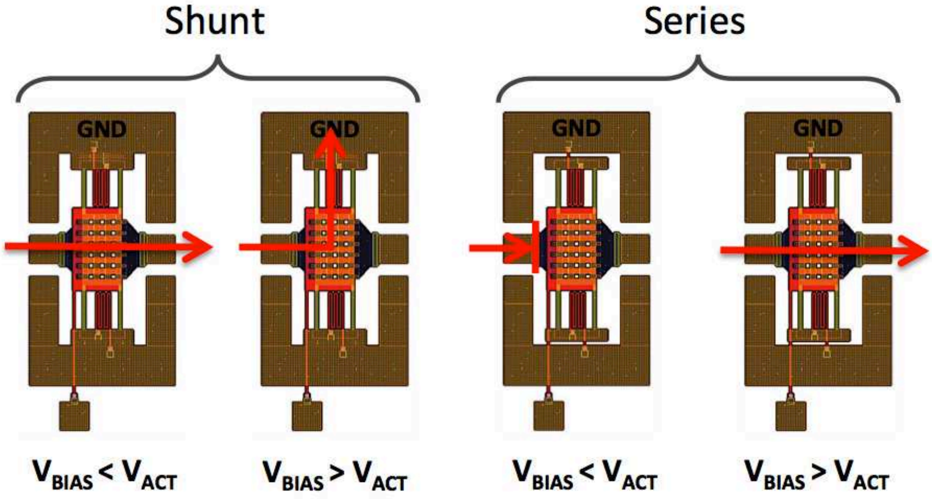

Figure 3.1: Simplify scheme of the two topologies, series and shunt, with different bias voltages. In red the path of the RF signal

In Figure 3.1 a simplify scheme of the two topologies, series and shunt, with different bias voltages is presented. The red arrows indicate the path of the RF signal.

In the shunt configuration the transmission line is uninterrupted between the input and the output. When the bias voltage is smaller than the actuation voltage the suspended membrane is in the up state position and the RF signal goes directly from the input to the output. On the contrary, when the voltage applied is higher than the actuation voltage, the bridge collapses down touching the transmission line and the RF signal goes to the GND pad. This topology can be considerated as a normally closed switch.

On the other hand, for the series configuration, the transmission line is interrupted between the input and the output. In this case, when the bias voltage is smaller than the actuation voltage the RF signal is stucked at the input. On the contrary, when the voltage applied is higher than the actuation voltage, the RF signal can go from the input to the output thanks to the bridge that close the circuit. This device can be considered as a normally open switch.

Both topologies can be realized with ohmic or capacitive structures, depending on whether the device has a metal-to-metal contact or a Metal-Insulator-Metal (MIM) structure. While ohmic switches work thanks to the direct contact of two metals, the transmission line and the suspended membrane, capacitive devices have a thin dielectric layer deposited on the transmission line avoiding the direct contact. In this case the short circuit is obtained with the increasing of the MEMS capacitance that implies a decrease of the impedance following the equation:

$$Z_{capacitor} = \frac{1}{j\omega C} = \frac{1}{j2\pi fC} \tag{3.1}$$

3.1 Principles of electrical characterization

In the matter of characterization, there are several parameters to consider in order to have a first idea of devices performances. MEMS structures, as presented before, have different characteristics typical of electrical devices but also of mechanical devices.

The first parameter to measure is the actuation voltage, or better the voltage at which switch's parameters can be considered good.

Not in all devices this parameter corresponds to the voltage at which the suspended membrane contacts the transmission line. Sometimes an higher force is needed in order to make a good contact between the transmission line and the suspended membrane, probably because of the roughness of the material, or the shape of the stopping pillar, or residual stresses.

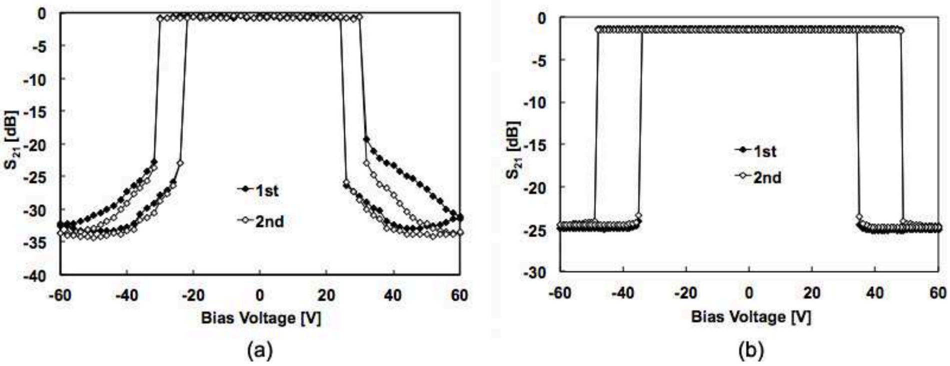

Figure 3.2: S_{21} parameters curves for two different devices. (a) slow actuation (b) fast actuation. Two measurements have been performed in series

In Figure 3.2 an example of two different actuation curves is presented. The graphics show the S_{21} parameters, the transmitted power coefficients, for two different series RF-MEMS switches. In (a) the suspended membrane close the contact at $\sim 35V$ while the performances continue to improve up to $60V$. On the contrary, in (b) the point of maximum performances corresponds to the point in which the suspended membrane close the contact. From this example it appears quite clear that the best performances are not always reached at the actuation voltage but sometimes it is necessary to increase the bias voltage up to 50%. Once the actuation voltage has been calculated, it is important to verify if the RF performances are good and if they can satisfy the specifications. This is possible measuring the S_{12} and S_{21} parameters that are respectively the reflected and the transmitted power coefficients.

The last parameter that should be considered is the actuation time, defined as the delay time between the biasing of the device and the measurement of the RF signal at the output port. If these devices are used as redundancy switches, this parameter is not so important because, in general, 1s is the maximum time accepted for the reconfiguration. 1s results to be more than enough for a fresh device, being the actuation time around $50\mu s$ as it is possible to see from Figure 3.3

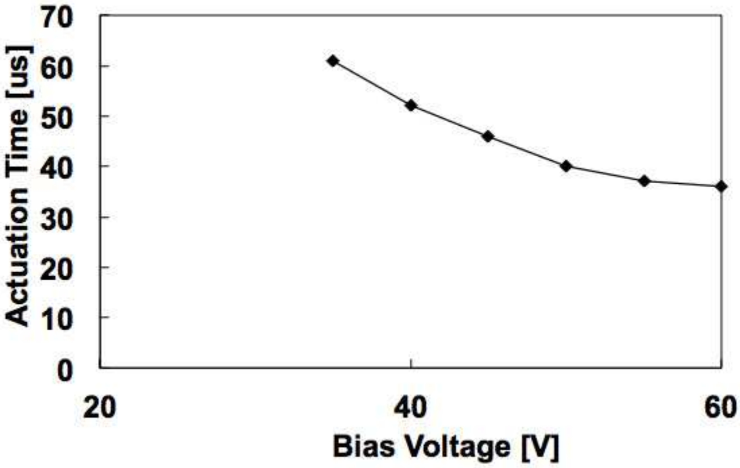

Figure 3.3: Actuation time versus actuation voltage for a series meander based MEMS switch

Figure 3.3 shows the actuation time versus the actuation voltage for a series meander based MEMS switch. Increasing the voltage applied makes the device actuate faster because of the greater force applied to the suspended membrane.

At $35V$, the voltage necessary to actuate the device, the actuation time is around $60\mu s$ while at $60V$ it becomes less than $40\mu s$. This is a reduction of more than $20\mu s$, around 33% of the original actuation time.

From this first analysis of MEMS switches parameters it seems that increasing the voltage applied improves the performances of the switch (better RF parameters and lower actuation time). Nevertheless increasing too much the voltage applied can compromise the reliability because of charging problem or EOS or ESD events as it will be analyzed later.

3.2 DC Sweep

The first measurement to perform with a fresh device is the so called “DC Sweep”. It gives useful information such as RF performances, through the measurement of the S_{12} and S_{21} parameters, actuation and deactuation

voltages and possible presence of charge trapped throw the analysis of the symmetry of the curves.
The scheme of the instruments used to perform these measurements is shown in Figure 3.4

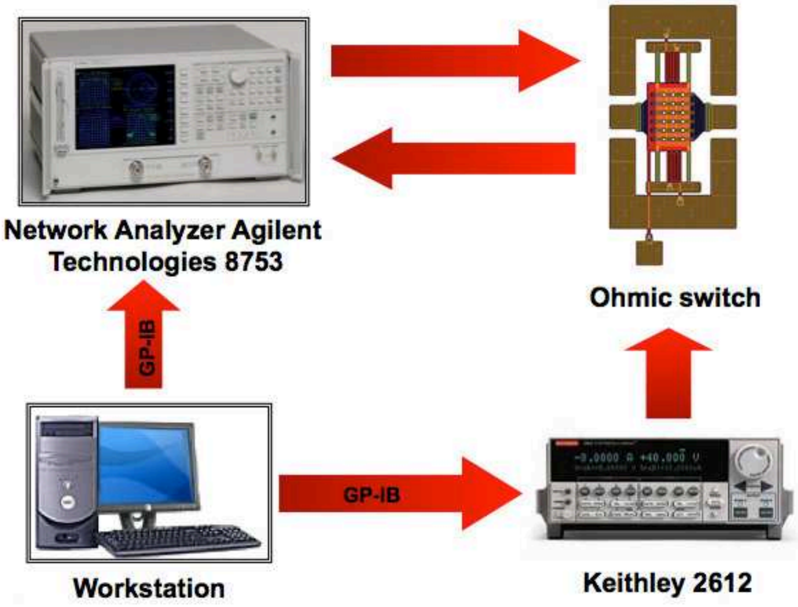

Figure 3.4: Scheme of the DC Sweep set up

The Keithley is used as external voltage supplier in order to bias the devices and, at the same time, to measure the current absorbed. The Network Analyzer Agilent Technologies 8753 can be used for signal up to $6GHz$ and it measures the S-parameters.
All the instruments are connected through a GP-IB cable making possible to fully control them and set all the different parameters with an ad-hoc realized Labview program.
All the data measured are automatically saved with Labview and processed with Microsoft Excel through a Macro written in Visual Basic.
The Labview front panel of the program used for the DC Sweep is reported in Figure 3.5.
All the most important parameters can be set with Labview, such as the maximum voltage to apply, the power and frequency of the RF signal, the number of sweeps that have to be done and so on.
At the same time it is also possible to monitor in real time the S-parameters

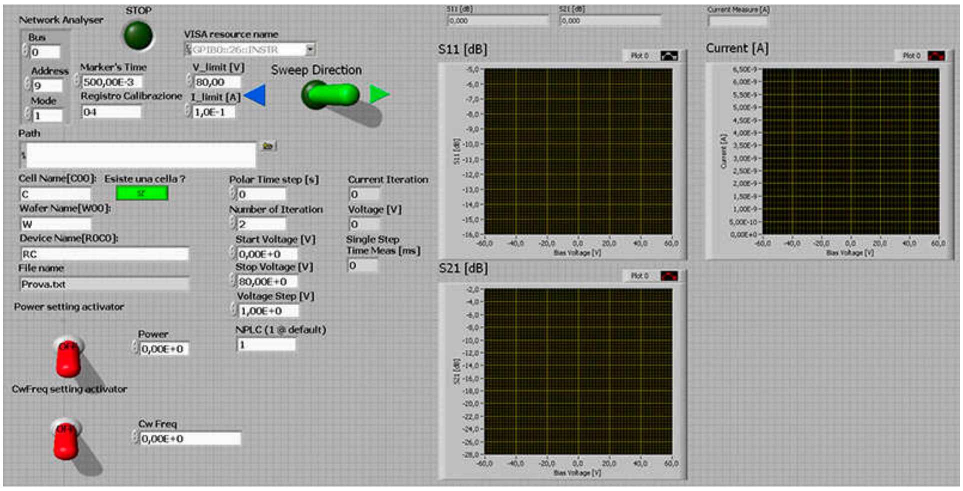

Bus
0
Address
9
Mode
1
Marker's Time
500,00E-3
Registro Calibrazione
04
VISA resource name
GPIB0::26::INSTR
V_limit [V]
80,00
I_limit [A]
1,0E-1
Path
Cell Name[C00]:
C
Esiste una cella ?
SI
Wafer Name[W00]:
W
Device Name[R0C0]:
RC
File name
Prova.txt
Power
0,00E+0
Cw Freq
0,00E+0
Polar Time step [s]
0
Number of Iteration
2
Start Voltage [V]
0,00E+0
Stop Voltage [V]
80,00E+0
Voltage Step [V]
1,00E+0
NPLC (1 @ default)
1
Current Iteration
0
Voltage [V]
0
Single Step Time Meas [ms]
0
S11 [dB]
0,000
S21 [dB]
0,000
Current Measure [A]

Figure 3.5: Front Panel of the Labview program used for the DC Sweep

and the current absorbed from the device. It is extremely important to monitor this last parameter in order to discover possible leakages or find the causes of a malfunction.
The graph of the voltage applied at the device is shown in Figure 3.6. Different voltage steps are applied at the device and for each step the S-parameters are measured. The voltage starts from 0, it is increased up to V_{max} (part 1 of the curve) then it is lowered down to 0 and then again to

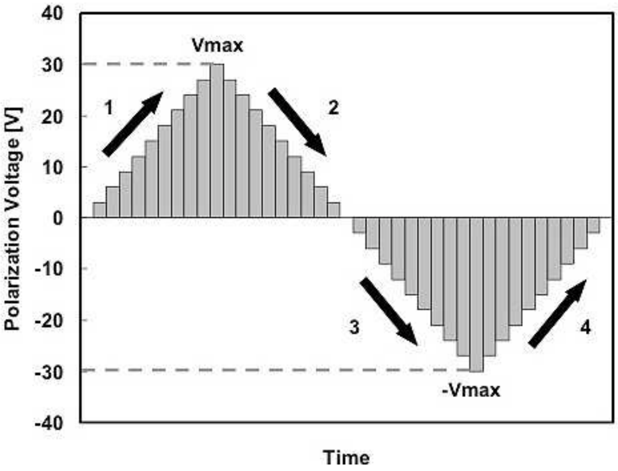

Figure 3.6: Evolution in the time of the voltage applied at the device during the DC Sweep

$-V_{max}$ (part 2 and 3 of the curve) and finally the voltage increases again going back to 0 (part 4 of the curve).
This measurement leads to the classical hysteresis like diagram reported in Figure 3.7

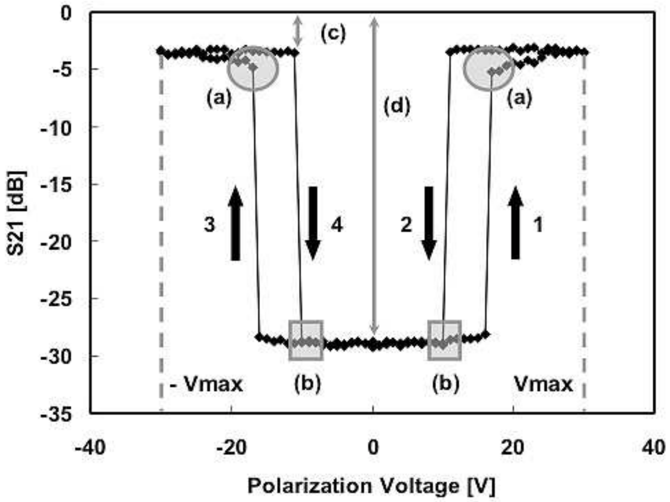

Figure 3.7: Classical DC sweep result for a RF-MEMS switch

In Figure 3.7 the four different parts of the DC Sweep are reported (1-4). Furthermore, it is possible to calculate the actuation voltage (a), the deactuation voltage (b), the S-parameter (c) and (d), and the presence of charge trapping through the analysis of the symmetry.
In order to not influence the performances of the device under test, the measurement process is performed as fast as possible, just few seconds are necessary to obtain a full characterization.
This measurement is quite easy but it is also a powerful method to analyze ohmic RF-MEMS switches.

3.3 Cycling stress measurement set-up

Cycling stress is one of the most common reliability test used for RF-MEMS switches. It consists in applying several pulses at the device monitoring the evolution of the S-parameters as a function of the number of cycles. Thanks to this stress it is possible to monitoring charge trapping and contact degradation.

The scheme of the instruments used to perform these measurements is shown in Figure 3.8

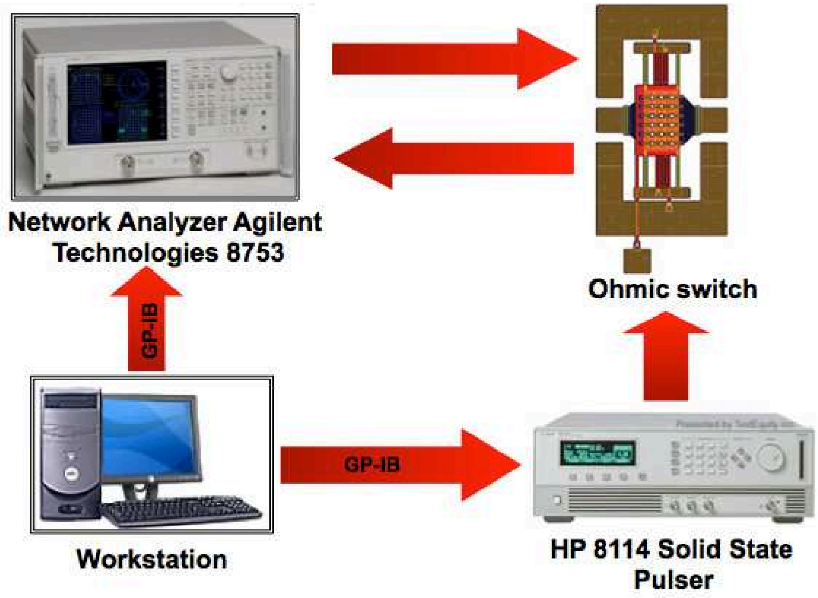

Figure 3.8: Scheme of the Cycling stress set up

The Solid State Pulser HP8114 is used to apply cycle of pulses at the device while the same Network Analyzer used for the DC Sweep is used to measure the S-parameters.

As for the previous set-up, also in this case all the instruments are connected through a GP-IB cable making possible to fully control them and set all the different parameters with an ad-hoc realized Labview program.

The Labview front panel of the program used for the Cycling stress is reported in Figure 4.1.

As well as setting all the different parameters of the stress, with the Labview program the measure of the S-parameters at every step and the general evolution during the stress can be monitored.

Unfortunately, because of the slowness of the Network Analyzer to perform a measurement, to monitor the S-parameter after every pulse is not possible. To do this kind of stress a maximum frequency of 10Hz should be used making the stress extremely long. 10 millions of cycles at 10Hz require 1 million of seconds, approximately 11 days. For this reason the S-parameter are monitored after a series of cycles, 10, 100, 1000, 10000 and 50000. 50000

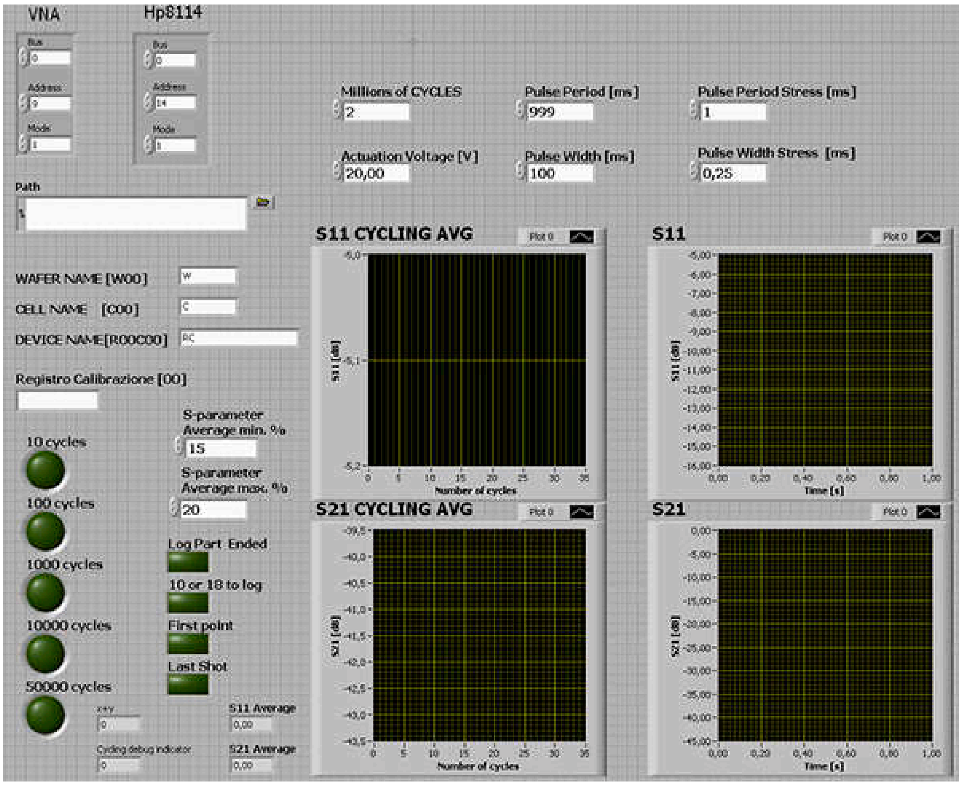

VNA: Bus 0, Address 9, Mode 1

Hp8114: Bus 0, Address 14, Mode 1

Millions of CYCLES: 2

Pulse Period [ms]: 999

Pulse Period Stress [ms]: 1

Actuation Voltage [V]: 20,00

Pulse Width [ms]: 100

Pulse Width Stress [ms]: 0,25

WAFER NAME [W00]: W

CELL NAME [C00]: C

DEVICE NAME[R00C00]: RC

S-parameter Average min. %: 15

S-parameter Average max. %: 20

x+y: 0

Cycling debug indicator: 0

S11 Average: 0,00

S21 Average: 0,00

Figure 3.9: Front Panel of the Labview program used for the Cycling stress

cycles is the limit of the programmable pulser.

Since the probability of a failure, for an electronic device, is greater in the first phase of stress, the following scheme of pulses has been used: $10 \times 10 - 10 \times 100 - 10 \times 1000 - 10 \times 10000 - 20 \times 50000$ for 1111100 pulses in total. The cycling frequency has been set to 1KHz with a duty cycle of 25% obtaining a pulse width of $250 \mu s$.

The actuation time of the devices need to be considered when choosing the frequency of the pulser. For sure the minimum pulse width can not be smaller than the actuation time otherwise the switch does not have the time to actuate, devices considered in this thesis have an average actuation time of $60 \mu s$. Moreover, a certain amount of time is necessary for the fully stabilization of the suspended membrane. $250 \mu s$ results to be a good choice.

The last parameter that need to be chosen is the voltage of the pulses. As it will discuss later, increasing this parameter seems to improve the reliability performances defined as the capacity of the switch to survive to an high

number of cycles. However, it creates charge trapping problems.
An example of data obtained with the cycling stress is shown in Figure 3.10

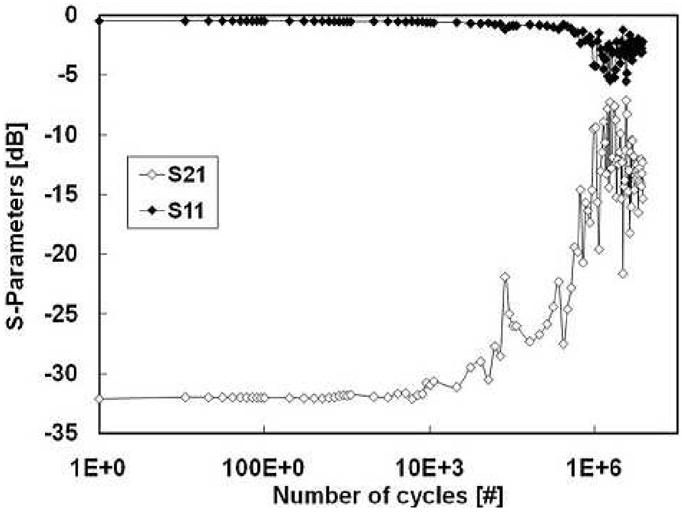

Figure 3.10: Example of data obtained with the cycling stress. S-parameters as a function of the number of cycles.

Looking at the graph shown in Figure 3.10 three different regions can be distinguished. In the first one, from 0 to about 10^3 cycles, the S-Parameters remain constant, from 10^3 to 10^6 they get worse and finally, in the third region, after 10^6 it is difficult to distinguish between S_{12} and S_{21} parameters. It means that there is almost no difference between the signal transmitted and reflected, making the device useless.
With this kind of plot it is easy to analyze the cycling reliability of devices obtaining an idea of when the contact starts getting worse and at which rate.
Cycling stress do not only impairs the contact but also general performances because of the charge accumulated during the stress. Throw the plot of Figure 3.10 it is not possible to have an idea of the amount of charge trapped because only the S-parameters at a specific voltage are plotted without caring about actuation or deactuation voltage. To have an idea of the charge it is necessary to perform a complete DC Sweep and to compare it with the original DC sweep.
An example of comparison between the DC sweep of a series RF-MEMS

switch before (pre) and after (post) the cycling stress is presented in Figure 3.11.

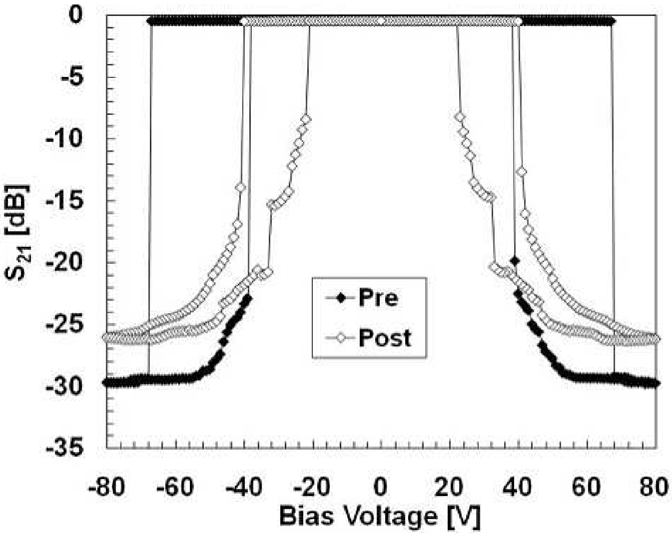

Figure 3.11: DC Sweep before and after the cycling stress of a series RF-MEMS switch

From the two DC Sweeps plotted in Figure 3.11 it is possible to clearly distinguished the two different degradation process: contact degradation and charge trapping.

The first process is recognizable because of the upward translation of the curves, the cycling impaired the contact quality and the S_{21} parameter started getting worse.

Concerning the charge trapping, this phenomenon can be recognized by a narrowing of the curve. Looking at Figure 3.11, the actuation voltage for the fresh device was around $\pm 70V$ while the deactuation voltage was around $\pm 40V$. After the cycling stress the actuation and deactuation voltages are respectively $\pm 40V$ and $\pm 20V$, it means a narrowing of almost 50%.

Figure 3.12 shows the different DC Sweep curves obtained at every step of the cycling stress for a shunt RF-MEMS switch. In this case only the upward translation of the curves is visible while the actuation and deactuation voltages remain almost the same. It means that, for this device, after 1 million of cycles there is not charge trapped but only a significant degradation of the contact.

Considering that the voltage applied during the sweep goes from $0V$ to V_{max}

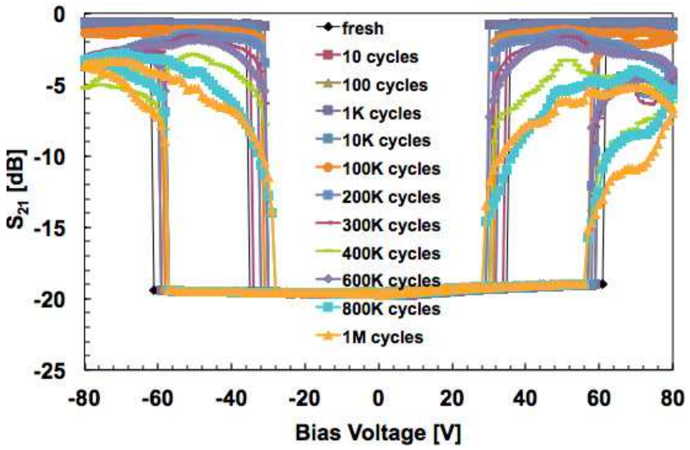

Figure 3.12: DC Sweep before and after the cycling stress of a shunt RF-MEMS switch

to $-V_{max}$ and then again to $0V$, it seems that there is a sort of partial recovery of the contact quality after the first actuation.
As a matter of fact the right part of the curves results to be lower than the left part.

3.4 Main results for different switches

The previous two measurements have been performed on all the devices considered in this thesis, both designed by the University of Bologna and by the University of Perugia.

3.4.1 Meander and straight beams based devices

The influence of the suspension shape on the electrical parameters and on the reliability of series and shunt RF switches designed by the University of Bologna has been studied. The attention has been focused on how different spring constants influence the electrical parameters of RF-MEMS switches, in terms of pull-in voltage, pull-out voltage, and evolution of scattering parameters during the DC sweep. The robustness to cycling stress has also been studied, considering different movable structures and bias voltages.
There are two main differences in the tested devices. The first difference is the shape of the suspended gold springs: meander based (type (a)), Figure

3.13 (a), or straight beams (type (b)), Figure 3.13 (b). The second difference is the type of membrane/transmission line contact: flat surfaces instead of dimple based. The optical profilometer image of a dimple based series RF-MEMS switch is reported in Figure 3.13 (c).

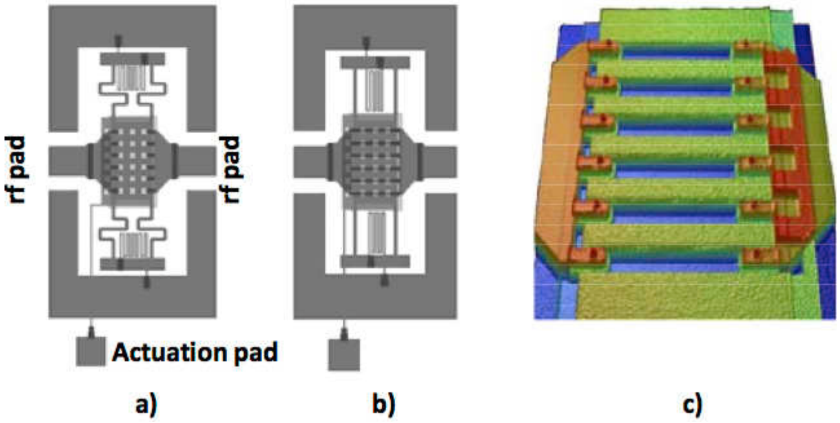

Figure 3.13: Tested devices layout: (a) meander based suspensions, and (b) straight beam suspensions. Optical profilometer image (after removal of the suspended membrane) of a series switch with dimples (c)

The DC sweep characteristic of the meander based series switch is reported in Figure 3.14. Thanks to the low spring constant value, given by the meander shaped anchors, type (a) devices, both shunt and series topologies, have exhibited very low values of actuation and release voltages ($|V_{ACT}| \approx 12V, |V_{REL}| \approx 6V$).

These devices have shown good RF performances (S-parameters measurement conditions: $RF_{freq} = 6GHz$, $RF_{power} = 0dBm$), and, as indicated by the graph symmetry, are not particularly affected by charge trapping phenomena. Straight beams devices (higher spring constant value), have exhibited a sudden actuation and higher values of both actuation and release voltages, as shown in Figure 3.15.

Series type (b) devices have exhibited an actuation voltage $|V_{ACT}|$ around 36V and a release voltages $|V_{REL}|$ around 18V. Also type (b) devices have shown good RF performances ($RF_{freq} = 6GHz$, $RF_{power} = 0dBm$), and almost no charge entrapment.

Comparing Figure 2 and Figure 3, it is clear that meander based switches

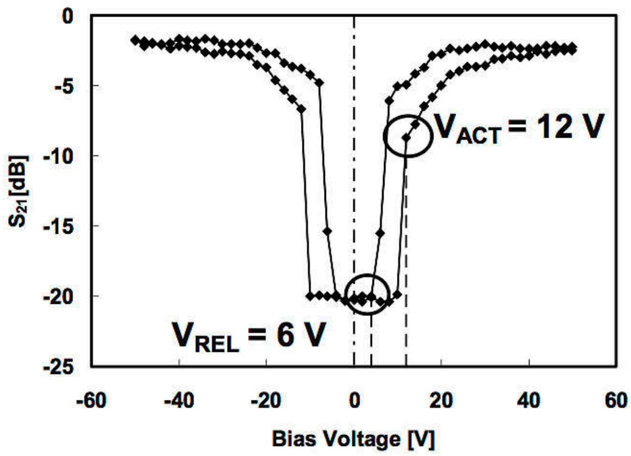

Figure 3.14: DC characteristic of a meander based switch

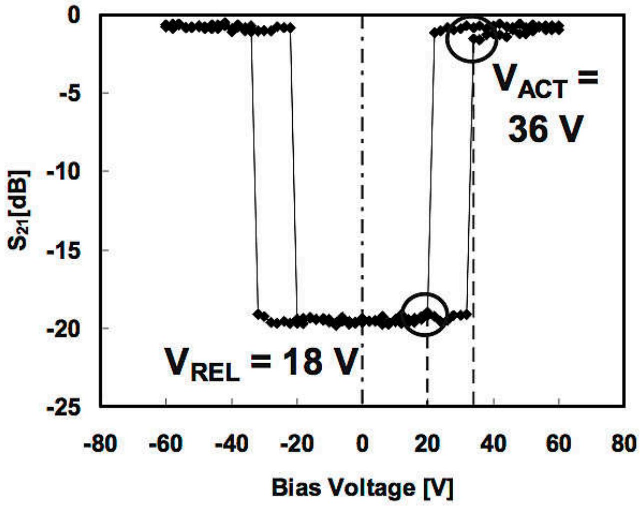

Figure 3.15: DC characteristic of a straight beams based switch

exhibit a soft evolution of the S21 parameter in the transition from the up-state position to the actuated state, contrary to the sudden actuation of straight beams devices. This behavior could be explained by the contact force obtained with the applied bias voltage. As postulated in [33], when the membrane is in the down-state position, the force on the pull-down electrode is not the same as the force on the contact points. In fact, the force at the contact points is about $30\% - 60\%$ of the pull-down force, with the remaining force contributing to membrane flexure and the reaction force at the anchors. This means that if the difference between $|V_{ACT}|$ and $|V_{REL}|$ is low the resulting electrostatic force is used to contrast the springs restoring force instead of improve the metal-to-metal contact. This fact leads to an increase in the bias voltage to achieve similar results in the contact resistance (or S_{21} parameter) between meander based and straight beam based switches. This also explains the difference observed between the two DC characteristics.

Another aspect that must be considered is the quality of the metal-to-metal contact at different actuation voltages. When a low actuation bias is applied, the surface roughness leads to an high series resistance value. On the contrary, increasing the actuation bias, the electrostatic force is strong enough to flatten the asperities between the metal-to-metal contact leading to an improvement of contact and then to a reduction of the series resistance value with a direct improvement of the S_{21}.

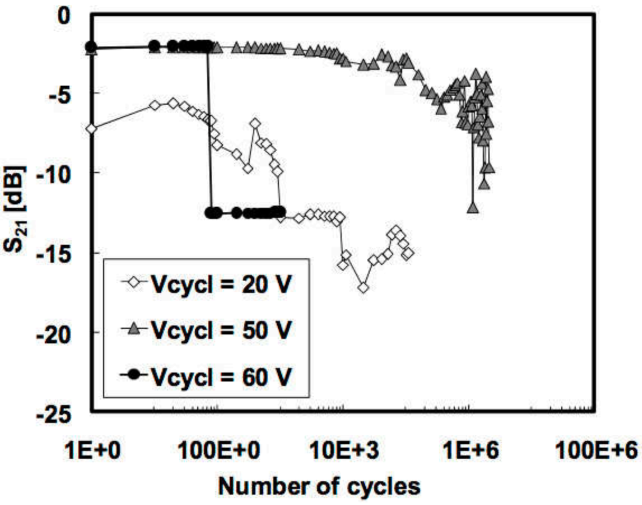

Figure 3.16: Parameters evolution during cycling stress for meander based devices at different stress voltage. $RF_{freq} = 6GHz$, $RF_{power} = 0dBm$

The S_{21} parameter evolution of a meander based series switch during cycling stress at different actuation voltages (V_{cycl}) is reported in Figure 3.16.

This type of devices exhibits a very poor cycling behavior at low cycling voltage, in this case $V_{cycl} = 20V$, in terms of both S_{21} values, and number of cycles (just few hundreds).

Increasing the stress voltage at $V_{cycl} = 50V$, the RF performance improves because of the better metal-to-metal contact as previously described, and the switch is able to reach around 10^6 cycles with low S_{21} parameter degradation. Nevertheless, a further increase of the actuation voltage up to 60V drastically reduces the lifetime of the device to about 100 cycles. This fact clearly indicates the necessity of finding an optimum bias voltage that needs to be high to improve the metal-to-metal contact, but not too high to not compromise the reliability.

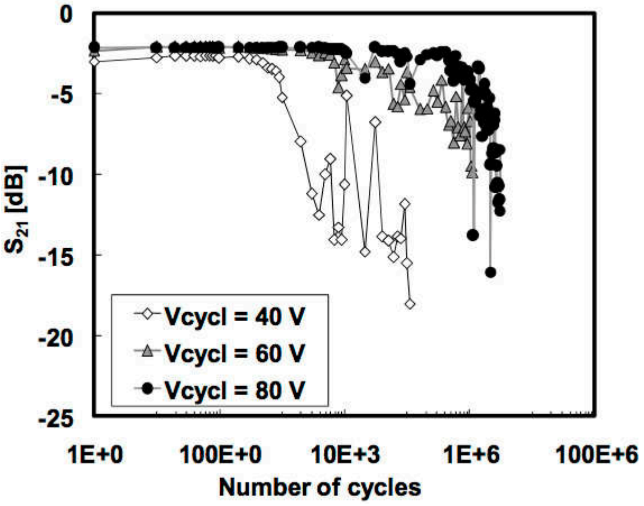

Figure 3.17: Parameters evolution during cycling stress for straight beams based devices at different stress voltage. $RF_{freq} = 6GHz$, $RF_{power} = 0dBm$

Straight beams based devices have also exhibited the same improvement on the reached number of cycles increasing the stress voltage as it is possible to see from Figure 3.17. In this case, at $V_{cycl} = 40V$, the device reached around 10^3 cycles, at $V_{cycl} = 60V$ around 10^5 cycles, and at $V_{cycl} = 80V$, around 10^6 cycles.

A possible explanation of the metal-to-metal contact degradation is given in [33] and seems to be caused by the presence of hardening and pitting phenomena. This contact degradation has been observed in all the typologies of the tested devices, both with and without dimples. The optical profilometer images showing the degradation of the bottom contacts of shunt straight beam based switch with dimples are reported in Figure 3.18, with a comparison between a fresh device (a), and after 10^6 cycles at $V_{CYCL} = 60V$. Comparing the pictures, it is clear the damage induced by cycling stress to the dimples structures, leading to an heavy degradation of the metal-to-metal contact, that increases the series resistance value.

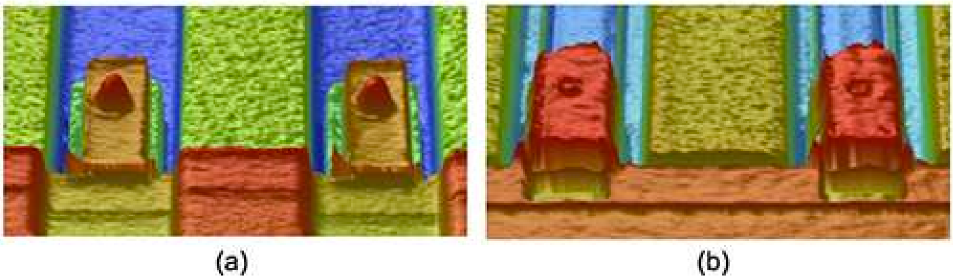

Figure 3.18: Optical profilometer images of a shunt straight beams based switch with dimples fresh (a), and after cycling stress (b)

3.4.2 PSX

Three different types of series ohmic winged switch with stopping pillars (PSX) devices have been stressed with cycling measurements: PSX1, PSX2, PSX5. All these devices differ only in the activation pad while the contact points between the suspended membrane and the transmission line has been realized as already discussed in 1.4.1.

DC characteristics of these devices are reported in Figure 3.19.

Figure 3.19 (a) shows the DC characteristic of the PSX1 device, the actuation voltage is $\sim 40V$ and the deactuation voltage is $\sim 22V$. The characteristics are quite symmetric, there is just a little shift on the right that become smaller during the second sweep maybe because of a small amount of charge trapped. The actuation is very good and fast resulting in a “clean” DC characteristic.

Figure 3.19 (b) shows the DC characteristic of the PSX2 device, the actuation voltage is $\sim 44V$ and the deactuation voltage is $\sim 24V$. Also in this case there is a little bit of asymmetry that disappear after the first sweep. The DC characteristic continues to be a very good one.

Finally, Figure 3.19 (c) shows the DC characteristic of the PSX5 device, the

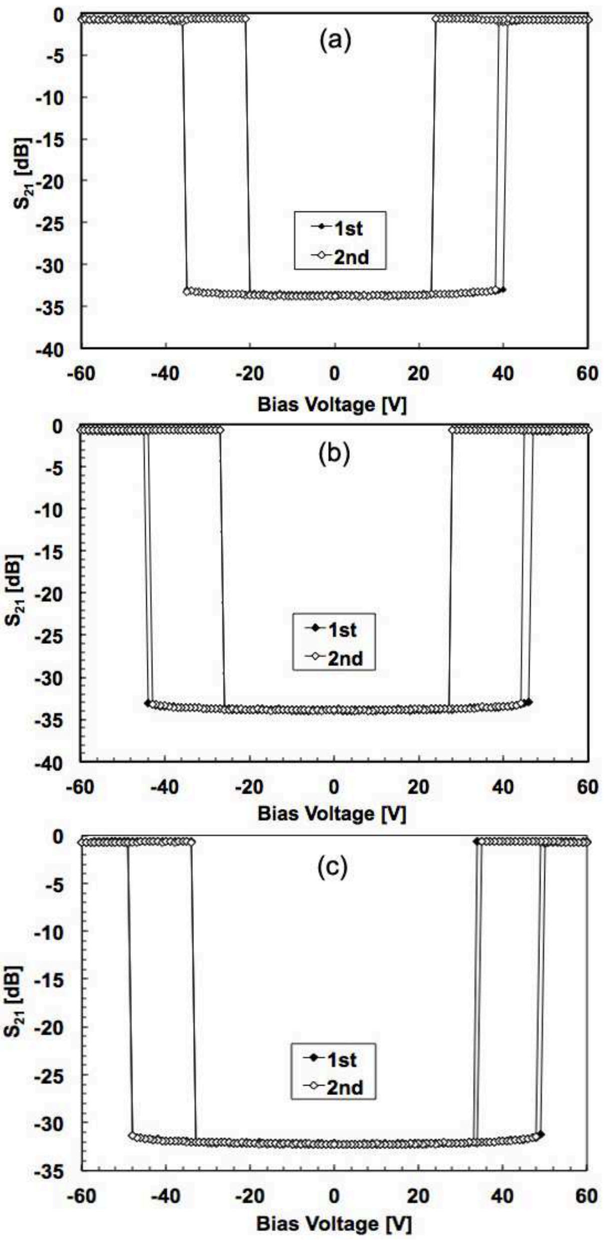

Figure 3.19: DC characteristic of PSX1 (a) PSX2 (b) and PSX5 (c) devices

actuation voltage is $\sim 46V$ and the deactuation voltage is $\sim 28V$. In this case there is no asymmetry and the DC characteristic is closed to an ideal one.

For all these devices the RF performances are very good and stable.

Looking at Figure 3.19 it is possible to see a trend for the actuation and deactuation voltages. Going from PSX1 to PSX5 the voltages increase. This increase is caused by the different structure of the activation pad that is bigger in PSX1, smaller in PSX2 and even smaller in PSX5. Reducing the area of the activation pad leads to an increase of the voltage that need to be applied in order to actuate the device.

The same devices have been submitted to cycling stress up to 1 million of cycles with $V_{pulse} = 60V$. Considering their use as redundancy switches, the capability to survive to billions of cycles is not the bigger priority, this is the reason why 1 million of cycles can already be considered a good test. The results are reported in Figure 3.20

PSX1 device exhibits some problems at the contact already in the first part of the stress. After only 10 cycles the S-parameters are lower and they continue getting worse during all the stress. After 10K cycles S_{11} and S_{21} are almost the same and after 1 million of cycles the "window" is completely closed with $S_{11} < S_{21}$. This is not a very good reliable result.

Looking at Figure 3.20 (b), PSX2 device, the situation seems to improve. The first effect of the cycling stress only appears after 100 cycles but they become relevant only after 10K cycles. At the end of the stress S_{11} and S_{21} parameters are not yet swapped even if they are quite similar. From a reliable point of view this type of device seems to be better than the previous one but it is not ideal yet.

Finally the results for PSX5 are presented in Figure 3.20 (c). In this case the device presents a very good behavior if compared with the other two typologies. Only after 100K cycles a small reduction of the S-parameter is visible and after 1 million of cycle we can consider the switch still working. Several measurements have demonstrated that PSX5 devices exhibit good performances from a cycling point of view but also they seem to not suffer of charge trapping as it will be discuss later in the long term analysis section. However, this characteristic can be noticed performing a DC Sweep after every step of the cycling stress. The resulting plot is shown in Figure 3.21. In this case 10 millions of cycles have been performed but at the end of the stress the device can not be considered still functioning.

However, it is possible to see that, up to 100K cycles, the actuation and deactuation voltages are almost constant. It means that charge trapping is not a problem but only the degradation of the contact is lowering the overall

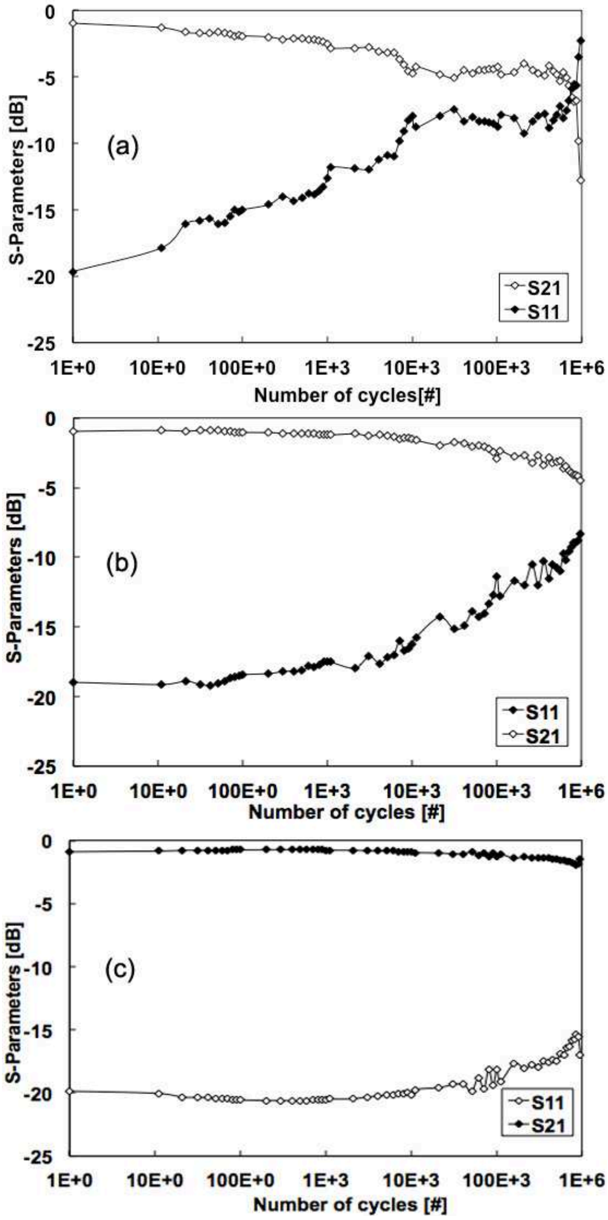

Figure 3.20: Cycling stress of PSX1 (a) PSX2 (b) and PSX5 (c) devices

performances.
After 1 million of cycles there is a small shift of the curve on the right as consequence of the presence of fixed charge trapped and a small degradation of the S parameter is noticeable. At the end of the stress, after 10 millions

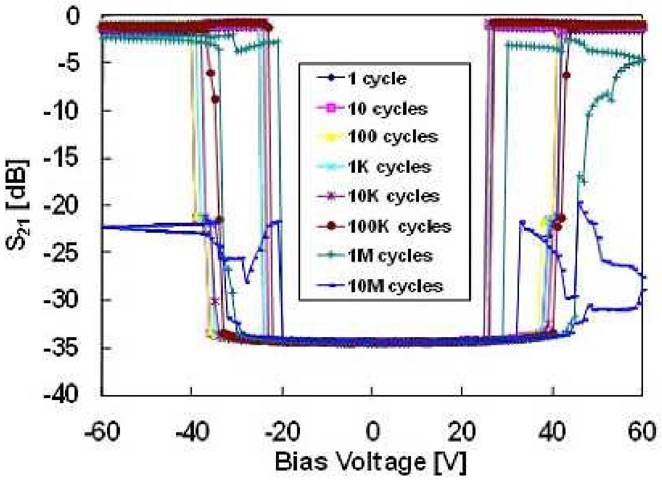

Figure 3.21: Consecutive DC characteristics performed during the cycling stress of a PSX5 device at 60V

cycles, the contact is completely degraded but the charge trapped is the same.

3.4.3 BO

Only one topology of boosted ohmic shunt switch (BO devices) has been subjected to cycling stress: the BO5.

Three different devices with the same layout and characteristics have been tested increasing the amplitude of the pulse of the stress. The first device has been tested at 40V, the second at 50V and the last one at 60V monitoring the S-parameters.

The results are shown in Figure 3.22 and they are similar to the one obtained for the meander and straight beams based switches designed by the University of Bologna.

The device tested at the lower voltage, only 40V, presents very poor performances with the degradation of the S-parameters that starts after only 200 cycles, making the device completely unusable at less than 10k cycles.

Increasing the stress voltage at 50V seems to improve the behavior of the switch that starts showing a degradation after 100k cycle becoming unusable after 1 million of cycles.

Finally, at the higher stress voltage, 60V, the switch exhibits good perfor-

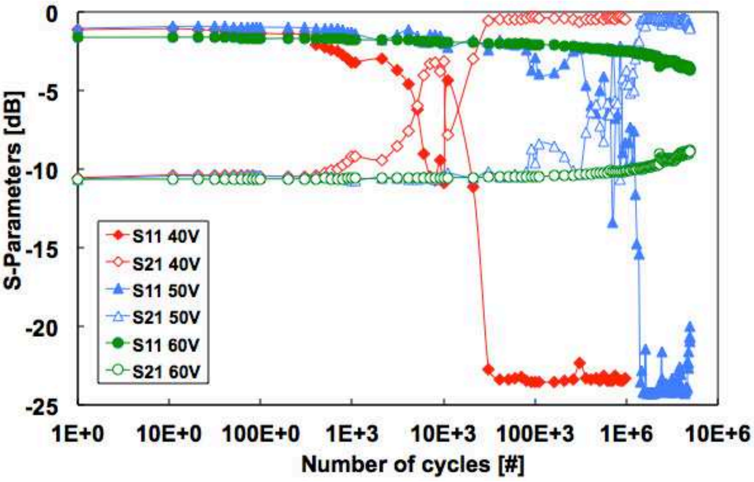

Figure 3.22: Parameter evolution during cycling stress of boosted ohmic shunt switches

mances being usable also after 5 millions of cycles.

It has been confirmed that stressing the switch at higher voltages can lead to an improvement of the reliability performances, at least from the cycling stress point of view.

In Figure 3.23 the DC characteristics of the BO device stressed at 50V have been reported.

There is a curve of the fresh device before cycling (pre cycling) and two curves made in series after the stress (1st post cycling and 2nd post cycling).

Two different phenomena can be recognized analyzing the different curves. The first one is the degradation of the contact that makes the S_{21} parameter decreasing from -12dB to -2dB at 40V, the second and more interesting is the partial recovery of the contact obtained doing a second DC Sweep.

Comparing the blue curve (first DC Sweep after the stress) and the green curve (second DC Sweep after the stress) it is clear how the contact has been improved by the first sweep. During the cycling the bias is applied only for $250\mu s$ and then immediately removed for $750\mu s$, on the contrary, during the DC Sweep the bias is constantly applied increasing the level at each step for a total time of $\sim 4s$ (the total DC Sweep least $\sim 16s$. Moreover the voltage applied arrives at 60V instead of 50V like during the cycling. The longer actuation time, together with the higher bias voltage, let the suspended

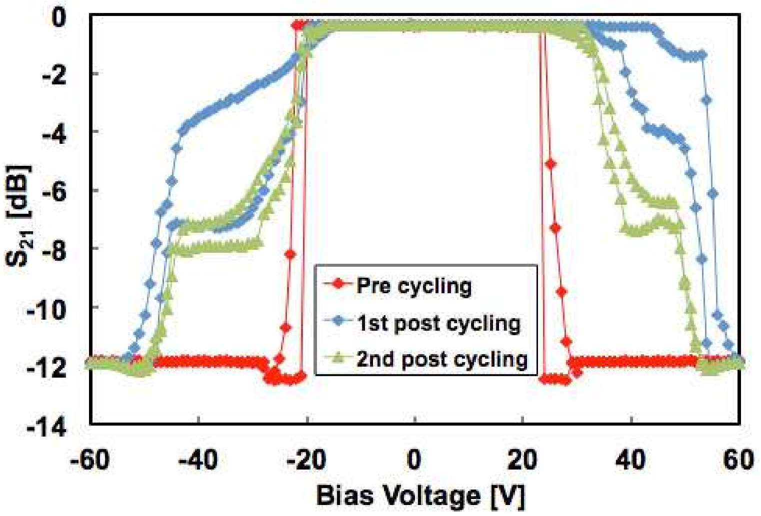

Figure 3.23: DC Sweep curve of a boosted ohmic shunt switches before and after cycling stress

membrane better settle on the contact point increasing its quality. A sort of smoothing seems to happen.

3.4.4 BAT

Several spring anchor ohmic switches (BAT) have been tested. However, most of them were not working because stuck in the down state position.
This problem could be caused by the too lower spring constant that lead to a very low actuation voltage and restoring force making possible for a small amount of residual stress to bend the suspended membrane.
Figure 3.24 shows the DC characteristics of a device that have been submitted to cycling stress.
The actuation voltage is extremely low and the actuation happens in two phases. The first phase happens at 12V and the S_{21} parameter goes from -31dB to -23dB, the second phase happens at 17V and the S_{21} parameter goes from -18dB to -0.7dB. The same phenomenon has been noticed also in the meander based devices designed by the University of Bologna. The common characteristic of these two different layouts is the low spring constant.
A small voltage is needed to bend down the suspended membrane and close the contact while an higher voltage is needed to reach the best performances.

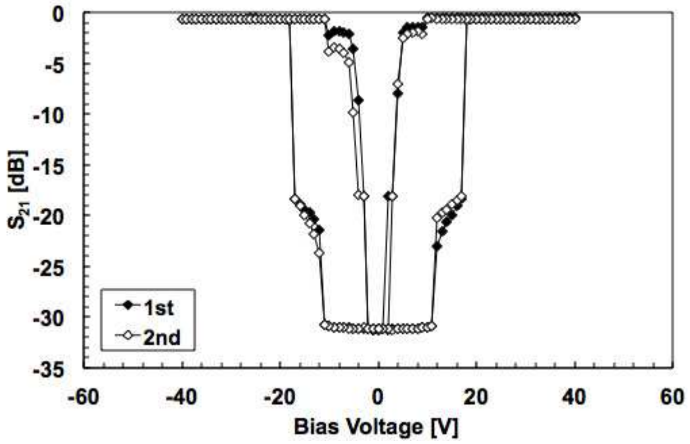

Figure 3.24: DC characteristics of a BAT device before cycling stress

Figure 3.25 shows the result of the cycling stress done at 30V.

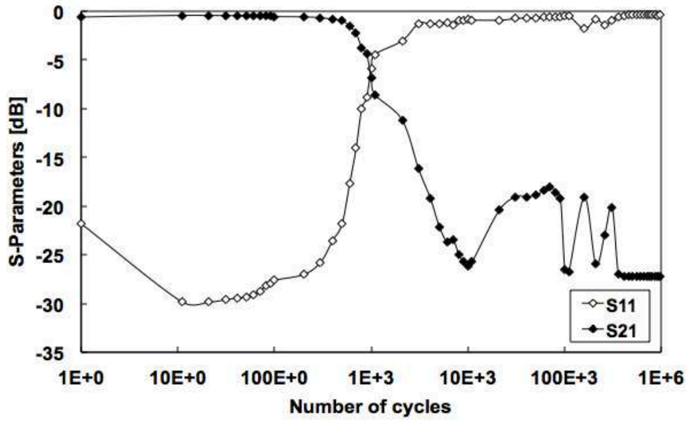

Figure 3.25: S-Parameters evolution during cycling stress of spring anchor ohmic (BAT) switch

Even if the DC characteristic is quite far from the ideal one, the cycling stress has been performed. However, the results obtained are not so good, the switch improves his RF performances between 1 and 10 cycles but then they start getting worse. At 1K cycles the device is completely unusable. Increasing the voltage stress do not improve the cycling performances but it leads to stiction.

3.4.5 CA

Several cantilever (CA) devices have been tested and almost all of them have shown excellent RF performances and reliability to cycling stress.
An example of DC characteristic is reported in Figure 3.26.

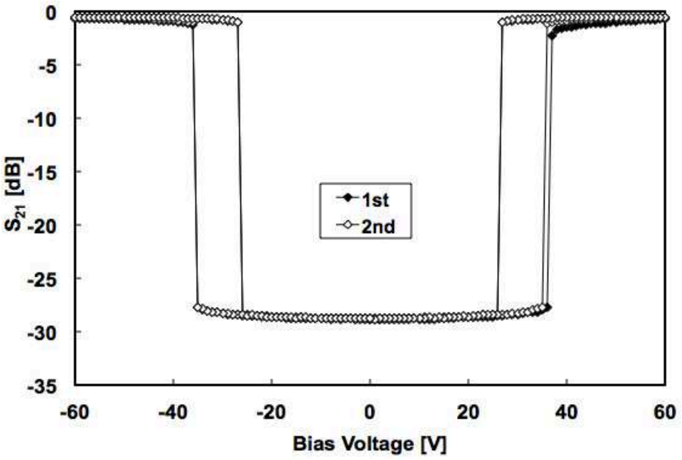

Figure 3.26: DC characteristic of a CA device before cycling stress

The actuation voltage is 35V, the de-actuation voltage is 25V and the curves are perfectly symmetric. Moreover, after the actuation the device reach immediately the best performances exhibiting a “clear” DC characteristic.
Figure 3.27 shows the S-Parameter evolution during the cycling stress performed at 60V.
The device do not present any degradation of the S-parameters up to 1 million of cycles, only after this point the S-parameters start getting worse. However, after 5 millions of cycles the “window” is not completely closed and there are almost 10dB of difference between the S-parameters.
Two DC sweeps have been performed after the stress and the results are reported in Figure 3.28.
From the first curve it is possible to see a partial degradation of the contact that makes the full actuation slower (for positive voltages) reaching the best performances only at 60V. Nevertheless, the contact recovery it is really fast and, during the first sweep, the actuation and deactuation for the negative region is immediate.
The second sweep presents no deviation neither in the positive or negative regions. The same phenomenon has already be seen for boosted ohmic shunt

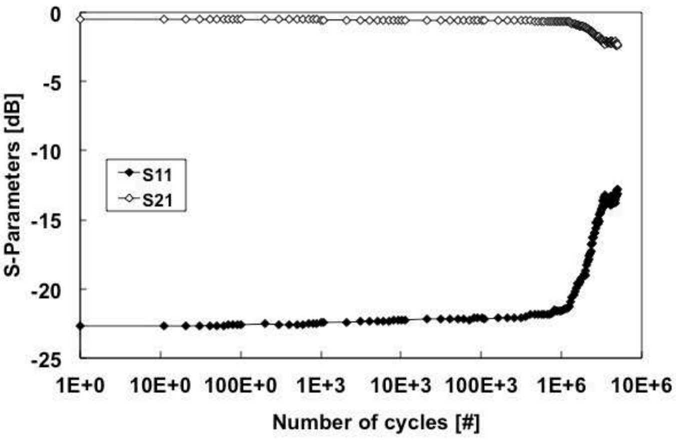

Figure 3.27: S-Parameters evolution during cycling stress of cantilever switch

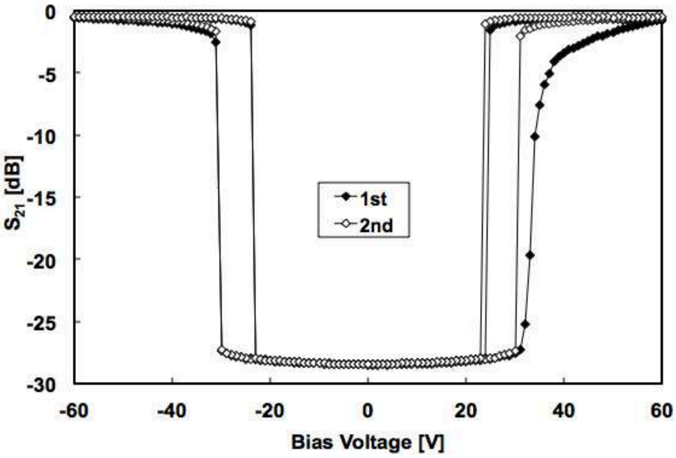

Figure 3.28: DC characteristic of a CA device after the cycling stress

switches.
After the stress the actuation voltage is 30V and the de-actuation voltage is 23V instead of 35V and 25V. This reduction of the actuation and de-actuation values is caused by the charge trapped during the stress.
Looking at Figure 3.29 the narrowing of the DC characteristic is clearly visible. In the graph the DC curve before the stress and the second DC curve after the stress have been reported. From this graph it can be noticed that there is almost no degradation of the contact but only a problem of charge

trapping.

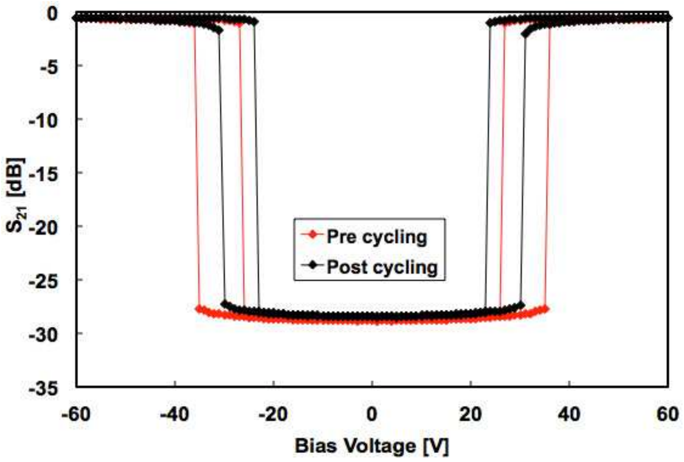

Figure 3.29: Comparison of DC characteristics before and after the cycling stress for a CA device

Capitolo 4

Long term actuation stress

The reliability of a RF-MEMS switch is generally connected to his ability to reach excellent performances during the cycling stress defined as the maximum number of cycles that can be done before the closure of the "window" and the stability of the S-parameters.
However, there are several applications in which the cycling robustness is not the greatest priority. If we think about using a RF-MEMS switch as a light and small redundancy switch in satellites, it is easy to understand that it does not matter if the device is able to perform 1 billion or 1 million of cycles but the ability to de-actuate after several years of working is more important. In some applications the switching time requirement could be around one second even after several years of work.
This is the reason why a new type of measurements have been set up: the long term actuation stress.

4.1 Long term actuation stress set-up

The behavior of different devices under continuous polarization has been tested monitoring the S-parameters during the actuation and release phase using an ad hoc set-up. The instruments used are the same that have been used for the DC Sweep as described in Figure 3.4.
The front panel of the Labview program used for this stress is reported in Figure 4.1. The S-parameters can be monitored in real time during all the stress and several parameters can be set to adjust the measurements for

every type of switch.
During the release phase, with $V_{BIAS} = 0$, the S-Parameters can be monitored every 1 second.

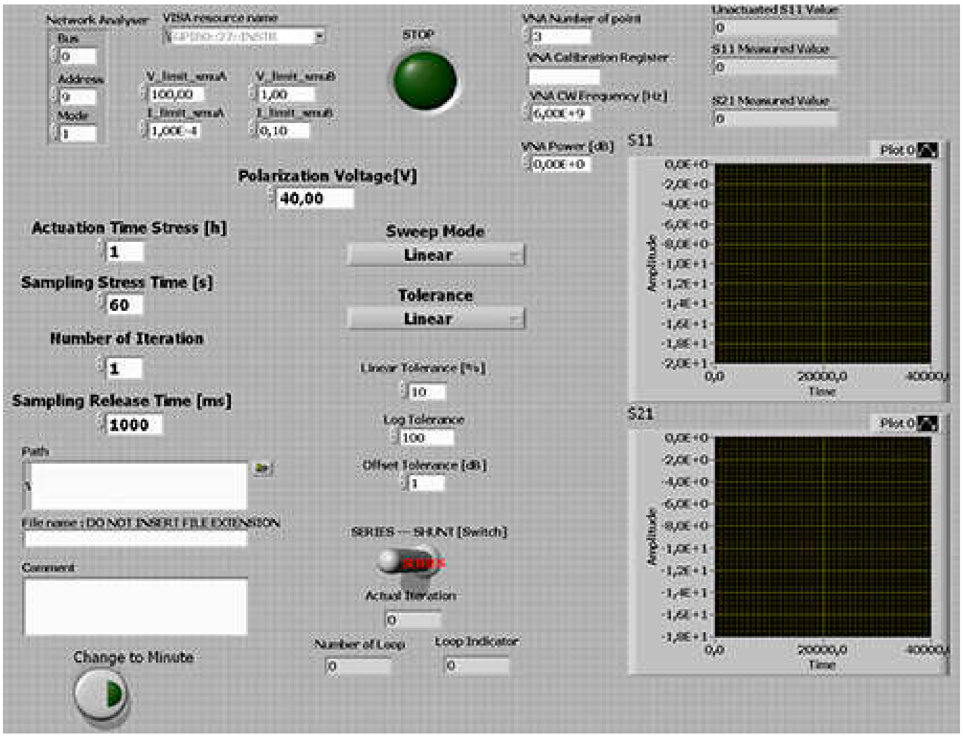

Bus: 0
Address: 9
Mode: 1
V_limit_smuA: 100,00
I_limit_smuA: 1,00E-4
V_limit_smuB: 1,00
I_limit_smuB: 0,10
Polarization Voltage[V]: 40,00
Actuation Time Stress [h]: 1
Sampling Stress Time [s]: 60
Number of Iteration: 1
Sampling Release Time [ms]: 1000
Sweep Mode: Linear
Tolerance: Linear
Linear Tolerance [%]: 10
Log Tolerance: 100
Offset Tolerance [dB]: 1
SERIES — SHUNT [Switch]: SERIES
Actual Iteration: 0
Number of Loop: 0
Loop Indicator: 0
VNA Number of point: 3
VNA Calibration Register:
VNA CW Frequency [Hz]: 6,00E+9
VNA Power [dB]: 0,00E+0
Unactuated S11 Value: 0
S11 Measured Value: 0
S21 Measured Value: 0

Figure 4.1: Front Panel of the Labview program used for the Long Term Actuation stress

4.2 Suspensions shape impact: meander based Vs straight beams devices

Several meander based and straight beams devices have been tested in order to better understand which is the influence of the suspended membrane shape in long term reliability stresses.
Figure 4.2 shows the S_{21} parameter evolution of a series meander based switch during a four hours stress at $V_{BIAS} = 40V$, $f_{RF} = 6GHz$, $P_{RF} = 0dBm$ and during the release phase.

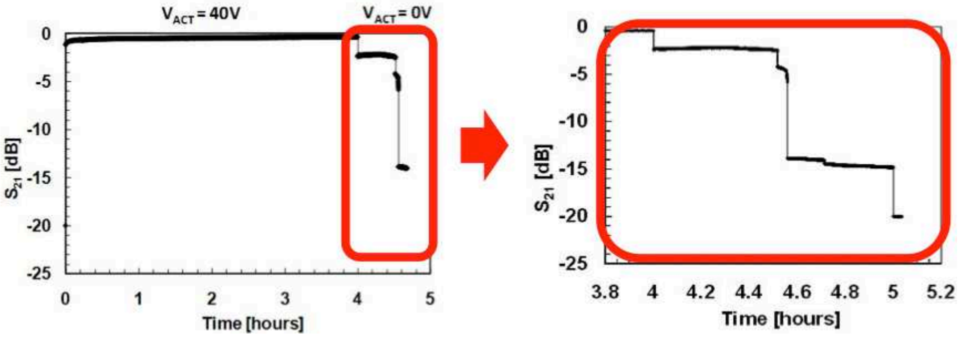

Figure 4.2: Meander based series switch. Full evolution of the S_{21} parameter during the stress (left) and magnification of the release phase (right)

During the first hour of actuation the insertion loss slightly decreases from 1.6dB up to 0.5dB probably because of the metal-to-metal contact improvement already described in the cycling stress section. However, this improvement in the contact could be the origin of the release delay problem: the switch takes around 1 hour to completely release itself since $V_{BIAS} = 0V$. Considering the release phase, the suspended membrane does not show a sudden release but a step-like evolution made of three different and well defined steps. This anomaly could indicate a progressive detachment of different sectors of the bridge from the bottom.

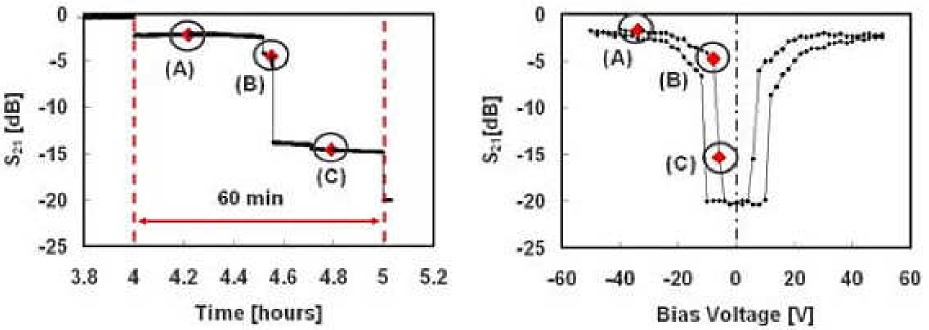

Figure 4.3: Comparison between release transient and DC characterization of an ohmic series meander based switch

Figure 4.3 shows the comparison between the release transient and the DC characteristic of the device tested. From the graphs it is possible to notice a

good correspondence between the long term stress release steps and the DC releasing behavior. This phenomenon can be explained by micro-welding and dielectric charging issues generated during the stress. A detailed description of the behavior of metal-to-metal contact and micro-welding is reported in [35]. Furthermore, meander based suspensions, characterized by a low restoring force, are not able to detach the stuck membrane and bring the bridge back in its rest position.
In order to better characterize the release time, the same stress with different actuation periods and applied RF power level has been performed.
Figure 4.4 (a) shows the release time as a function of the actuation time.

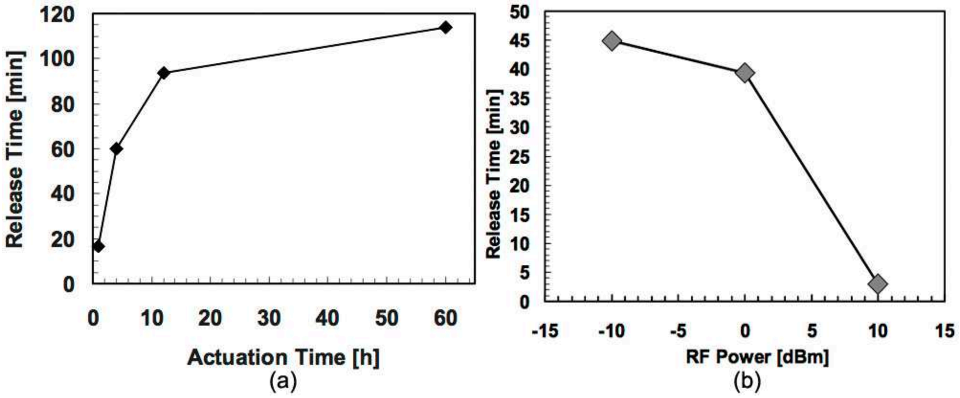

Figure 4.4: Release time evolution as a function of the time the device remained actuated (a) and as a function of the RF power applied (b)

It is clear that long actuation periods lead to long release times, reaching around 110 minutes after 60 hours of continuous polarization. Such behavior makes this type of devices, characterized by a low spring constant, not suitable for the development of a fast redundancy switch.
Figure 4.4 (b) shows the evolution of the release time of a meander based device stressed for 4 hours at different power levels of -10dBm, 0dBm, and 10dBm ($V_{BIAS} = 40V$). From the graph it is possible to see that increasing the RF power the release time gets lower.
This behavior can be explained with a local temperature increase of the device (just upon the SiO_2 dielectric layer between the actuation layer and the metal-to-metal contact), that can make charge recombination mechanisms faster, leading to a reduction of charge trapping phenomena. This change can also make the switch less sensitive to capillary effects, and micro-welding

problems.
Straight beams switches have been subjected to a long term actuation stress longer than the one used for the meander based devices reaching the 72 hours of continuous actuation with a RF power of 0dBm. Compared to meander based devices, the stronger spring constant of the straight beam based switches helps the suspended membrane to release itself as it is possible to see in Figure 4.5

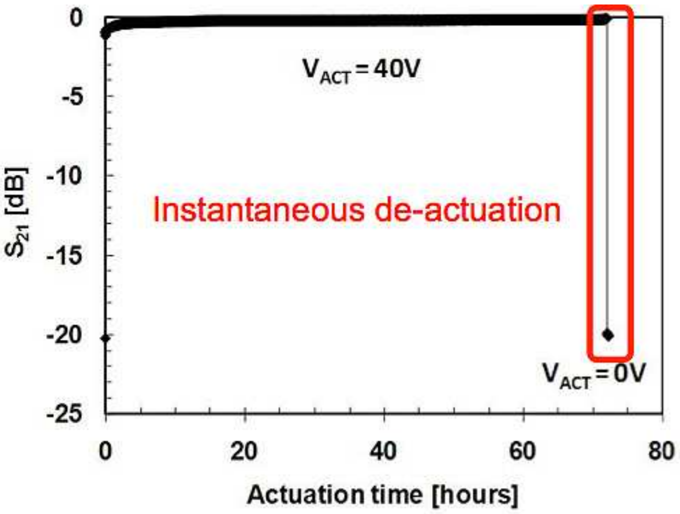

Figure 4.5: Straight beams based series switch. Full evolution of the S_{21} parameter during the stress

Moreover, it has been found that an high percent relative humidity can change the release time of the same device under the same stress condition, dramatically increasing from around 2 minutes to beyond 80 minutes. An excessive increase in local environment temperature can equally influence the reliability of these devices. Temperatures high enough to induce spring softening, will make the release time of RF-MEMS switches longer than at ambient temperature.

4.3 Analysis of different topologies of dielectric-less ohmic RF-MEMS cantilever-based switches

The evolution of the main electrical parameters for four different layouts of dielectric-less ohmic RF-MEMS cantilever-based switches during long term actuation stress has been investigated. In this case the measurement has been performed in a different way if compared with the previous section: the release phase has not been measured but a complete DC sweep has been performed after every step of the stress.

Figure 4.6 (a) shows the optical microscope image of the standard device SC1.

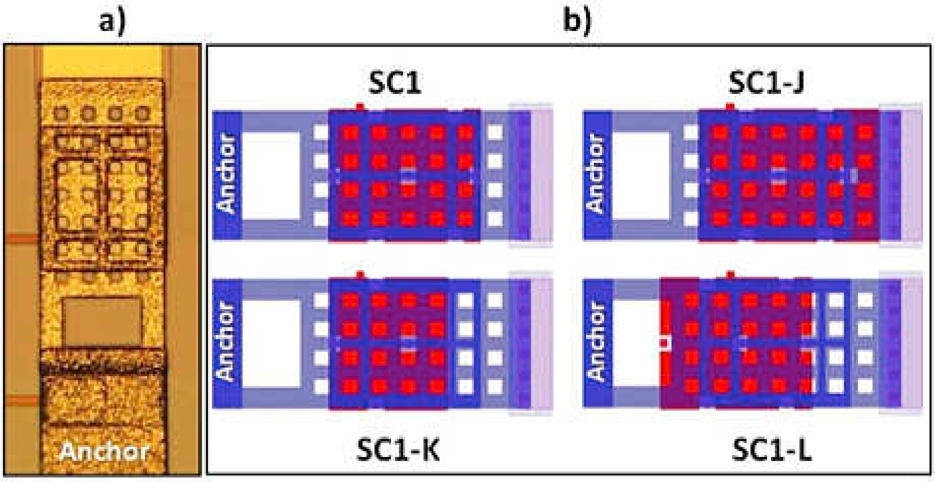

Figure 4.6: Optical microscope image of standard (SC1) switch (a), and studied layouts with different polysilicon size/substrate coverage (b, 90° left-rotated with respect to (a))

Tested devices consist of identical cantilever beams and differ in sizes and position of the actuator structures (see Figure 4.6 (b) red part), leaving different area of the substrate exposed to possible charge-trapping issues, as it will be discussed later. The device with the larger exposed area is SC1-K, whereas SC1-J is the one with the larger electrode.

In order to study the influence of continuous actuation on these switches, the devices have been submitted to a time-increasing fixed voltage stress. After each time step a full DC sweep has been performed, in order to investigate any deviation of the main electrical parameters (V_{ACT+}, V_{REL+},

V_{ACT-}, V_{REL-}, S-Parameters) from the initial ones. The result is shown in Figure 4.7.

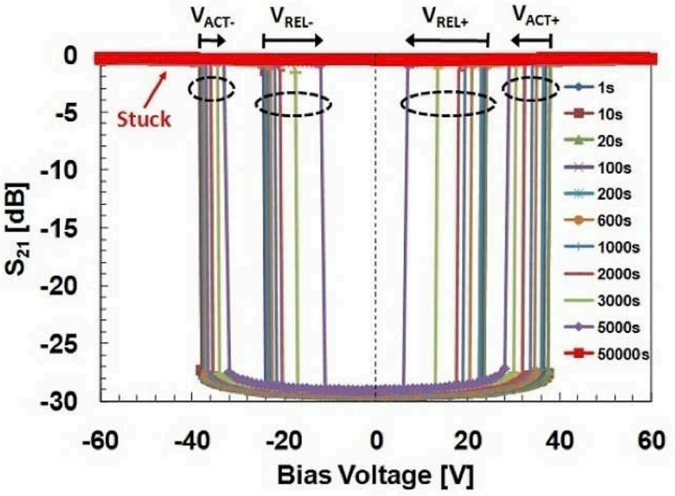

Figure 4.7: S_{21} curves evolution of a SC1-L switch measured after selected incremental times steps during continuous actuation stress at $V_{BIAS} = 50V$, $f_{RF} = 6GHz$, $P_{rf} = 0dBm$

Time steps duration were 1s, 10s, 20s,..., up to 50,000s, and the stress parameters were $V_{BIAS} = 50V$, $f_{RF} = 6GHz$, $P_{rf} = 0dBm$. Looking at Figure 4.7, three different phenomena can be distinguished: the narrowing of the hysteresis curves, a small left-shifting of the DC sweep center, and the stiction occurrence after the 50,000s long stress, that corresponds to a total time stress of 61,931 s, about 17.2 hours.

The narrowing and shifting of the curves confirm the results shown by [36] and [37], and, because of the greater variation of the V_{ACT+} and V_{REL+} than V_{ACT-} and V_{REL-} values, it is symptomatic of a negative charge trapping phenomenon. Because of the absence of dielectric layers over the polysilicon electrode, the charge could be entrapped in the oxide over the substrate near the actuation pad, as already proposed in [36].

The same measurements have been repeated applying a voltage stress of -50V and the same results have been obtained (positive charge in this case). Furthermore, to invert the DC sweep direction do not change the results, this leads to the conclusion that the DC sweep measurement and direction has only a negligible impact on the overall result.

The proposed stress procedure has been repeated also for devices SC1-J, SC1-K, and SC1-L, and the results were compared.
If we define the difference between the positive and negative actuation and release voltages at the time step t_i respectively as:

$$\Delta V_{ACT}(t_i) = \Delta V_{ACT+}(t_i) - \Delta V_{ACT-}(t_i) \tag{4.1}$$

$$\Delta V_{REL}(t_i) = \Delta V_{REL+}(t_i) - \Delta V_{REL-}(t_i) \tag{4.2}$$

the narrowing of the actuation and release voltage windows can then be defined as:

$$\Delta V_{ACT\_NAR}(t_i) = \Delta V_{ACT}(fresh) - \Delta V_{ACT}(t_i) \tag{4.3}$$

$$\Delta V_{REL\_NAR}(t_i) = \Delta V_{REL}(fresh) - \Delta V_{REL}(t_i) \tag{4.4}$$

and the shifts of the center of symmetry of $\Delta V_{ACT}(t_i)$ and $\Delta V_{REL}(t_i)$ respectively as:

$$\Delta V_{ACT\_SHIFT}(t_i) = \frac{\Delta V_{ACT+}(0) + \Delta V_{ACT-}(0)}{2} - \frac{\Delta V_{ACT+}(t_i) + \Delta V_{ACT-}(t_i)}{2} \tag{4.5}$$

$$\Delta V_{REL\_SHIFT}(t_i) = \frac{\Delta V_{REL+}(0) + \Delta V_{REL-}(0)}{2} - \frac{\Delta V_{REL+}(t_i) + \Delta V_{REL-}(t_i)}{2} \tag{4.6}$$

The results obtained using the previous (from 4.1 to 4.6) equations have been plot in Figure 4.8.
The first result is that both narrowing and shifting of the S_{21} curves are induced by the continuous actuation stress. These phenomena are driven by dielectric charge trapping issues, as already discussed previously for device SC1.
The other important consideration is that the slope of the $V_{REL}(t_i)$ can be considered as a factor to evaluate the robustness of RF-MEMS versus continuous actuation stresses: the faster the slope is, the easier and faster could be the chance to fall into stiction issues. Comparing the results obtained with the three different structures, it is possible to see from Figure 4.8 that devices SC1-K are the most sensitive concerning this kind of reliability problem. Such devices, in fact, showed a fast increase of the slope of both $V_{ACT\_NAR}(t_i)$ and $V_{REL\_NAR}(t_i)$ curves after just 1000s. The different

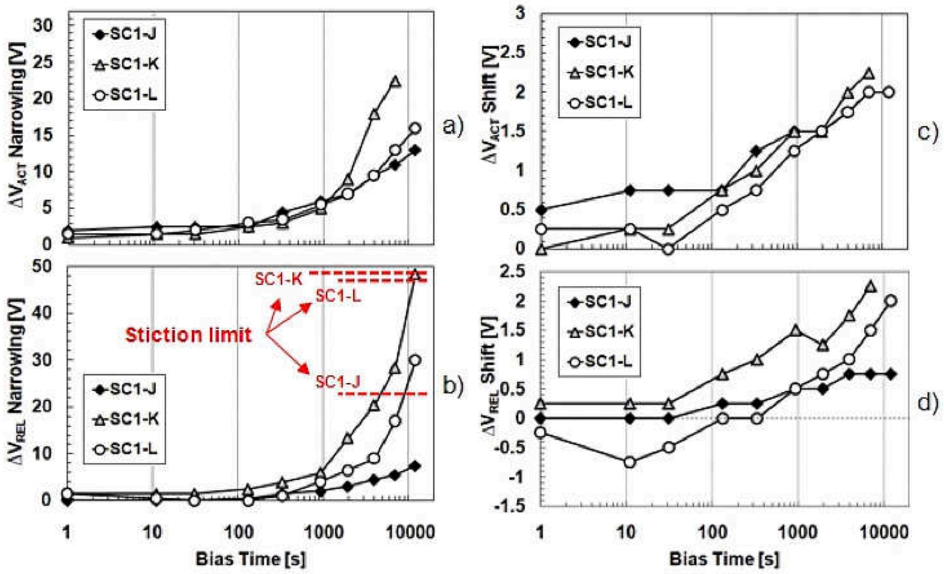

Figure 4.8: Narrowing and shifting of the center of symmetry of V_{ACT} (a, c) and V_{REL} (b, d) during the continuous actuation stress on devices SC1-J, SC1-K, SC1-L. The three different stiction limits have been highlighted in (b)

behavior of the three typologies can be easily correlated to the difference of the sizes and positions of the polysilicon actuator structures. In fact, the device with the largest area of uncovered substrate (SC1-K), was also the most sensitive, as previously described. On the contrary, the typology SC1-J presents the largest actuator structure, and it turned out to be the most robust. These results lead to the fact that the oxide around the actuator structure could easily entrap charges as already demonstrated in literature, but this phenomenon can be reduced with an ad-hoc design of the actuator structure.

The sensitivity of a SC1 switch to stiction issue at increasing stress voltage have been investigated studying the evolution of the normalized release voltage at V_{BIAS} = 30V, 40V, and 60V.

Measured curves, shown in Figure 4.9, have been fitted using the power law equation proposed by Curie-Von Schweidler [38]:

$$V_{REL+NORMALIZED} = a\Delta(t_{stress})^b + 1 \tag{4.7}$$

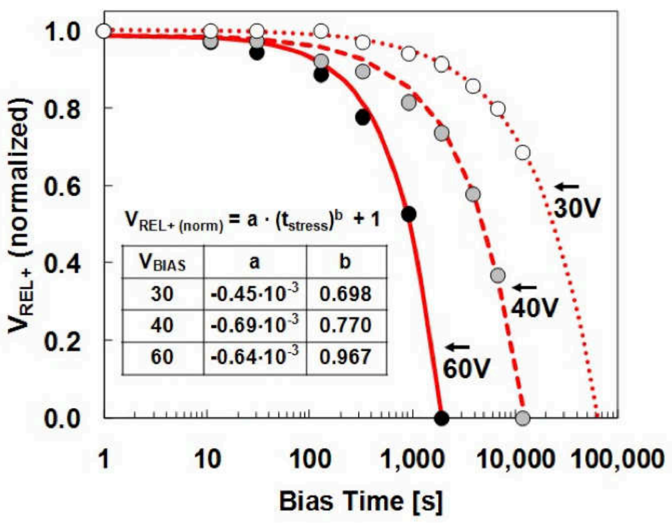

Figure 4.9: Evolution of the normalized release voltage of a SC1 device. Broken lines represent the fit curves

Obtained data and fitting curves are well in accordance with the results shown in [37]. Furthermore, $V_{REL+_{NORMALIZED}} = 0\%$ represents the stiction occurrence of the device.

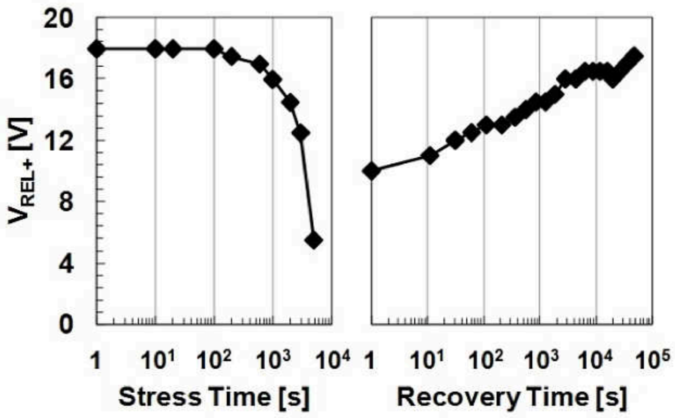

Figure 4.10: V_{REL+} evolution of device SC1 during continuous actuation stress performed at 50 V, and during the successive recovery phase at 0 V

In order to better understand the charging and discharging phenomena, recovery investigation of previously stressed structures have been performed. The measurement setup was identical to the one used to stress the devices, but in this case the S_{21} curves were monitored after selected steps with 0V applied during the delay steps. An example of the adopted procedure is shown in Figure 4.10 for a SC1 device, concerning the evolution of V_{REL+} during a 5000s long stress at 50V, and during the successive recovery last about 80000s. All the other electrical parameters exhibited a similar behavior. It is interesting to note the exponential shape of the charging phase, compared to the linear evolution shown during the discharging phase (in log scale).

The continuous actuation stress experiment on devices already stressed after a full recovery of the main electrical parameters have been repeated. Figure 4.11 shows the evolution of the $V_{ACT\_NAR}(t_i)$ parameter as a function of the stress time of a SC1-L switch during a continuous actuation at 50V.

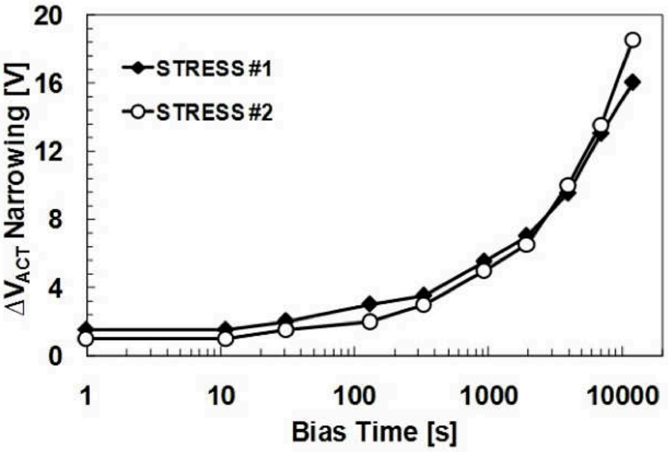

Figure 4.11: Comparison of the evolution of V_{ACT_NAR} as a function of the stress time (stress voltage = 50V) of a SC1-L fresh device (stress 1), and of the same device stressed in the same condition after a complete recovery

The two curves are almost overlapped. This means that the de-trapping phase was nearly total. At the same time, analyzing the evolution of S-Parameters values, the metal-to-metal contact was not impaired by previous operation.

In order to investigate the robustness of studied dielectric-less switches to breakdown occurrence, a stair-like voltage to the actuation pad has been applied, monitoring the drained current (I_{BIAS}), and acquiring the emission

image by means of an Hamamatsu PHEMOS-200 emission microscope.
Unfortunately, very few hot spots were visible, highlighted by the arrows in Figure 4.12 (a) (SC1-L), because of the coverage of the gold membrane. The device showed an increase of I_{BIAS} from $V_{BIAS} > 70V$. This behavior could be due to the approaching of the breakdown point of some dielectric layer, or to the downward movement of the cantilever towards the polysilicon actuator above the contact area. The breakdown point occurred at about 120V, and the second hypothesis was confirmed by the inspection of the polysilicon actuation structure, after the cantilever removal. A large burnt occurred, as shown in Figure 4.12 (b), due to the high dissipated power, with the corresponding stain visible also to the back of the cantilever, see Figure 4.12 (c).

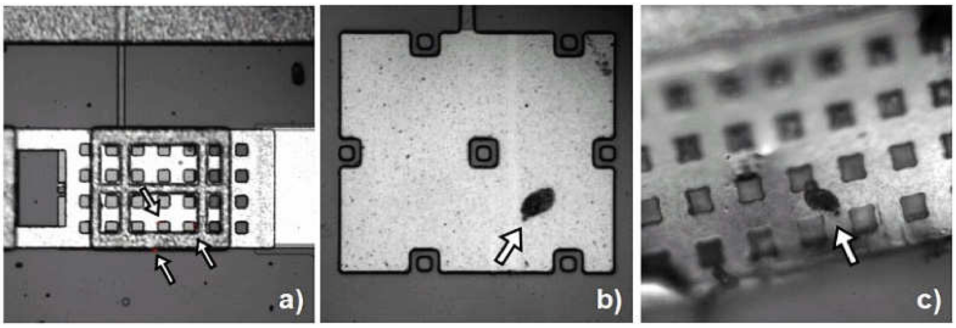

Figure 4.12: Emission microscope image of the SC1-L switch during breakdown tests (a). Optical images of the actuator (b) and of the back of the cantilever (c) after the breakdown occurrence

The repetition of the breakdown test after cantilever removal showed an increase of I_{BIAS} only for $V_{BIAS} > 170V$, leading to the conclusion that such potential reliability issue is localized only on the MEMS structure, and not on the other parts of layout.

4.4 PSX devices analysis

The robustness of series ohmic winged switch with stopping pillars (PSX) device stressed with long term actuation has been tested.
These devices have exhibited excellent performances as reported in Figure 4.13.

After twelve hours of continuous actuation at 70V the release phase seems to be immediate, it needs less than 1s.

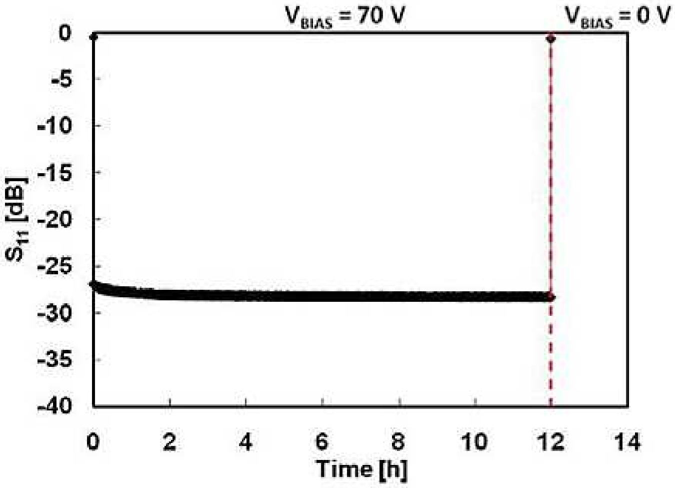

Figure 4.13: Full evolution of the S_{21} parameter during the stress

In order to better understand if there is a relation between the release time and the stress time even if the device seems to deactuate immediately, e new measurement set up has been realized and it is shown in Figure 4.14.

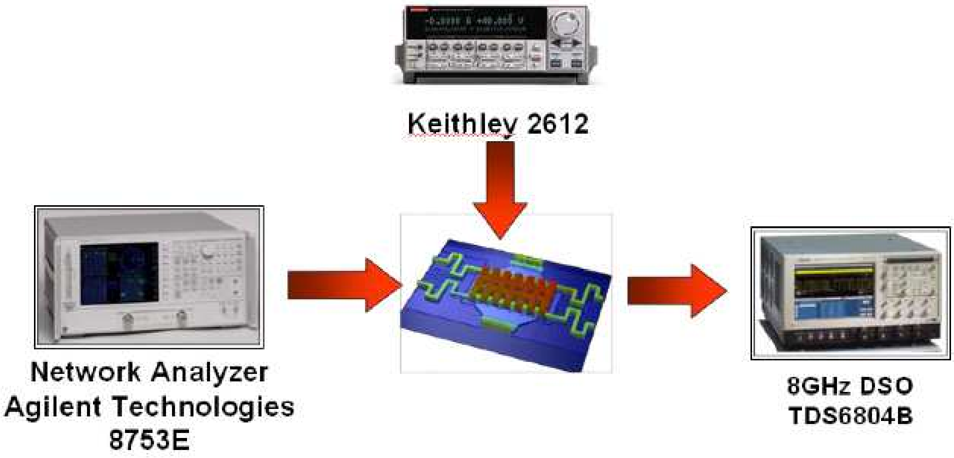

Figure 4.14: New set-up for monitoring fast release phase

The scheme is quite similar to the one used for the normal Long Term Actuation stress but, in this case, the output signal does not go back to the

Network Analyzer but in the Digital Storage Oscilloscope. The curve that is possible to see thanks to the oscilloscope is reported in Figure 4.15

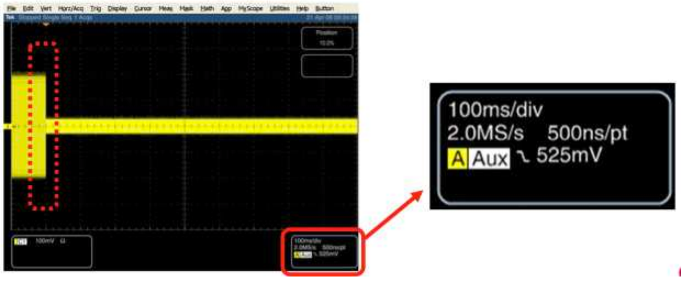

100ms/div
2.0MS/s 500ns/pt
A Aux ⤵ 525mV

Figure 4.15: Example of measurement done during the release phase with the Digital Storage Oscilloscope

With this new set-up a resolution of 500ns is possible, instead of 1s using the other set-up. This system makes possible to perform a deeper analysis of the releasing phase even for devices that seem to deactuate immediately. Long Term Actuation stress has been repeated on PSX devices increasing the stress time at every step and monitoring the release time. The plot of the release time as a function of actuation time is reported in Figure 4.16.

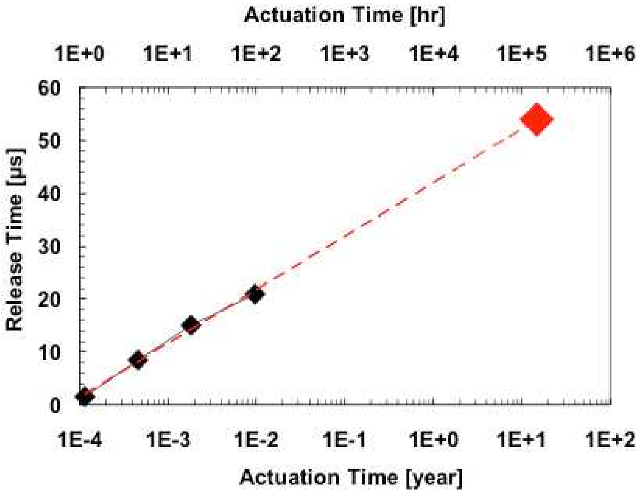

Figure 4.16: Release time as a function of actuation time for PSX device. The red line is a linear interpolation of the measured data.

After 1 hour of stress at 70V the release time is $\sim 2\mu s$, after 4 hours it

increase at $\sim 8\mu s$ becoming $\sim 15\mu s$ after 12 hours of stress. Finally, after 100 hours of stress the release time is only $\sim 20\mu s$.
The red line is a linear interpolation of the measured data and, in according to this trend, the device should take only less than $60\mu s$ to deactuate after 15 years of actuation.
Considering all the Long Term Actuation stresses performed on different devices designed by the University of Bologna or by the University of Perugia, PSX devices result to be the best candidate for applications in which a long term reliability is required.

Capitolo 5

Analysis of EOS/ESD events

In the last years reconfigurable network systems become more popular and their market size is growing fast. One of the best candidate for these kind of applications are RF-MEMS devices thanks to their good performances at high frequency and extreme low power consumption. Examples of applications for RF-MEMS can be actually found as tx/rx antenna switch in mobile phone, or in many spatial applications, thanks to the size and weight reduction in comparison to traditional mechanical coaxial switches.

If we consider nano-satellites, satellites that weight less than 10kg and that can be considered the future of space communications and Earth monitoring, RF-MEMS devices are the best solution. The possible combination of MEMS inertial sensors for space-position tracing, and high frequency MEMS switches for multi-standard RF net developing, is expected to save weight and volume issues in space applications (actually a mechanical reconfigurable switch net can weight several kilograms) opening the road to the next generation of satellites.

Unfortunately, there are still open questions concerning the reliability of RF-MEMS devices that can prevent their presence in this market. Some of the problems are the presence of continuous thermal cycling, shocks and vibrations (during take-off and solar panels opening), and last, but not least, Electro Static Discharge (ESD) and radiation phenomena.

However, one of the most critical issues are the EOS/ESD phenomena that are quite common on satellites due to the high intensity of electromagnetic fields that envelop the Earth.

As reported in literature [32], ESD is the main cause of electrical equipment

failure in space missions. RF-MEMS switches have a greater probability to be affected by EOS/ESD events than sensors and actuators that are typically packaged without any direct connection to pins exposed to the external world. On the contrary, RF-MEMS switches could, for example, be exposed to phenomena coming from the antenna connection.
With all these considerations, to investigate EOS/ESD phenomena in RF-MEMS devices is extremely important.

5.1 Time Domain Reflectometer Transmission Line Pulser (TDR-TLP) set-up

The best way to produce extremely fast squared pulses with different length and amplitude, characterized by a steep slope, consists in charge and discharge the distributed capacitance of a transmission line. This gave the name to this method: Transmission Line Pulser (TLP).
A simplified scheme of the set-up used for the following measurements (TDR-TLP) is presented in Figure 5.1.

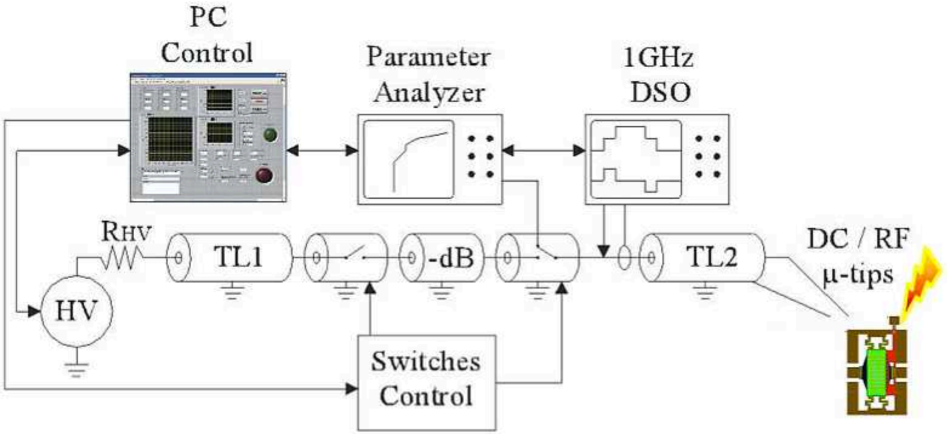

Figure 5.1: Simplify scheme of the Time Domain Reflectometer TLP

An high voltage source (HV) is used to charge the distributed capacitance of the first transmission line (TL1) through an high-ohmic resistor (R_{HV}) while the coaxial switch remains open. Closing the switch, the discharge of TL1 creates a squared pulse whose length is equal to the length of the

charged line divided by the propagation speed of the signal from the switch to the high-ohmic end of this line and back to the switch.
For instance, 10m of RG58 transmission line with a propagation speed of 20cm/ns generate a 100ns wide pulse.
Concerning the amplitude of the pulse, in general it depends by the pre-charged voltage, V_{HV}, by the impedance of the source Z_S and by the impedance of the load Z_L following the equation

$$V = V_0 \cdot \frac{Z_L}{Z_L + Z_S} \tag{5.1}$$

In the case of matched impedance $V = V_0/2$.
An attenuator (-dB) between the generator and the device under test (DUT) is needed in order to avoid multiple stresses caused by multiple reflections.
Finally, the TL2 transmission line separates the incident and reflected pulse adding a delay at the reflected pulse.
Considering that the Time Domain Reflectometer TLP is based on the fact that if an incident pulse reaches the DUT at the end of the transmission line it will be reflected depending on the impedance $Z_{DUT}(t)$ and on the impedance of the transmission line Z_0, the amplitude of the reflected pulse is:

$$V_{reflected}(t) = \frac{Z_{DUT}(t - t_{delay}) - Z_0}{Z_{DUT}(t - t_{delay}) + Z_0} \cdot V_{incident}(t - t_{delay}) \tag{5.2}$$

The voltage $V_{DUT}(t)$ and the current $I_{DUT}(t)$ are measured starting from the measured pulses and shifting the reflected signal of $2t_{delay}$ obtaining the following equations:

$$V_{DUT}(t) = V_{incident}(t) + V_{reflected}(t - 2 \cdot t_{delay}) \tag{5.3}$$

$$I_{DUT}(t) = \frac{V_{incident}(t) - V_{reflected}(t - 2 \cdot t_{delay})}{Z_0} \tag{5.4}$$

An example of measures obtained is shown in Figure 5.2
All the set-up is controlled with an ad-hoc labview program and the front

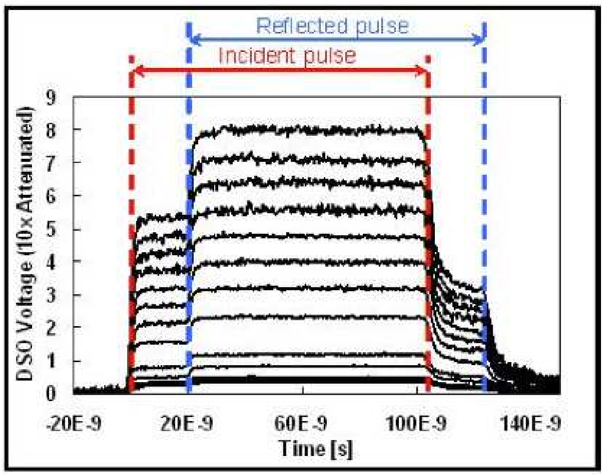

Figure 5.2: Example of curves obtained with the DSO during TDR-TLP stress

panel is shown in Figure 5.3

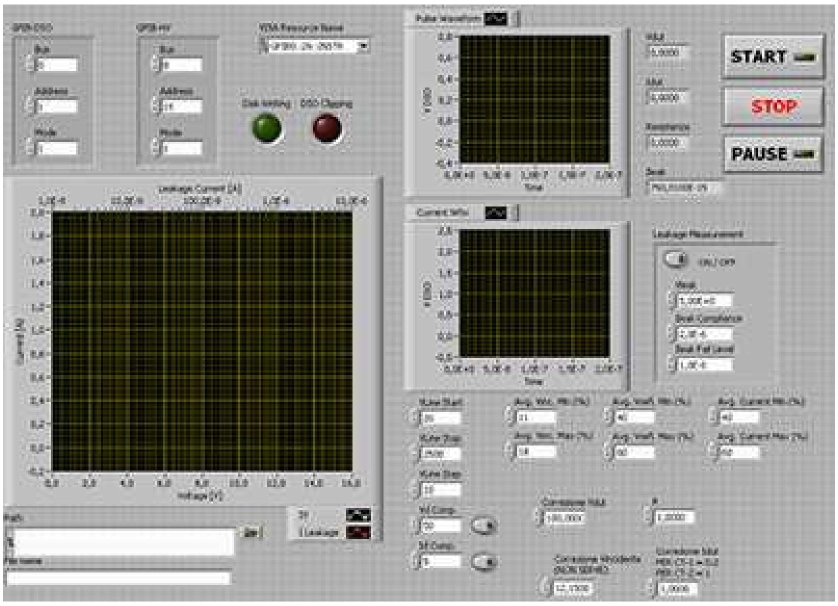

Figure 5.3: Front panel of the Labview program used for the TDR-TLP

Several parameters can be set with the program, for instance the start, step, and stop voltage pulse, the parasitic resistance and other important values. This makes the set-up extremely flexible and different type of devices can be measured.

5.2 ESD Sensitivity of Functional RF-MEMS Switches

Several typologies of ohmic RF-switches, in both shunt (normally closed) and series (normally opened) configuration have been tested. These devices have been designed by the University of Bologna and the scheme is presented in Figure 5.4

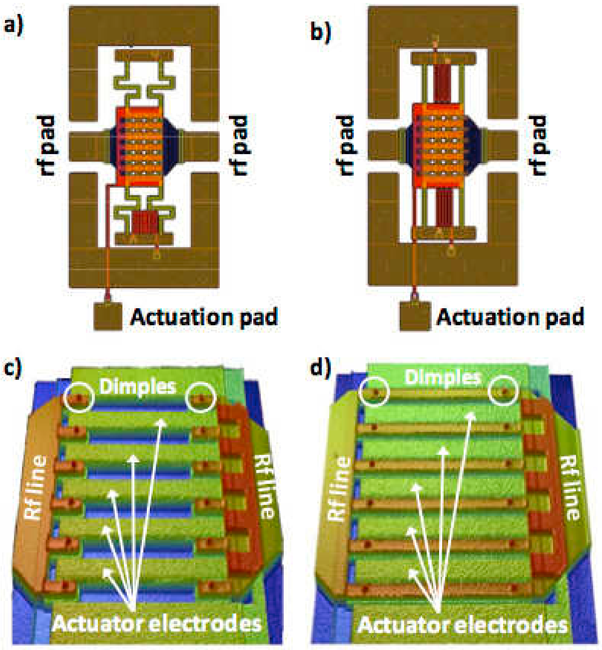

Figure 5.4: Tested devices layouts: meander based suspensions (a), and straight beam suspensions (b). Optical profilometer image of a series switch (c) and shunt one (d) after suspended membrane removal. Actuator electrodes and dimples are highlighted in the picture.

5.2.1 TLP characterization

The sensitivity to EOS/ESD has been studied, using the 100ns TDR-TLP system described in the previous section, in the following conditions: (I) between RF-OUT and ground with no bias voltage applied (up-state membrane), and (II) between RF-OUT and GND at different actuation voltage (fully actuated / partially bended membrane). These two configurations are potentially the most critical for the reliability of RF-MEMS switches. Considering the first condition, Figure 5.5 shows the typical IV-TLP graph exhibited by straight beams shunt RF-switches tested in not actuated condition.

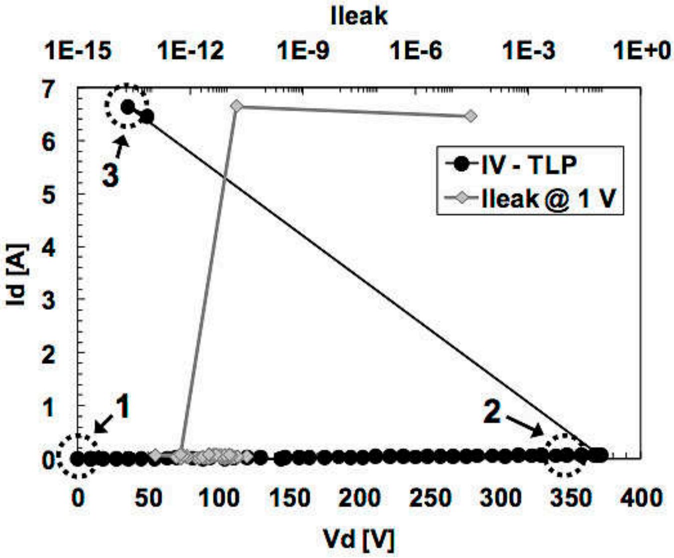

Figure 5.5: IV-TLP (black curve) of meander based shunt RF- switch tested between RF-OUT and ground. The gray curve shows the evolution of the leakage current during the TLP stress

The equivalent circuit of the tested device in this topology is an open circuit, constituted by the suspended membrane, the air-gap ($3\mu m$), and the transmission line. As it is possible to see in Figure 5.5 the device exhibits an open-circuit behavior up to around 380V. At 380V, the system abruptly switches to a short-circuit behavior due to dielectric breakdown. Dielectric breakdown is also accompanied by visible sparks under the membrane. As already demonstrated in [39], the traditional TLP leakage measurement (measured at 1V) does not offer any certain indication of the device life state, but it creates a failure, which is only apparent when the device is completely destroyed. The highlight of the evolution of the leakage current during this test is reported in Figure 5.6

Fluctuations in the leakage current at a level of pico-amperes are the result of simple electrical noise. On the contrary, the analysis of voltage and cur-

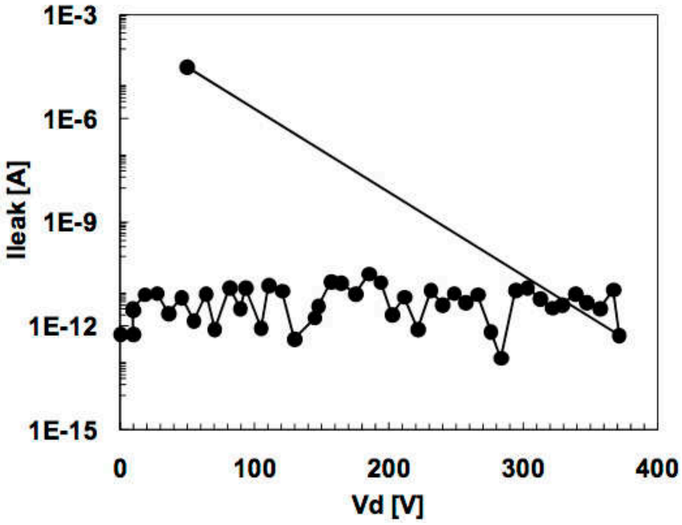

Figure 5.6: Highlight of the evolution of the leakage current during the TLP stress of meander based shunt RF-switch tested between RF-OUT and ground

rent waveforms performed after each TLP pulse, and especially the complete characterization of the scattering parameters during the TLP stress, show that the failure has occurred at about 350V as presented in Figure 5.7.

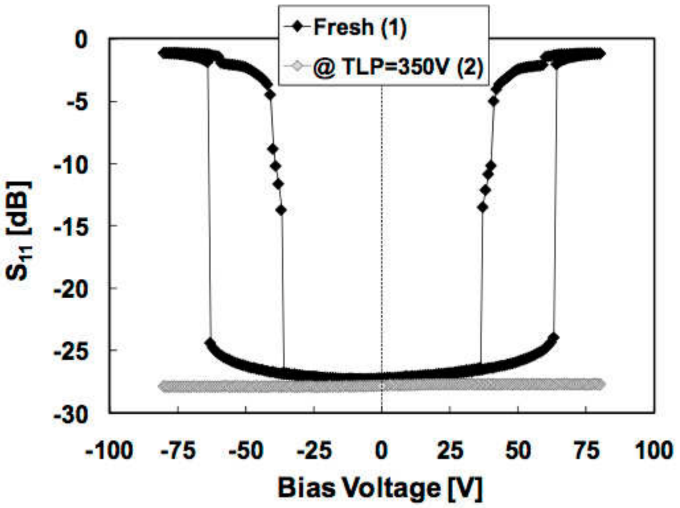

Figure 5.7: S_{11} behavior of the shunt RF-switch stressed between RF-OUT and ground before (1), and after the TLP failure point (2)

No variations of the S-Parameters have been measured before the failure point. A possible reason for the MEMS blocking can be debris formation. At this point the membrane is no more able to bend (grayed diamond curve) because of debris formation caused by melting during the spark.
Figure 5.8 shows images of the top view of the damaged device, and, after the suspended membrane removal, it is possible to see the large burns caused by the dielectric breakdown.

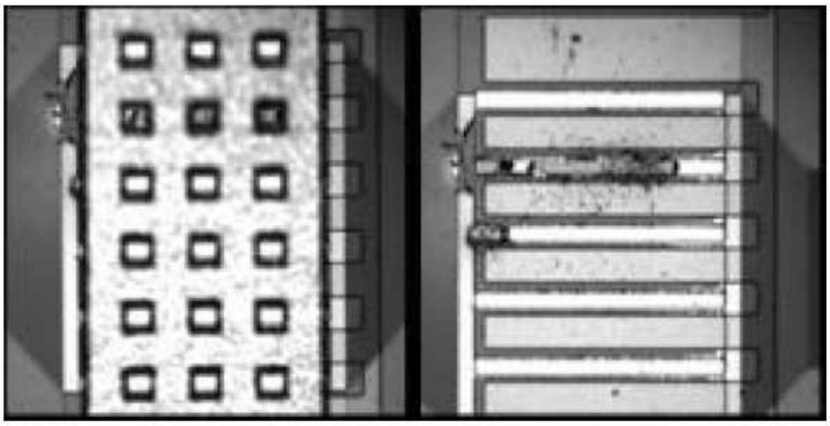

Figure 5.8: Pictures of the meander based shunt RF-switch of Figures 2 and 3 after the dielectric breakdown occurred (sx), and after membrane removal (dx)

Dielectric breakdown occurs between 370V and 400V, in good accordance with the breakdown voltage values for a $3\mu m$ air gap predicted by the modified Paschen's law that predicts about 350V [40], and that type of stress can lead to both open or short circuit formation.
Considering the second type of stress, between RF-OUT and GND at different actuation voltage, the IV-TLP characterization of straight beams shunt RF-switches with ESD-like events applied between RF-OUT and ground when the device is actuated ($V_{ACT} = 60V$) is shown in Figure 5.9
An actuated shunt device exhibits a low impedance path between the RF pads and ground, as demonstrated by the IV-TLP curve (series resistance of around 2Ω), up to the complete destruction of the RF-MEMS that occurs at extremely high TLP injected current (18A).
Like in the first test type, S-Parameters analysis shows that the failure occurs at lower current values. In fact, as it is possible to see in Figure 5.10, the

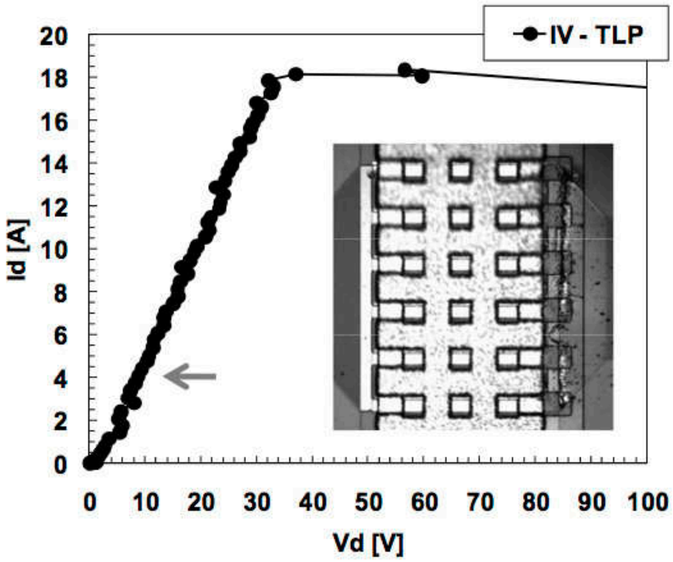

Figure 5.9: IV-TLP of straight beams shunt RF-switch tested between RF-OUT and ground actuated at $V_{ACT} = 60V$. The inset shows the damages caused by the high current flown during the TLP stress. S_{21} parameter characterization shown in Figure 5.10 was extracted after the TLP point indicated by the arrow

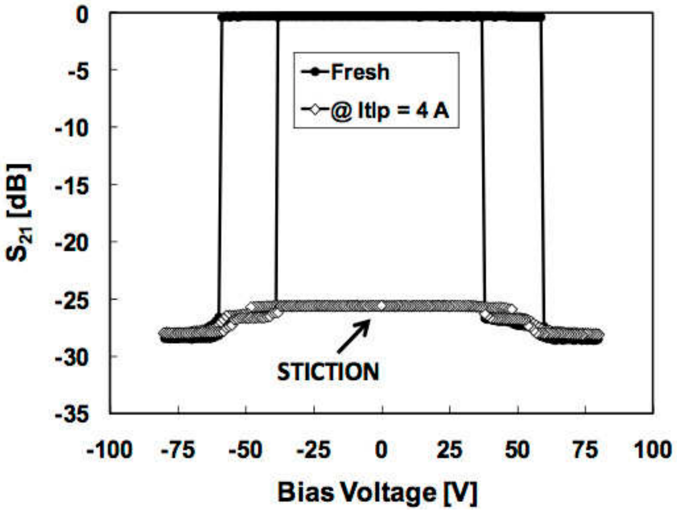

Figure 5.10: S_{21} behavior of the straight beams shunt RF-switch stressed between RF-OUT and ground @ $V_{ACT} = 60V$ during the TLP stress of Figure 5.10 (TLP points indicated by the arrows)

device is severally damaged after only 4A of TLP current. No S-Parameters variations have been shown before this TLP current level.

To better investigate the robustness to ESD events in this configuration, the same stress at different actuation voltages have been repeated, it has been observed that the greater is the actuation voltage, the greater is the TLP robustness. This is most probably due to the increase of the surface contact between the bended membrane and dimples/transmission line, leading to the creation of a better low-impedance path for the ESD event.

Furthermore, it has been discovered that the TLP failure level is dependent on the suspensions shape (spring constant). In fact, the same test applied to meander based RF-switches has lead to stiction problems at a TLP current level of below 0.75A. This happens because meander based suspensions, characterized by a lower spring constant, are less efficient to restore the membrane state if metal-to-metal micro-welding occurs during the TLP stress.

Considering the characterization of series type RF-switches, the TLP events between RF-OUT and GND, in non-actuated condition, and at different actuation voltages have been applied. In this configuration, the voltage at the RF-IN pad has been monitored and it has been found that, in this case, about 400V are enough to cause the breakdown of the device.

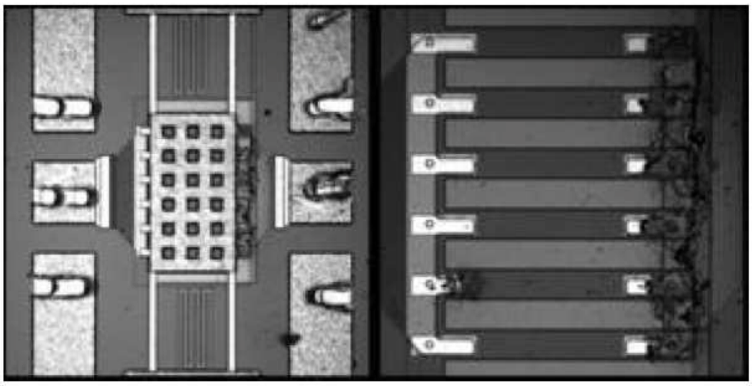

Figure 5.11: Pictures of the straight beam series RF-switch after the failure occurred (sx), and after membrane removal (dx)

Figure 5.11 shows pictures of the top view of the damaged device. After removal of the suspended membrane, it is possible to see the burns of the RF-switch fingers. The burns were caused by dielectric breakdown followed

by high current flows. Furthermore, some coupling of the TLP pulse from the RF-OUT pad to the RF-IN pad was observed.
This test have been repeated while applying an actuation voltage which is not sufficient to actuate the device, but only to slightly bend the membrane downward. This test simulates residual stress, or partial actuations caused by entrapped charge. As expected, the TLP failure voltage decrease with the increase of the actuation voltage (or the increase of residual bending).

5.2.2 HBM characterization

RF-MEMS switches have also been characterized under HBM regime, in order to study if any correlation between TLP tests and the Human Body Model exists for these devices. Preliminary results on the testing of the EOS/ESD sensitivity between the actuation pad and ground are here presented. Previous data [41] have shown that in this configuration TLP pulses of about 300 V are sufficient to destroy the device. HBM-like stresses on wafer level between actuation pad and ground have been applied to all the previously described topologies of RF-MEMS switches, starting at 50 V, with an increasing step of 50 V. We have obtained failure voltage levels between 300 and 350 V, in good agreement with previously made TLP stresses. Like TLP tests, HBM stresses have brought to a complete destruction of the actuator polysilicon line, leading to a no more working device.
In order to better investigate where the dielectric breakdown occurs, the stress using ad-hoc designed test structures have been repeated. These are characterized by different distances (L) between the actuation pad and ground ($10\mu m$, $20\mu m$, $30\mu m$, $50\mu m$, $100\mu m$), and two width (W) of the polysilicon lines ($5\mu m$, $10\mu m$). The goal was to understand if the breakdown occurs only at the crossing between the polysilicon line and the ground layer (separated by 100nm of TEOS and 200nm of LTO), or if breakdown could be induced in air along the surface.
Using the on wafer HBM-like tester, the results presented in Figure 5.12 have been obtained. During the tests we have used the measurement of the leakage current (at 40V, nominal actuation voltage of the switches) as failure criterion.
All tested structures present failure between 300V to 350V, without any significant dependence on L or W, as shown by the sudden increase from about 10pA up to the set compliance current level ($2\mu A$) of the leakage current.

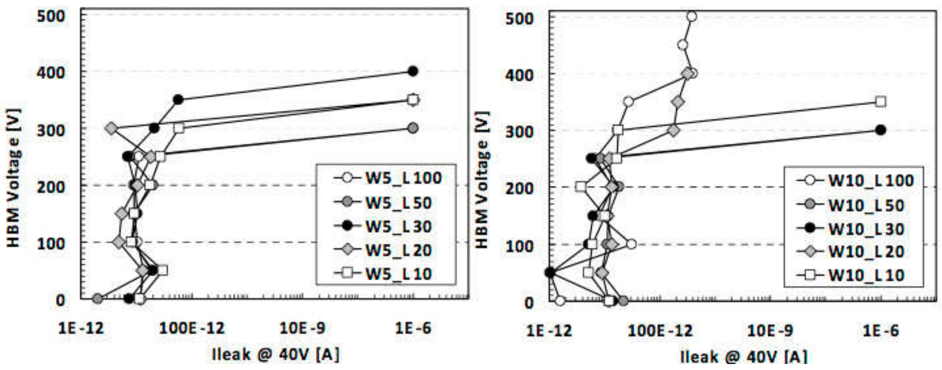

Figure 5.12: Results of the HBM-like stress carried out on the test structures with polysilicon line width of $5 \mu m$ (left), and $10 \mu m$ (right). The leakage current measured at 40V has been used as failure criterion

This lead to the result that the failure is due to the dielectric breakdown occurring in the cross between the polysilicon line and ground, and it is also confirmed by optical visible sparks in that zone. Devices $W10_L100$ and $W10_L20$, characterized by a lower increase of the leakage current than the other structures have shown the same sparks.

5.2.3 Electro-Mechanical Simulations

The mechanical inertia of movable parts on RF- MEMS switches (not present in solid state devices) acts as a low pass filter to very fast transients (like ESD events) applied to the actuator pad. It has already been demonstrated the detrimental effects of strong ESD events on the reliability of RF-MEMS switches. However, it is interesting to investigate how the suspended membrane reacts to short electrical overstress, especially considering electrostatically actuated MEMS, which base their functioning on an electrostatic potential between the actuator electrodes and the suspended structure.
In order to better understand if an ESD event applied to the actuation pad can be energetic enough to bend or to fully actuate an RF-MEMS switch, an electro-mechanical Finite Element Method (FEM) simulations of straight beams based devices have been performed.
The actuation time at increasing bias voltages has been studied. Switches actuation times have been measured biasing the devices with a rectangular shape voltage pulse (Hp 8114, 5ns rise time), applying a 6GHz, 0dBm RF

signal to the RF-IN pad, and connecting the RF-OUT pad to a Tektronix TDS 6804 (8 GHz analog bandwidth) DSO. The actuation time has been defined as the time the RF-OUT signals spends to reach the 90% of its final value, starting from the rising of the bias voltage. Actuation time measurements for straight beams based switches are reported in Figure 5.13.

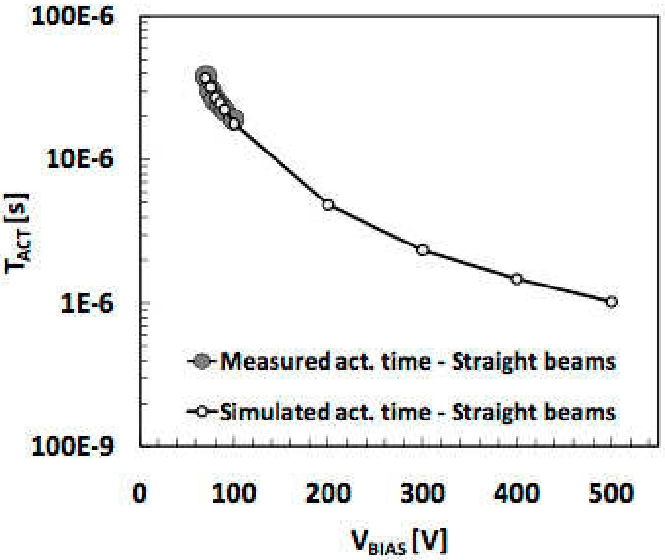

Figure 5.13: Measured and simulated actuation time of studied RF-MEMS switches at increasing bias voltage

Electro-mechanical simulations have been performed in order to evaluate the maximum displacement of the suspended membrane at increasing bias voltage, and at different pulse length (in the range of typical ESD-like events), the results are shown in Figure 5.14

Considering the simulation of Figure 5.14, at 400V, using a 100ns long pulse, a maximum displacement of 10nm is predicted. If we consider that 400V roughly corresponds to the maximum voltage applicable to the actuator pad before dielectric breakdown occurs between the polysilicon line and ground, it is easy to understand that there is virtually no movement of the suspended membrane during a 100ns TLP test.

Things change if we consider HBM-like test with pulses in the range of μs. According to Figure 5.14, a $1\mu s$ long pulse at 400V causes a displacement of almost $1\mu m$, that means one third of the initial air gap. Finally we can say that an ESD event can be energetic enough to bend the suspended

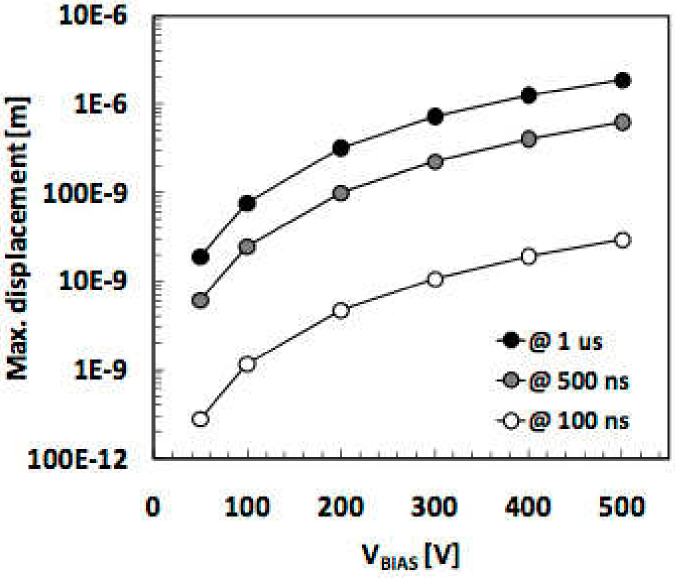

Figure 5.14: Maximum displacement of the suspended membrane at increasing bias voltage, and at different pulse length

membrane making possible an unwanted actuation.

5.3 EOS Induced Stiction

In conjunction with the traditional measure of both RF and electro-mechanical parameters of MEMS switches measured in the previous section, the measurement of I_{ACT} have been studied: during the S-Parameters characterization (I), and in a fastest way considering only the actuator structure (II, sweeping the voltage at the actuation pad vs. ground).
In order to better understand the evolution of the actuator current, ad-hoc developed test structures have been fully characterized. These are square capacitors ($440\mu m$ x $440\mu m$), without any movable parts, made with a polysilicon top electrode, a 100nm SiO_2 LTO, and an $Al1\%Si$ bottom electrode. These capacitor test structures made it possible to investigate the influence of the trapped charge on the actuator current and, in general, on the behavior of the full MEMS switch. The measurement setup used for the capacitors is the same used for switches characterization, but, in this case, only I_{ACT} has been measured (no S-Parameters).

5.3.1 Dielectric charging and actuator current

The comparison of S_{21} and I_{ACT} measurements of a shunt, meander-based switch is reported in Figure 5.15

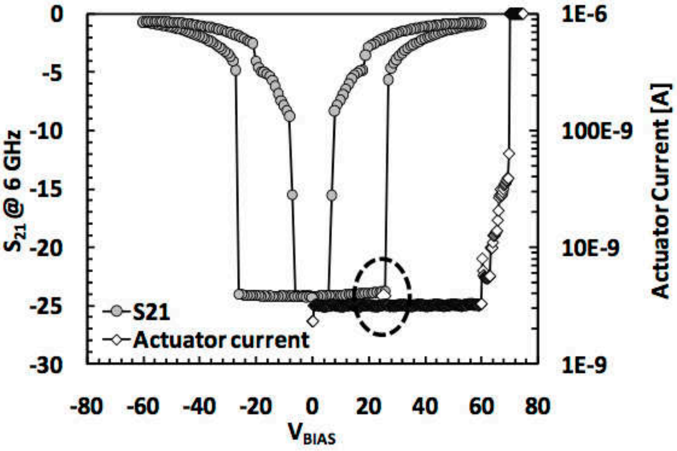

Figure 5.15: Comparison of S_{21} and I_{ACT} measurements of a shunt meander-based switch. I_{ACT} compliance has been set to $1 \mu A$

As it is possible to notice from Figure 5.15, I_{ACT} can furnish a precise value of the switch actuation voltage ($V_{ACT} = 25.5V$, as highlighted by the dotted circle in Figure 5.15), due to the transient increase of the capacitor displacement current, and the value is in perfect agreement with the S_{21} variation due to the actuation of the switch. Furthermore, it is interesting to notice that I_{ACT} suddenly increases after about 60V, precursor of the breakdown of the dielectric layer. It must be noted that a compliance level of $1 \mu A$ was set during the measure shown in Figure 5.15. Without setting a compliance value on the maximum current level, the device could remain stuck, as it will be discuss in the next section.

In order to better investigate the behavior of I_{ACT}, similar measurements have been repeated on capacitors test structures. An example of a typical I-V curve shown by a fresh capacitor is shown in Figure 5.16. Like in the measurement of a full switch, at about 60V the current starts to increase (phase 1), and, during the phase 2, the current decreases showing an hysteresis-like behavior.

This phenomenon can be attributed to the upward bending of the oxide

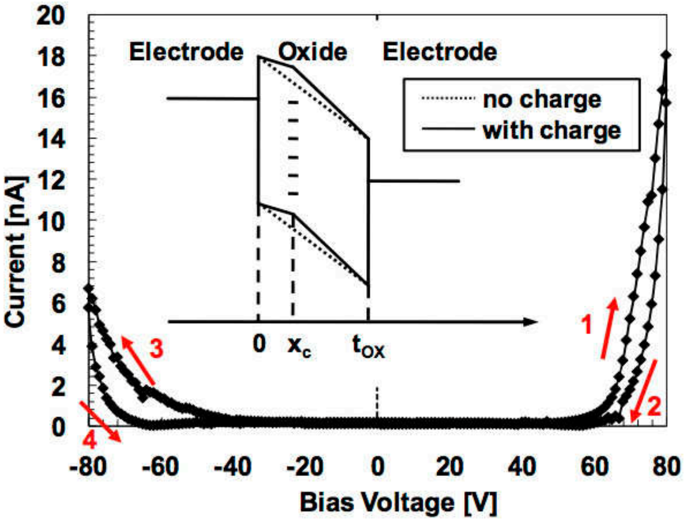

Figure 5.16: Evolution of I_{ACT} on a fresh test structure during the test. The arrows indicates the sweep direction. The inset shows a simplified schematic of the capacitor bands diagram before (dotted line) and after (continuous line) negative charge injection in the oxide

band diagram (see the inset in Figure 5.16: X_C = charge barycentre, t_{OX} = oxide thickness), leading to a reduction of the current flowing through the oxide (tunnel effect, or trap-assisted tunnel mechanisms) [42].

The measurements have been consecutively repeated for 100 times, and in Figure 5.17 it is reported the evolution of selected (#1, #10, #100) I-V characteristics during the test.

In order to investigate the evolution of the current during the test, the current value measured at 80V has been graphed in the inset of Figure 5.17. It decreases exponentially, and this can be explained by a continuous injection of negative charge in the dielectric. The negative charge causes an increase in the oxide barrier leading to a decrease in the current, with a saturation on the charge accumulation value after some repetitions of stress.

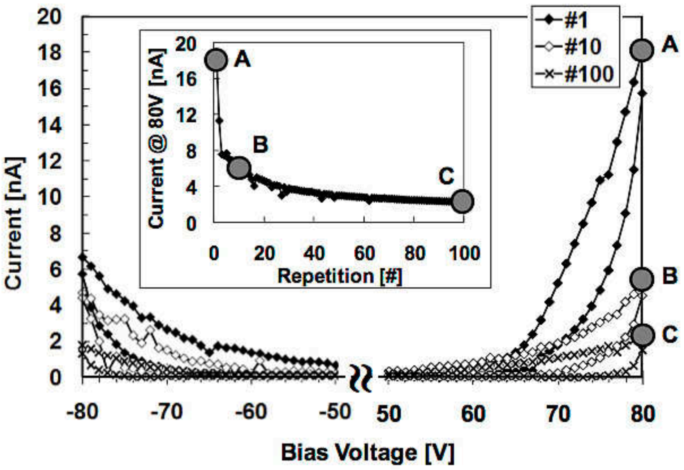

Figure 5.17: Evolution of I_{ACT} after 1, 10, and 100 measurement cycles. The x-axis is split for clarity purpose. The inset shows the decrease of I_{ACT} at 80 V caused by charge trapping

5.3.2 Stiction induced by dielectric breakdown

As already shown in Figure 5.15, it is interesting to note that I_{ACT} starts to suddenly increase for $V_{BIAS} > 60V$, due to the breakdown of the oxide layer between the suspended membrane and the actuator line. The region affected by the dielectric breakdown is highlighted in Figure 5.18b.

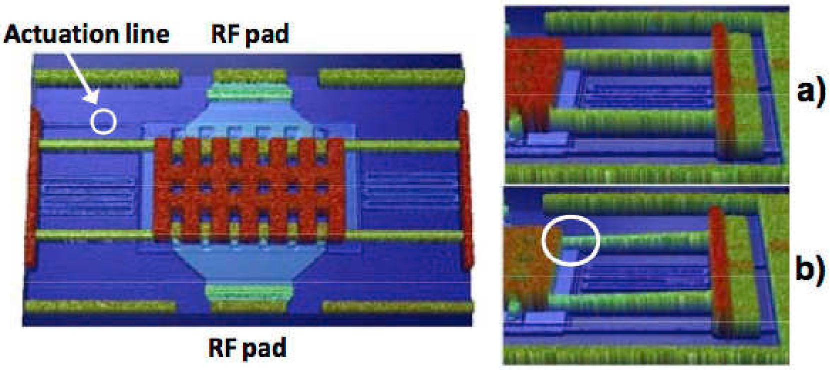

Figure 5.18: Optical profilometer images of tested devices: un-actuated (a), and actuated ($V_{BIAS} = 60V$). The circle in (b) highlights the zone where the dielectric breakdown occurs

It has been noticed that if the actuator current is not limited (setting the current compliance level to a maximum value of $1\mu A$), the dielectric breakdown can lead to a permanent stiction of the suspended membrane. In Figure 5.19 we show the evolution of S-Parameters and actuator current during the test with no compliance set on I_{ACT}

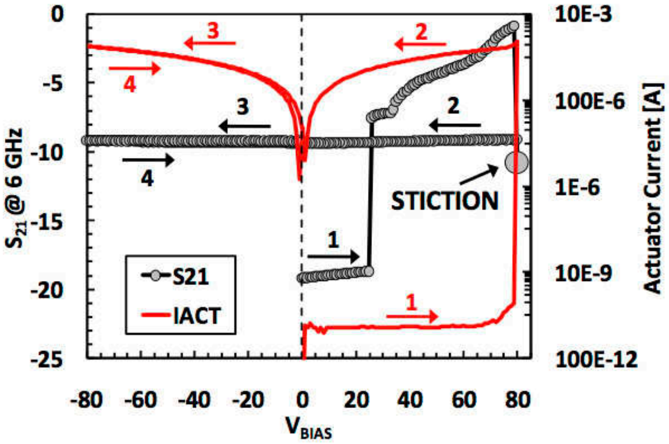

Figure 5.19: Comparison of S_{21} and I_{ACT} measurements with no current limit. The device remains stuck, in the point highlighted by the emission microscope image reported in Figure 5.20

At $V_{BIAS} \sim 80V$, I_{ACT} increases up to about 2mA; from that point the actuator assumes an ohmic behavior and the S_{21} parameter does not show any variation during the test. In this case the dielectric breakdown has lead the device to remain stuck and partially bended, since the S_{21} parameter assumes an intermediate value between the not-actuated, and the actuated values. Furthermore, the stiction occurrence has been confirmed by the prickling of the membrane, showing the bridge rotating around the point in which the breakdown occurred. Another confirmation is given by emission microscope (Hamamatsu PHEMOS-200) measurements, that clearly indicates the point where the failure has occurred, as shown in Figure 5.20.

Devices with different anchorage layout (without crossing with the actuation electrodes) have been tested, obtaining an highly increased robustness.

From this breakdown characterization between suspension and bottom actuator electrode, a simple design guide-line that should be observed to improve the reliability of such devices, could be avoid the crossing between the ac-

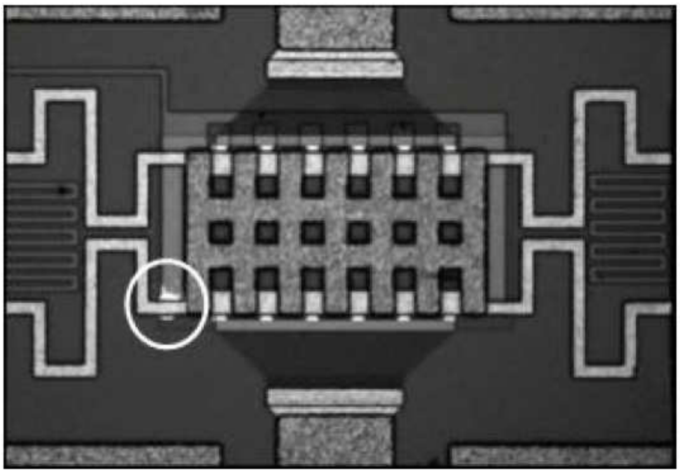

Figure 5.20: Emission microscope image of the stuck device after the dielectric breakdown (see Figure 5.19). The stiction has occurred in the area highlighted by the circle

tuator area and the suspended structure.

Capitolo 6

Radiation sensitivity for space application

Small dimensions and light weight make RF-MEMS switches very appealing for spatial applications, in particular for nano satellites. However, there are still some open issues that need to be overcome, especially in the harsh space environment where radiation induced damage is one of the main causes of failure as presented in Chapter 2. In particular, the behavior after exposure to ionizing radiation of devices having mechanical motion governed by electric fields across insulators has been seldom studied, mainly in MEMS sensors [44] or capacitor-like structures [45]. Just few authors have analyzed complete RF-MEMS devices [46], [47]

6.1 Introduction to radiation stress

It is well known that space can be an harsh environment for traditional solid state devices. Ionizing radiation comes in form of protons or ions trapped in the van Allen belts, of solar wind (with its periodical variations), and of protons and ions of galactic origin [48]. In the last years, radiation and EOS/ESD phenomena have been addressed as the main causes of mission failure, as reported by Koons in [32]. While most of the works consider only traditional solid state electronic components, recent studies have demonstrated that also micro-mechanical structures can be hampered by radiation damages.

Considering standard satellites, the radiation shield has been proved to be

a good solution to guarantee the electrical device lifetime during space missions. However, since the best applications for RF-MEMS devices would be nano-satellites, the efficiency of such a protection on small and light satellites needs to be verified. Further, a relatively thick shielding helps reducing the electrostatic charging and the total dose delivered to the electronic devices, but it cannot totally suppress it.
The effects of ionizing radiation on microelectronic devices can be divided into three categories. Single Event Effects are the macroscopic manifestation of single ions, such as the bit flip in a SRAM. To date, this should not be a problem with MEMS. Total Ionizing Dose effects are the progressive buildup of defects, mainly in the dielectric layers, due to the energy loss via ionization. Electrically active defects can be of different kinds, including charge trapping (E' and Pb centers), Si/SiO_2 interface defects, and the generation of mobile charge [49]. These sort of effects need to be considered for RF-MEMS since charge trapping is universally recognized as one of the most impairing problems for the reliability of electrostatically actuated switches. Finally, even the most ionizing particles lead to a certain amount of Non Ionizing Energy Loss (NIEL), that is, an energy loss due to interactions with atomic nuclei and not to the direct generation of electron/hole pairs. These interactions typically result in the generation of point defects which can, for example, degrade the gain of bipolar transistors [50]. In the same way, NIEL can lead to a modification of the Young Modulus of adopted materials, going to modify the mechanical properties of the MEMS structural parts, but also making the device more vulnerable to creeping and fracture.
Several types of devices designed by the University of Bologna have been tested.

Figure 6.1: Schematic process description of tested devices.

The device have the same layout already seen in section 3.4.1 and the schematic process description is shown in Figure 6.1. Starting from the substrate, on the top of it a 600nm layer of polysilicon is deposited and it is covered with 400nm of TEOS+LTO. Over the oxide there are 200nm of gold for the transmission line and, on top of it, there is the suspended membrane ($5\mu m$ of gold) separated by $3\mu m$ of air gap.
RF-MEMS switches have been submitted to protons and x-rays radiation sources analyzing the impact of such a stress on the RF and electrical parameters of the devices with the increase of the radiation dose, and during the successive days of annealing. The measurements set-up is the one already used for the DC Characterization.

6.2 Protons radiation stresses

An excerpt of the complete characterization carried out on a shunt switch after growing doses of 1, 10, and 30Mrad (SiO_2) protons stresses, and during the subsequent room temperature annealing, is reported in Figure 6.2

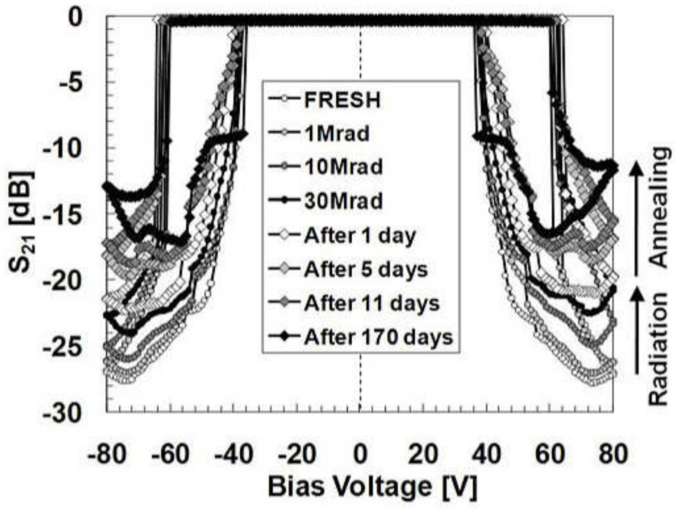

Figure 6.2: Degradation of S_{21} for a shunt switch (straight beams) during the protons radiation stress and the successive days of storage (test conditions: $f_{RF} = 6GHz$, $P_{RF} = OdBm$)

Looking at Figure 6.2, an important degradation of the insertion loss is visible while the actuation voltage remains basically the same. The relatively small variations of the actuation voltage with the increasing dose appears to exclude large charge trapping as the only cause for insertion losses degradation.

Figure 6.3 shows the evolution of V_{ACT} and $-V_{ACT}$ for a series switch (up) and a shunt one (bottom, from Figure 6.2) during the protons radiation stress and the successive days of storage.

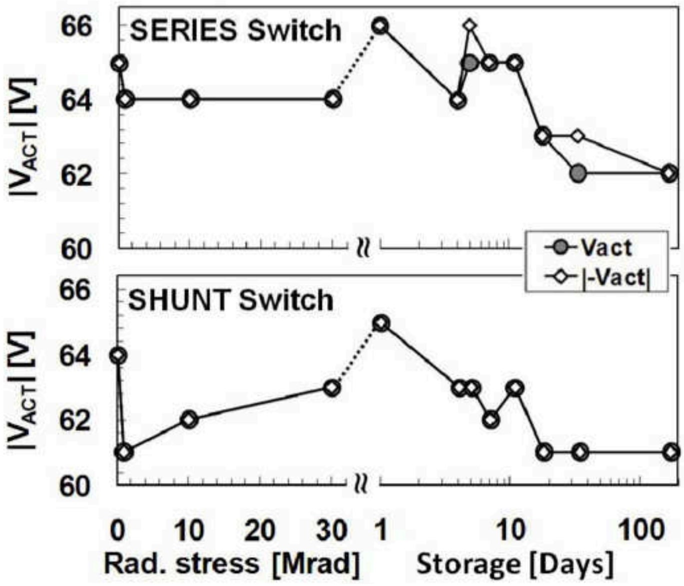

Figure 6.3: Evolution of V_{ACT} and $-V_{ACT}$ for a series switch (up) and a shunt one (bottom, from Figure 6.2) during the protons radiation stress and the successive days of storage

Positive charge trapping would have changed both the actuation and the release voltages toward lower values. On the opposite, during the storage time, charge de-trapping would have moved $|V_{ACT}|$ and $|V_{REL}|$ toward their original values. On the opposite, both follow a complex behavior with a fast degradation, a partial recovery during irradiation, and an apparent worsening during post-irradiation storage. Such a complex behavior suggests that the phenomena underlying the degradation of devices should have a complex nature, probably resulting from the superimposition of different effects having different temporal evolutions.

Figure 6.4 shows the evolution of the S_{21} parameter measured at 80V during the radiation stress and later, during the storage.

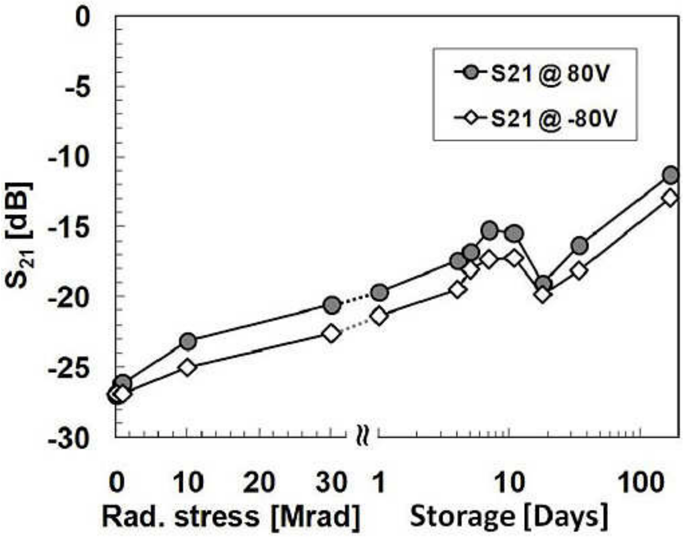

Figure 6.4: Evolution of the S_{21} parameter measured at 80V during the radiation stress and later, during the storage

It seems that this degradation is not caused by coplanar waveguides (CPW) or substrate losses because the measurement does not change even changing the frequency in the range 100KHz - 6GHz. Moreover, an irradiated CPW test structure does not show any loss.

Figure 6.5 shows the comparison between the S_{21} curve after 30Mrad protons stress measured at 6GHz and the one measured at 100KHz. The curves are almost identical leading to the fact that there is not a frequency dependency of this behavior.

Furthermore, the same irradiated devices have been submitted to cycling stress and they have shown a faster degradation, if compared with fresh devices, as presented in Figure 6.6.

A possible explanation could be found in the degradation of the metal-to-metal contact (increased series resistance). In principle, the damage induced by 2MeV protons could be due to either displacement damage (latice defects directly induced by proton-nucleus interactions), or to ionizing damage (protons generate columns of charges in the device that recombine and/or move generating the actual damage) [51].

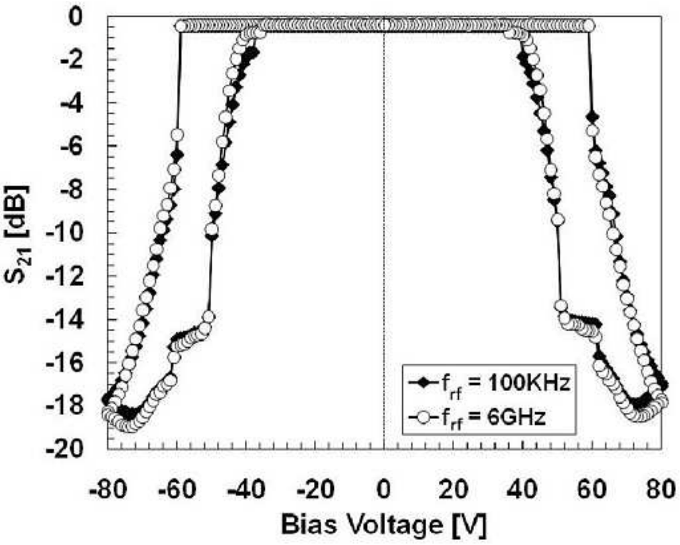

Figure 6.5: Comparison between the S_{21} curve after 30Mrad protons stress measured at 6GHz and the one measured at 100KHz

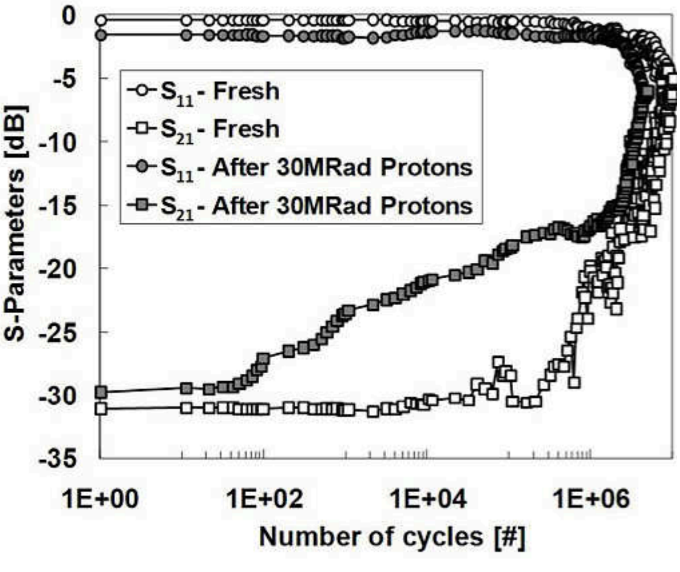

Figure 6.6: Comparison of the cycling robustness of a fresh series switch with a 3OMrad protons stressed one($V_{bias} = 80V$, $f_{RF} = 6GHz$, $P_{RF} = OdBm$)

Figure 6.7 shows the Monte Carlo TRIM simulation [52] of displacement damage for 2MeV protons for the measured devices. The inset highlights the $vacancies/cm^3$ just below the air-gap.

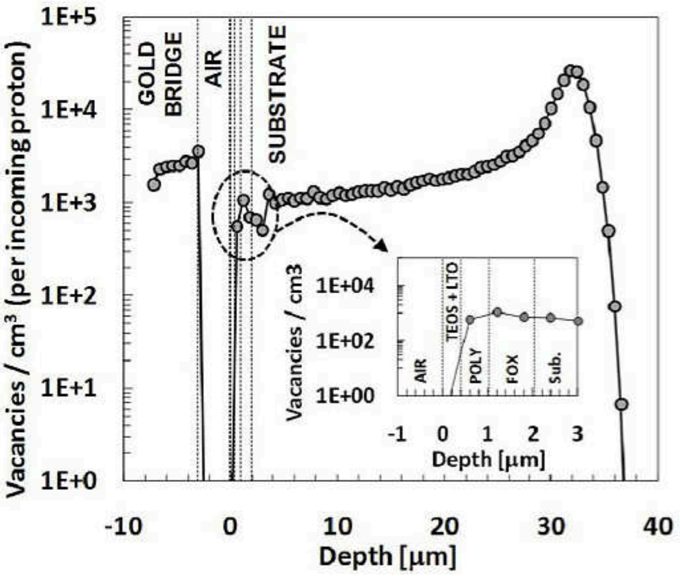

Figure 6.7: Monte Carlo TRIM simulation of displacement damage for 2MeV protons for the measured devices. The inset highlights the $vacancies/cm^3$ just below the air-gap

Looking at Figure 6.7 different observations can be done.
First: the range of 2MeV protons is more than enough to cross all the device active area. This confirms that protons are crossing the whole device, and that all parts (bridge, actuators, substrate) may in principle be the origin for the observed degradation.
Second: the displacement damage is mainly located in the bulk of the silicon. Since this part of the device has no role in the electrical performances of the switch, the easiest conclusion one can draw is that performance degradation should be linked someway to ionizing damage.
Third: displacement damage in the gold layer is much higher than that in the surface silicon, due to the larger mass of the former. Hence, a contribution of NIEL cannot be neglected.
The fluences used (up to 1.7x10^{13} for the higher dose) are actually compatible with literature results on displacement damage in silicon devices [53].

6.3 X-rays radiation stresses

In order to better understand the behavior shown in the previous section, devices with the same structure have been tested with a radiation source where displacement damage is in first approximation negligible, 10keV x-rays. 70 devices have been tested with up to 1Mrad, and the summary of results are reported in Figure 6.8.

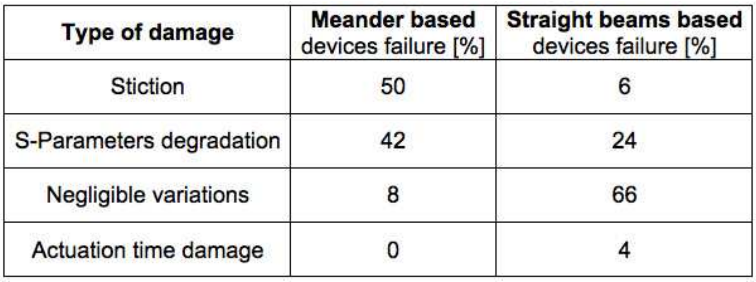

Type of damage	**Meander based** devices failure [%]	**Straight beams based** devices failure [%]
Stiction	50	6
S-Parameters degradation	42	24
Negligible variations	8	66
Actuation time damage	0	4

Figure 6.8: X-ray radiation stress induced failures. Number of tested devices: 30 meanders based, 40 straight beam.

Figure 6.9 shows the comparison of S_{21} of a fresh shunt switch, after 1Mrad x-rays stress, and after 1 month of storage.

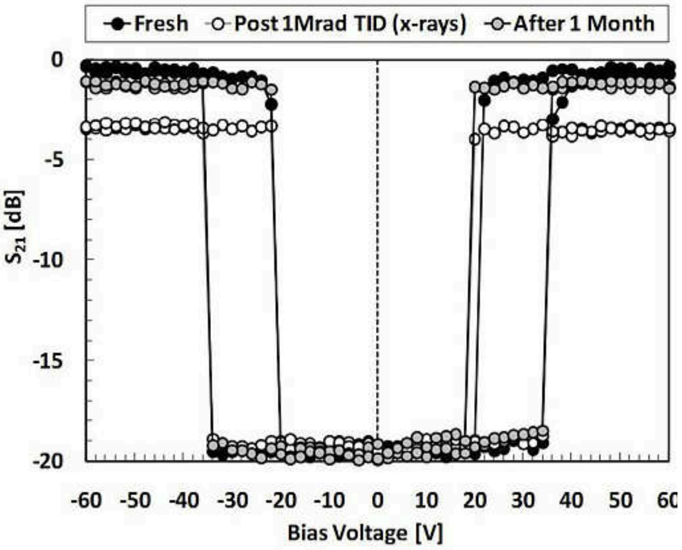

Figure 6.9: Comparison of S_{21} of a fresh shunt switch, after 1Mrad x-rays stress, and after 1 month of storage (showing the recovery)

From the curves it is possible to notice the almost complete recovery obtained after 1 month of storage at room temperature. There are no significant changes in actuation and deactuation voltages.
This more pronounced recovery found after x-rays irradiation, if compared to protons, suggests that displacement damage may actually play a role in the degradation of switches performance. On the other side, recombination kinetics is not the same after irradiation with x-rays and protons (especially at relatively low energies such as those used here [51]), and phenomena purely linked to ionization damage cannot be excluded.

Conclusions

RF-MEMS switches can be considered promising devices in all that situation in which small size and low power consumption are a priority.
However, several reliability issues need to be solved before their real usage in critical situations such as spatial applications or other applications in which reliability is considered a key factor.
In this work several devices with different layout and peculiarities have been tested, proposing a standard way for reliability testing. Starting from the more standard measurements like DC characterizations and cycling, the attention has been moved on reliability issues related to long time actuation, electrical over stress or electrostatic discharge and finally to radiation.
It has been demonstrated that standard electrical measurements and cycling stresses can not give a full idea of the real performances of RF-MEMS switches. Moreover, it has been studied how the suspensions shape impacts on the electrical parameters (pull-in and pull-out voltages) of the devices and which is the influence of the suspended membrane geometry and bias voltage on the cycling robustness.
Considering long actuation time stress, an ad hoc set-up has been realized and several devices have been tested finding the most reliable layouts.
Furthermore, the influence of continuous actuation stress on the reliability of dielectric-less ohmic RF-MEMS cantilever-based switches has been studied. Different designs have been compared, identifying in the substrate charging the first cause of narrowing and shifting of the hysteresis-like curves, possibly leading to stiction. The design rule of carefully covering substrate regions have also been demonstrated, aiming at the improvement of reliability versus continuous actuation of such switches. Breakdown occurrence have also been investigated, showing experimental results supported by both emission and optical microscope images.

An in-depth study of EOS/ESD phenomena of ohmic RF-MEMS switches have been done considering both not actuated, partially bended, and fully actuated membrane. It has been found that the robustness is strictly dependant by the suspension shape, by the type of contact between the suspended membrane and the transmission line, and by the value of the actuation voltage. Moreover, a good correlation of the range of breakdown voltage between TLP and HBM tests have been found.

The current drained by the actuation electrode has been investigated, finding interesting correlation between I_{ACT} and the actuation voltage, and the presence of charge trapping phenomena.

Capacitor test structures have been characterized, investigating the influence of charge trapping in the evolution of the leakage current.

It has been shown that stiction phenomena can also be induced by the dielectric breakdown of the insulator between the suspended membrane and the actuation electrode layer, and, like in the previous cases, I_{ACT} can furnish interesting information on the stiction and breakdown occurrence.

Finally, the influence of radiation have been investigated irradiating devices with protons and x-rays and showing how switches performances can be impacted by ionizing radiation, in particular the S-Parameters. While the devices tested with x-ray have shown a complete recovery 1 month after the stress with no impact on the actuation voltage, the usage of protons have caused a S-Parameters degradation similar to the one obtained with the cycling stress leading to a continue degradation even after the stress. This behavior is quite unusual but, if confirmed by further measurements, it should mean that proton stress can be used as accelerating factor for long term stress.

Appendix A

Software for automatic measurements using Labview

When developing a new technologies, a lot of measurements need to be done and, considering RF-MEMS devices, most of them are performed on wafer. This is the reason why developing a reliable, easy to use and fast methodology to test a great number of devices in a short time is a must for a forefront laboratory. In this section the development of an automatic measurement program will be presented.

The aim of the work is to realize an automatic measurement program to characterize and test MEMS structures in general, not only switches but also resonators, capacitors or other devices. Labview results to be the easiest and more efficient software for this purpose.

The program needs to be completely automatic in order to work 24/7 without any operators in the laboratory but it has to be easy to use in order to let all the people of the lab use it without a specific training period. At the same time, another requirement is the modularity. It is extremely important that people with different devices and test procedures can use it implementing new modules and improving the program.

The basic idea is to have in input just two files: 1 Wafer Map with all the coordinates of the different devices on the Wafer and 1 Test Plan with all the measurements that need to be performed and all the device that need to be measured.

A scheme of the general idea is presented in Figure A.1.

The two files are the inputs of the Labview program that controls all the

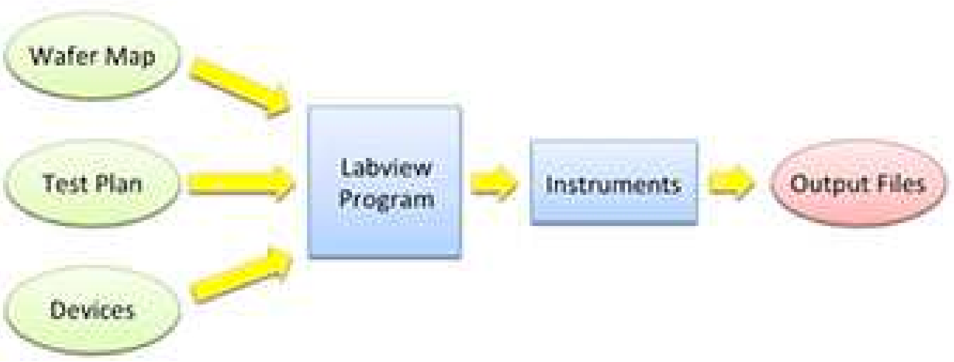

Figure A.1: Scheme of the automatic measurement program

instruments and saves all the measurements on different output files.
XML files have been used for the inputs because it is a free standard language and these type of files can be open and edit with a lot of programs.
An example of a Wafer Map file is shown in Figure A.2

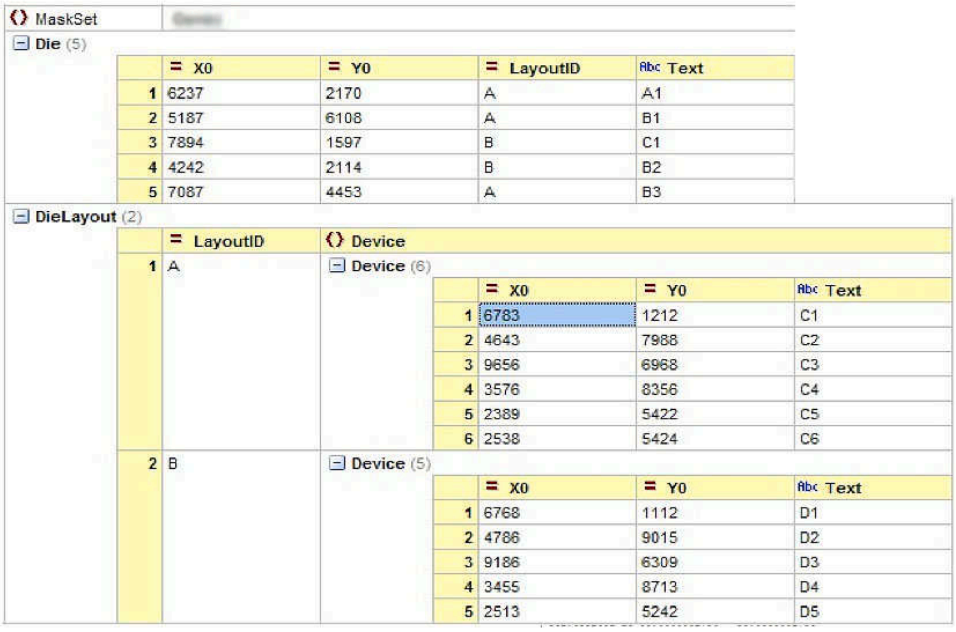

Die (5)

	X0	Y0	LayoutID	Text
1	6237	2170	A	A1
2	5187	6108	A	B1
3	7894	1597	B	C1
4	4242	2114	B	B2
5	7087	4453	A	B3

DieLayout (2)

	LayoutID	Device
1	A	Device (6)
2	B	Device (5)

1 A – Device (6)

	X0	Y0	Text
1	6783	1212	C1
2	4643	7988	C2
3	9656	6968	C3
4	3576	8356	C4
5	2389	5422	C5
6	2538	5424	C6

2 B – Device (5)

	X0	Y0	Text
1	6768	1112	D1
2	4786	9015	D2
3	9186	6309	D3
4	3455	8713	D4
5	2513	5242	D5

Figure A.2: Example of Wafer Map file

From the figure two different areas can be distinguished: Die and DieLayout.
In the Die section all the Die of the wafer are reported (A1, B1, C1, B2...)

with their general layout (A or B) and with the coordinates (X0 and Y0). In the DieLayout part, for every type of general layout (in this example only A and B) all the devices are reported (C1, C2, C3,...) with their coordinates. An example of a Test Plan file is shown in Figure A.3

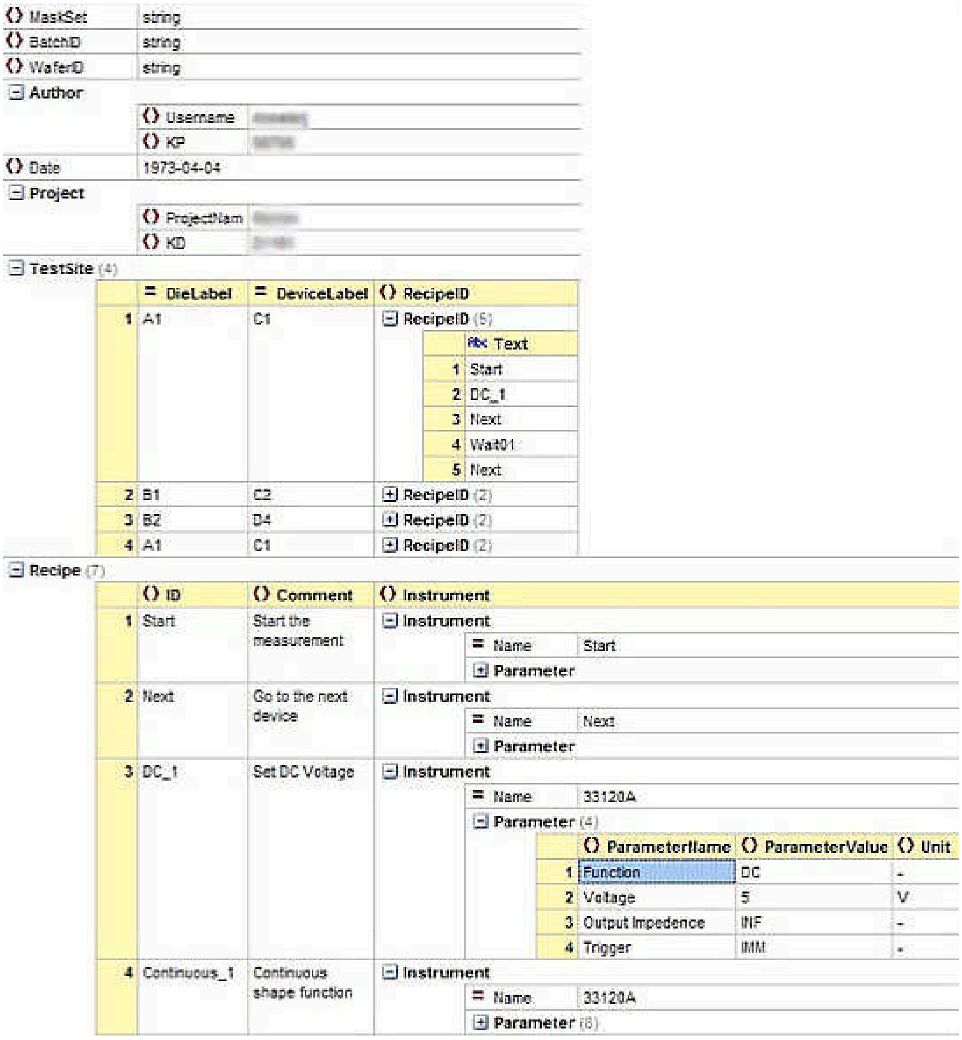

MaskSet	string	
BatchID	string	
WaferID	string	
Author		
	Username	[redacted]
	KP	[redacted]
Date	1973-04-04	
Project		
	ProjectNam	[redacted]
	KD	[redacted]

TestSite (4)

	DieLabel	DeviceLabel	RecipeID
1	A1	C1	RecipeID (5) Text 1 Start 2 DC_1 3 Next 4 Wait01 5 Next
2	B1	C2	RecipeID (2)
3	B2	D4	RecipeID (2)
4	A1	C1	RecipeID (2)

Recipe (7)

	ID	Comment	Instrument
1	Start	Start the measurement	Instrument Name Start Parameter
2	Next	Go to the next device	Instrument Name Next Parameter
3	DC_1	Set DC Voltage	Instrument Name 33120A Parameter (4) ParameterName ParameterValue Unit 1 Function DC - 2 Voltage 5 V 3 Output Impedence INF - 4 Trigger IMM -
4	Continuous_1	Continuous shape function	Instrument Name 33120A Parameter (8)

Figure A.3: Example of Wafer Map file

In this case three parts can be distinguished, in the first one all the useful information are reported such as MaskSet, BatchID, WaferID, who did the measurements (Username), Date and project information. These are needed to built the output file name in order to be easy recognizable.

The second part, called TestSite, contains the device to be measured, the die, and the list of measurements to be done in the order they need to be performed.

In the last part, called Recipe, every single measurement mentioned in the TestSite is fully described. In the Instrument part, the name of the instrument and all the parameters that have to be set for the specific measurement are defined.

With this system to perform a series of measurements on different devices is extremely easy even for people without specific training.

The output files are txt files and an example obtained after a C-t measurement is shown in Figure A.4

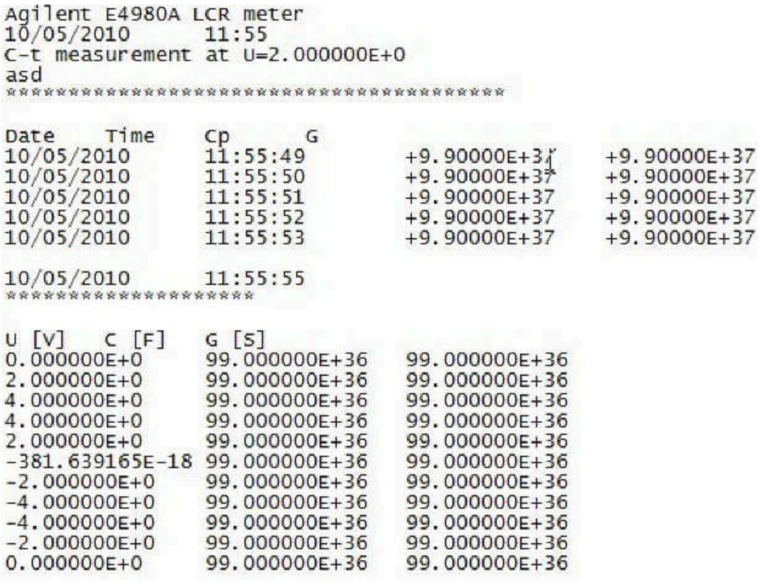

```
Agilent E4980A LCR meter
10/05/2010      11:55
C-t measurement at U=2.000000E+0
asd
****************************************

Date     Time     Cp       G
10/05/2010      11:55:49        +9.90000E+37    +9.90000E+37
10/05/2010      11:55:50        +9.90000E+37    +9.90000E+37
10/05/2010      11:55:51        +9.90000E+37    +9.90000E+37
10/05/2010      11:55:52        +9.90000E+37    +9.90000E+37
10/05/2010      11:55:53        +9.90000E+37    +9.90000E+37

10/05/2010      11:55:55
********************

U [V]   C [F]   G [S]
0.000000E+0     99.000000E+36   99.000000E+36
2.000000E+0     99.000000E+36   99.000000E+36
4.000000E+0     99.000000E+36   99.000000E+36
4.000000E+0     99.000000E+36   99.000000E+36
2.000000E+0     99.000000E+36   99.000000E+36
-381.639165E-18 99.000000E+36   99.000000E+36
-2.000000E+0    99.000000E+36   99.000000E+36
-4.000000E+0    99.000000E+36   99.000000E+36
-4.000000E+0    99.000000E+36   99.000000E+36
-2.000000E+0    99.000000E+36   99.000000E+36
0.000000E+0     99.000000E+36   99.000000E+36
```

Figure A.4: Example of output file for a C-t measurement

The program can fully control a Suss Microtec Vacuum Probe System PAV150 through the control of the probes, of the temperature and of the pressure. Moreover, Labview blocks have been realized for several instruments such as waveform generators, LCR meters and Network Analyzers. To add a new instruments at the program is easy and fast, it is enough to realize a labview block for the instruments and insert it in the main program.

The program can work in three different configurations:

Fully automatic Both Wafer Map and Test Plan files need to be loaded and the measurements are performed automatically for every device

Automatic Just the Test Plane needs to be loaded and the probes need to be placed manually

Manual No files need to be loaded, all the parameters can be specified through the program's Front Panel

The Front Panel of the program is shown in Figure A.5

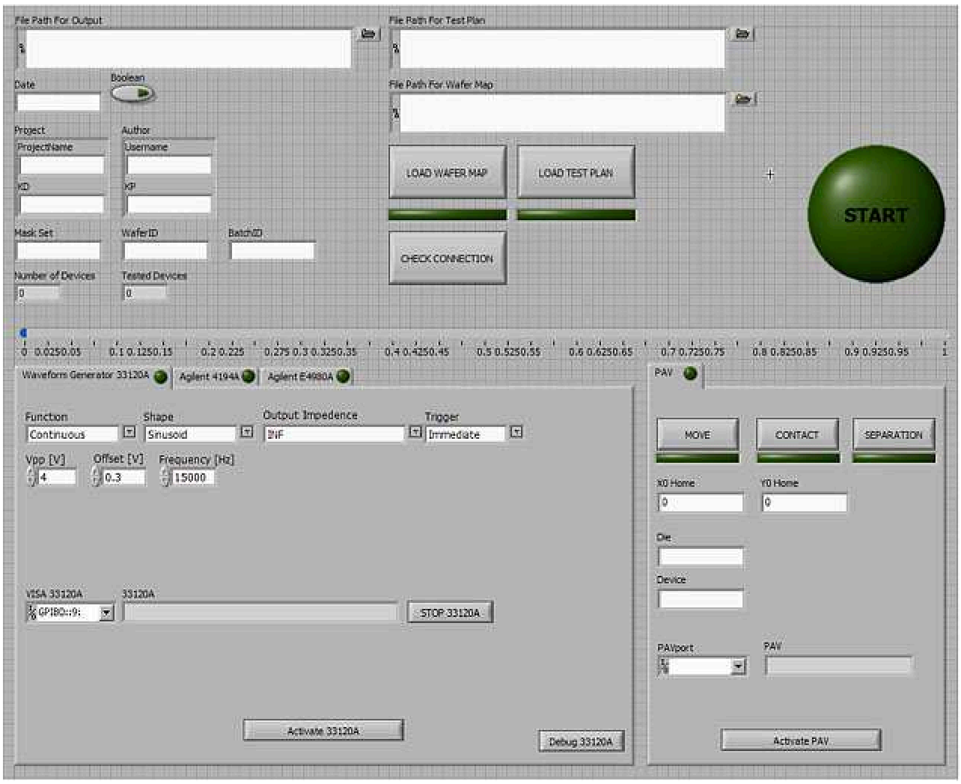

Number of Devices 0

Tested Devices 0

Function Continuous

Shape Sinusoid

Output Impedence INF

Trigger Immediate

Vpp [V] 4

Offset [V] 0.3

Frequency [Hz] 15000

VISA 33120A GPIB0::9:

X0 Home 0

Y0 Home 0

Figure A.5: Labview Front Panel of the main program

Publications

1. S. Stoffels, E. Autizi, R. Van Hoof, S. Severi, A. Witvrouw, H. A.C. Tilmans, and R. Puers, *"Physical Loss Mechanisms for resonant acoustical waves in Boron doped poly-SiGe deposited with Hydrogen dilution"*, Journal of Applied Physics 108, 084517 (2010) October 2010
2. A. Tazzoli, E. Autizi, M. Barbato, G. Meneghesso, F. Solazzi, P. Farinelli, F. Giacomozzi, J. Iannacci, B. Margesin, R. Sorrentino, *"Evolution of Electrical Parameters of Dielectric-less Ohmic RF-MEMS Switches during Continuous Actuation Stress"*, 39th European Solid-State Device Research Conference (ESSDERC), Athens, Greece, September 14-18, 2009
3. A. Tazzoli, E. Autizi, M. Barbato, F. Solazzi, J. Iannacci, P. Farinelli, F. Giacomozzi, B. Margesin, R. Sorrentino, G. Meneghesso, *"Impact of Continuous Actuation on the Reliability of Dielectric-less Ohmic RF-MEMS Switches"*, MEMSWAVE 2009, 10th International Symposium on RF MEMS and RF Microsystems, Trento, Italy, July 6-8, 2009
4. A. Tazzoli, G. Cellere, E. Autizi, V. Peretti, A. Paccagnella, and G. Meneghesso, *"Radiation sensitivity of ohmic RF-MEMS Switches for spatial applications"*, MEMS 2009, 22nd IEEE International Conference on Micro Electro Mechanical Systems, Sorrento, Italy, 25-29 January, 2009
5. A. Tazzoli, E. Autizi, V. Peretti, G. Meneghesso, *"Stiction Induced by Dielectric Breakdown on RF-MEMS Switches"*, MEMSWAVE 2008. 9th International Symposium on RF MEMS and RF Microsystems, Heraklion, Greece, 2008
6. A. Tazzoli, V. Peretti, E. Autizi, G. Meneghesso, *"Suspensions shape*

impact on the reliability of Ohmic rf-MEMS redundancy switches", International Reliability Physics Symposium, IRPS 2008, Phoenix, Arizona, USA, April 27-May 1, 2008

7. A. Tazzoli, V. Peretti, E. Autizi, G. Meneghesso, *"EOS/ESD Sensitivity of Functional rf-MEMS Switches"*, 30th annual EOS/ESD Symposium, Westin La Paloma, Tucson, Arizona, USA, September 7-11, 2008

8. N. Wrachien, E. Autizi, A. Cester, R. Portoghese and C. Gerardi, *"Readout drain current dependence of the programming window in nanocrystal memory cells"*, IEE-Electronics Letters, Volume 44, Issue 6, March 13 2008 Page(s):445-446

Bibliography

[1] G. Rebeiz, et al., *"RF MEMS Switches and Switch Circuits"*, IEEE Microwave Magazine, December 2001, pp. 59-71

[2] R. Plana, *"What's Hot in RF Components and Systems"*, Microwave Journal, February 2006, pp. 22-28

[3] R. Ramesham and R. Ghafkian, *"Challenges in Interconnection and Packaging of Microelectromechanical Systems (MEMS)"*, IEEE Electronic Components and Technology Conference, 2000

[4] W. D. van Driel, J. J. M. Zaal, D. G. Yang, M. van Kleef, G. Q. Zhang, *"Mechanical Reliability of MEMS Packages"*, IEEE Electronic Components and Technology Conference, 2008

[5] Z. Yufeng, T. Xiaoyun, C. Weiping, Z. Guowei and L. Xiaowei, *"Study of MEMS packaging technology"*, 6th International Conference on Electronic Packaging Technology, 2005

[6] J. Maciel, *"Recent Reliability Results in RF MEMS"*, Proceedings of the 2005 IEEE MTT-S Int. Microwave Symposium, Workshop Notes, WFE Recent Applications in RF MEMS, Long Beach, CA, June 12-17, 2005

[7] I. De Wolf, *"Reliability of MEMS"*, 7th International Conference on Thermal, Mechanical and Multiphysics Simulation and Experiments in Micro-Electronics and Micro-Systems, EuroSimE, 2006

[8] P.Blondy, A.Crunteanu, C.Champeaux, A.Catherinot, P.Tristant, O.Vendier, J.Cazaux, and L. Marchand *"Dielectric Less Capacitive MEMS Switches"* IEEE MTTS International Microwave Symposium Digest, June 2004

[9] D. Mardivirin, A. Pothier, M. El Khatib, A. Crunteanu, O. Vendier and P. Blondy, *"Reliability of Dielectric Less Electrostatic Actuators in RF-MEMS Ohmic Switches"*, 38th European Microwave Conference, Amsterdam, The Netherlands, 2008

[10] A. Ocera, P. Farinelli, P. Mezzanotte, and R.Sorrentino *"A novel MEMS reconfigurable hairpin line filter on silicon substrate"* Proceedings of the 36th European Microwave Conference, 2006

[11] A. Ocera, P. Farinelli, F. Cherubini, P. Mezzanotte, R. Sorrentino, B. Margesin, and F. Giacomozzi *"A MEMS Reconfigurable Power Divider on High Resistivity Silicon Substrate"* Proceedings of IEEE MTTS International Microwave Symposium Digest, 2007

[12] H. S. Newman, J. L. Ebel, D. Judy, and J. Maciel, *"Lifetime Measurements on a High-Reliability RF-MEMS Contact Switch"*, IEEE Microwave and Wireless Ccomponents Letters, 2008

[13] R. Chan, R. Lesnick, D. Becher, and M. Feng, *"Low-Actuation Voltage RF MEMS Shunt Switch With Cold Switching Lifetime of Seven Billion Cycles"*, Journal of Microelectromechanical Systems, vol. 12, no. 5, October 2003

[14] R. Gaddi et. al, *"Interdigitated low-loss ohmic RF-MEMS switches"*, NSTI Nanotech 2004, Boston, March 2004, vol. 2, p.327-330.

[15] P. Czarnecki, X. Rottenberg, P. Soussan, P. Nolmans, P. Ekkels, P. Muller, H.A.C. Tilmans, W. De Raedt, R. Puers, L. Marchand and I. De Wolf, *"New insights into charging in capacitive RF-MEMS switches"*, IEEE International Reliability Physics Symposium, Phoenix, AZ, 2008

[16] G. J. Papaioannou, M. Exarchos, V. Theonas, G. Wang, and J. Papapolymerou, *"On the Dielectric Polarization Effects in Capacitive RF-MEMS Switches"*, IEEE MTT-S International Microwave Symposium Digest, 2005

[17] G. J. Papaioannou and J. Papapolymerou, *"Dielectric charging mechanisms in RF-MEMS capacitive switches"*, 2nd European Microwave Integrated Circuits Conference, Munich, Germany, October 2007

[18] G. J. Papaioannou, M. Exarchos, V. Theonas, G. Wang, and J. Papapolymerou, *"On the dielectric polarization effects capacitive RF-MEMS switches"*, IEEE MTT-S International Microwave Symposium, Long Beach, CA, 2005

[19] E. K. Chan, K. Garikipati, and R. W. Dutton, *"Characterization of contact electromechanics through capacitance-voltage measurements and simulations"*, Journal of Microelectromechanical Systems, vol. 8, no. 2, pp. 208-217, June 1999

[20] W. M. Spengen, R. Puers, R. Mertens, I. De Wolf, *"Experimental characterization of stiction due to charging in RF-MEMS"*, IEEE International Electron Devices Meeting (IEDM), San Francisco, CA, December 9-December 11, 2002

[21] B. Pillans et al. *"RF power handling of capacitive RF MEMS device"*, IEEE MTT-S International Microwave Symposium Digest,2002

[22] B. Ducarouge et al. *"Power capabilities of RF MEMS"* 24th International Conference on Microelectronics (MIEL), Nis (Serbie), 16-19 Mai 2004, pp.65-70

[23] B. D. Jensen, H. Kuangwei, L. Chow, K. Saitou, J. S. Volakis and K. Kurabayashi *"Asperity heating for repair of metal contact RF MEMS switches"*, IEEE MTT-S International Microwave Symposium Digest, Part Vol.3, Fort Worth, TX, USA, pp.1939-42, June 6-11 , 2004.

[24] B. D. Jensen, L. W. Chow, R. F. Webbink, K. Saitou, J. L. Volakis and K. Kurabayashi *"Force dependence of RF MEMS switch contact heating"* 17th IEEE International Conference on Micro Electro Mechanical Systems. Maastricht MEMS 2004

[25] B. Stark, *"MEMS Reliability Assurance Guidelinesfor Space Applications"*, Jet Propulsion Laboratory, Pasadena, California JPL Publication 99-1

[26] B. Schauwecker, J.Mehner, K. Strohm, H. Haspeklo, and J.F. Luy, *"Investigations of RF shunt airbridges among different environmental conditions"*, Sens. Act. A, vol. 114, pp. 49-58, 2004

[27] B. Pillans, *"RF MEMS reliability at Raytheon"*, in Proc. IEEE Int. Microwave Symposium Workshop WFF: Reliability Testing Reliability Enhancement RF MEMS Switches, June 2004

[28] C. Goldsmith, J. Ehmke, A. Malczewski, B. Pillans, S. Eshelman, Z. Yao, J. Brank, and M. Eberly, *"Lifetime characterization of capacitive RF MEMS switches"*, in Proc. IEEE International Microwave Symposium, vol. 1, May 2001, pp. 227-230

[29] C. L. Goldsmith, D. I. Forehand, Z. Peng, J. C. M. Hwang, and John L. Ebel, *"High-Cycle Life Testing of RF-MEMS Switches"*, IEEE/MTT-S International Microwave Symposium, 2007

[30] *"Radiation Effects-From Particles to Payloads"*, Short course Notebook at 2002 IEEE NSREC, July 15, 2002

[31] Campbell, W.S., A. B. Jenkin, M.E. Sorge, *"Orbital Debris Hazard Assessment Methodologies for Satellite Constellations"*, Adv. Astron. Sci., Vol. 105, 639-652, 2000

[32] Koons H. C., J. E. Mazur, R. S. Selesnick, J. B. Blake, J. F. Fennell, J. L. Roeder, P. C. Anderson, *"The impact of the space environment on space systems"*, Aerospace Technical Report TR-99(1670)-1, 1999

[33] G. Rebeiz, *"RF MEMS theory, design, and technology"*, Wiley-Interscience, 2003

[34] B. Lacroix, A. Pothier, A. Crunteanu, C. Cibert, F. Dumas-Bouchiat, C. Champeaux, A. Catherinot, and P. Blondy, *"Sub-Microsecond RF MEMS Switched Capacitors"*, IEEE Transactions on Microwave Theory and Techniques, vol. 55, no. 6, June 2007

[35] B. D. Jensen, et al., *"Effect of Nanoscale Heating on Electrical Transport in RF MEMS Switch Contacts"*, Journal of Microelectromechanical Systems, vol. 14, no. 5, October 2005, pp. 935-947

[36] X. Rottenberg, et al., *"Analytical Model of the DC Actuation of Electrostatic MEMS Devices With Distributed Dielectric Charging and Nonplanar Electrodes"*, Journal of Microelectromechanical Systems, vol. 16, no. 5, October 2007, pp. 1243-1253

[37] D. Mardivirin, et al., *"Charging in Dielectricless Capacitive RF-MEMS Switches"*, IEEE Transactions on Microwave Theory and Techniques, vol. 57, no. 1, Jan. 2009, pp. 231-236

[38] A. K. Jonscher, *"Dielectric relaxation in solids"*, J. Phys. D, Appl. Phys., vol. 32, 1999, pp. R57-R70

[39] A. Tazzoli, et al., *"Electrostatic Discharge and Cycling Effects on Ohmic and Capacitive RF- MEMS Switches"*, IEEE Trans. on Device and Materials Reliability, vol. 7, no. 3, Sept. 2007, pp. 429-437

[40] W. D. Greason, *"Effect of Charge Injection due to ESD on the Operation of MEMS"*, IEEE 42nd Industry Applications Conference, 2007, pp. 2188-2193

[41] A. Tazzoli, et al., *"Transmission Line Pulse (TLP) Testing of Radio Frequency (RF) Micro- machined Microelectromechanical Systems (MEMS) Switches"*, EOS/ESD Symposium, 2006, pp. 295-303

[42] R. Kies, et al., *"Improved method for the extraction of oxide charge density and centroid from the current-voltage characteristic shifts in a mos structure after uniform gate stress"*, Proc. IEEE 1997 Int. Conference on Microelectronic Test Structures, vol. 10, March 1997, pp. 111-115

[43] R.W. Herfst, P.G. Steeneken, and J. Schmitz, *"Time and voltage dependence of dielectric charging in RF MEMS capacitive switches"*, 45th Annual International Reliability Physics Symposium, Phoenix, AZ, 2007

[44] A. R. Knudsen et al., *"The effects of radiation on MEMS accelerometers"*, IEEE Transaction on Nuclear Science, 1996, vol.43, pp.3122

[45] M. Exarchos et al., *"Charging of Radiation Induced Defects in RF MEMS Dielectric Films"*, doi:10.1016/j.microrel.2006.07.045

[46] S. S. McClure, et al., *"Radiation Effects in Micro-Electro-Mechanical Systems (MEMS): RF Relays"*,IEEE Transaction on Nuclear Science 2002, vol. 49, pp. 3197.

[47] J.Ruan, et al., *"Alpha particle radiation effects in RF-MEMS capacitive switches"*, Microelectronic Relyability 48(2008), pp. 1241-1244.

[48] E. Stassinopoulos, et al., *"The space radiation environment for electronics"*, Proceedings of the IEEE, 76 (11), Nov. 1988, pp. 1423-1442

[49] J.Schwank, *"Total dose effects in MOS devices"*, in IEEE NSREC ShortCourse, 2002

[50] D. Ball, R. Schrimpf, H. Bamaby, *"Separation of ionization and displacement damage using gate-controlled lateral PNP bipolar transistors"*, IEEE Transaction on Nuclear Science, 49(6), 2002, pp. 3185-3190

[51] T. P. Ma, et al., *"Ionizing radiation effects in MOS devices and circuits"*, Wiley, New York, 1989

[52] J.Ziegler, SRIM/TRIM computer code, available on line at www.srim.org

[53] S. Messenger, et al., *"Non-ionizing energy loss (NIEL) for heavy ions"*, IEEE Transaction on Nuclear Science, 1999, pp. 1595-1602